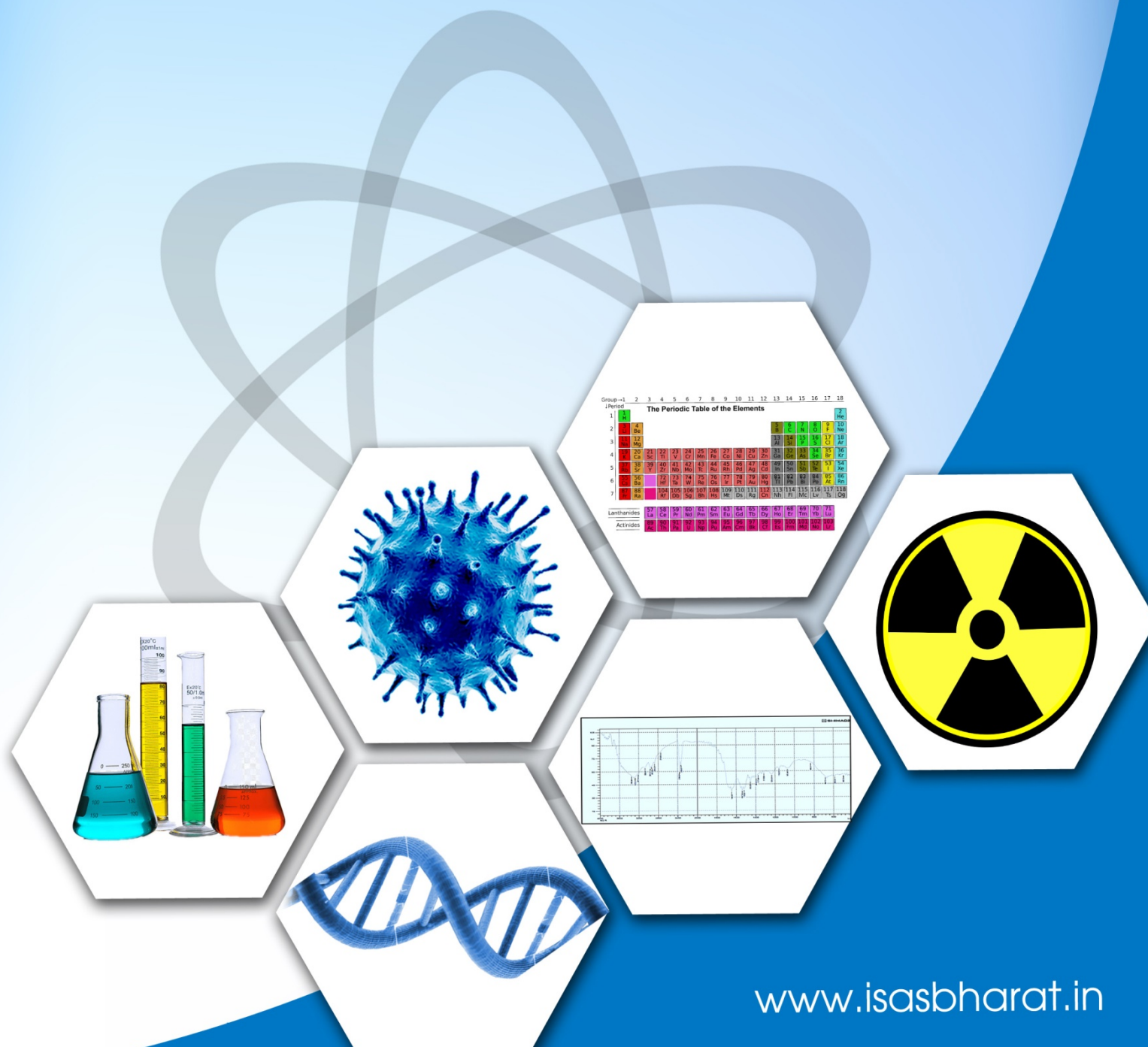




ISSN: 2583-5459
Volume 2 Issue 3
January, 2024

Journal of ISAS

An open access peer reviewed quarterly e-journal by
Indian Society of Analytical Scientists





Journal of ISAS

An open access peer reviewed quarterly e-journal published by Indian Society of Analytical Scientists

Published by: Indian Society of Analytical Scientists (ISAS)

Address: C/o REDS, BARC, Mumbai 400085

Email: isasjournal@isasbharat.in

President ISAS: Dr. Raghaw Saran

J. ISAS

Editorial Board

Editor in Chief

Dr. Nilima Rajurkar, Pune

Members

Dr. Vijayalaxmi C. Adya, Mumbai

Dr. A. K. Basu, Pune

Dr. Vinay Bhandari, Pune

Dr. Avinash Bharati, Nagpur

Dr. Anu Gopinath, Kochi

Dr. Ravin Jugade, Nagpur

Dr. Padmaja S. Vadodara

Dr. Pradeep Kumar, Mumbai

Dr. Prakash Samnani, Vadodara

Dr. Sridhar T. M , Chennai

Dr. S. K. Yadav, Vadodara

Dr. A. N. Garg, New Delhi

Advisory Board

Chairman

Dr. Raghaw Saran, Nagpur

Members

Dr. V. Sivanandan Achari, Kochi

Dr. V. Balaram, Hyderabad

Dr. J. Manjanna, Belgavi

Dr. V. R.Nair, Kollam

Dr. Amrit Prakash, Mumbai

Dr. S. Sriman Narayanan, Vellur

Dr. Shivaramu Prasanna, Bengaluru

Dr. K.P. Vijayalakshmi, Trivandrum

Dr. Mohammed Yusuff K.K., Kochi

Dr. Rajeev Raghavan, Trivandrum

Cover page images- curtsey Pixabay.com

Instruction to Authors

- The Manuscript should be typed in **MS word** (times new roman) with **1.5 spacings** and **font size 12**
- The **title** of the paper should be clear and concise(**font size 14 and bold**), the first letter of each noun and adjective in the title must be in capital letter. It will be followed by names of authors(initials followed by surname) with their affiliation (**font size 12**)
- Corresponding author should be indicated by * with email ID
- The text should be divided into following sections:
 - **Abstract : up to 300 words**
 - **Key words: 5-6**
 - **Introduction**
 - **Experimental**
 - **Results and Discussion**
 - **Conclusions**
 - **Acknowledgement**
- Figures and Tables should be before references with a caption **Figures:** Followed by **Tables:**
- **References**
 - Divisions within the section should be indicated as subheadings
 - The figures and tables should be numbered with Roman numerals and must be mentioned in the text at appropriate places
 - Standard abbreviations for technical terms and journals should be used
 - All constants should be expressed in **SI units**
 - References should be numbered consecutively and should appear in the text as superscript at appropriate places.
 - References should be in following pattern
 - For research paper:**
Authors' initials and surname, Journal abbreviation, Volume, Page, Year.
 - For book:**
Authors' initials and surname, Book name, Publisher, Place, Year.
 - For proceedings:**
Authors' initials and surname Proceedings' of the conference name, place, Page, Month and Year.
- The paper is to be submitted in word file and PDF file to isasjournal@isasbharat.in
- After getting the acceptance of the paper, authors have to submit **signed copyright form and undertaking** before publishing the article



Indian Society of Analytical Scientists.



Editorial

Welcome to the seventh issue of the Journal of Indian Society of Analytical Scientists [J.ISAS,2(3)] which is quarterly open access e-journal with ISSN and Doi number. In this edition, we are pleased to present a diverse array of articles that delve into cutting-edge research and advancements in the field of analytical science. Our aim with this issue is to foster a deeper understanding of analytical methodologies and their applications across various domains.

Nanoparticles play a crucial role in targeted drug delivery, improving treatment efficacy while minimizing adverse effects. They drive advancements in materials science, electronics, and environmental remediation, shaping various fields with their distinctive attributes. The research papers featured in this edition delve into photocatalytic nanoparticle studies, fundamental material transformation under controlled conditions, providing insights into transition metal dichalcogenides' synthesis and structural properties, and a comprehensive review of biogenic nanoparticles. Molecular docking aids in understanding crucial molecular interactions for drug design and development. One of the articles in this issue evaluates the effectiveness of essential oil components against water-borne multi-virulent bacteria and viruses. Through computational modelling, researchers shed light on essential oil constituents' potential antimicrobial properties. Erbium, a rare earth element, finds application in diverse high-tech industries, with its extraction from mineral sources involving intricate processes. The researchers introduce a novel synergistic extraction process for Erbium(III) in their article in this issue. Additionally, a review of a recently published book on aquatic pollution provides further insights into the subject. The articles featured in this issue underscore the dynamic nature of analytical science and its pivotal role in addressing

contemporary challenges across various disciplines. We hope that this issue serves as a catalyst for further exploration and innovation in the field of analytical science.

I extend my heartfelt appreciation to the authors, reviewers, and the editorial team for their dedication and hard work in bringing this issue to fruition. I am sincerely grateful to ISAS president and J.ISAS Advisor, Dr. Raghav Saran, as well as the committed individuals on the editorial board, Dr. Vijayalaxmi Adya, Dr. Vinay Bhandari, and Dr. Sridhar T.M., for their ongoing cooperation. Technical support from Shivani Katak and Vaibhav Parse is highly appreciated.



Dr. Nilima Rajurkar
Editor in Chief
Journal of ISAS

Journal of ISAS

ISSN: 2583-5459 2(3), Pages 1 to 122, (2024)

(An open access Peer reviewed quarterly e- journal by Indian Society of Analytical Scientists)

Contents

S.No.	Title and Authors	Page no.
1	Research Paper: Synergistic Extraction of Erbium(III) by n-Octyl Phenyl Phosphinic Acid (OPPA) with Oxine and 2-Methyl Oxine in Different Diluents Sutanuka Roy, M. Anitha *, Rajak Syed, Sukalyan Basuand D. K. Singh Email*: manitha@barc.gov.in DOI: 10.59143/isas.jisas.2.3.UOOR3254	1-17
2	Research Paper: Molecular Docking Analysis for Evaluating the Efficacy of Active Components of Essential Oils against Water-Borne Multi-Virulent Bacteria and Virus Kshama Balapure *, Vinay M. Bhandari Email*: kshama.balapure@gmail.com DOI: 10.59143/isas.jisas.2.3.BSVG2322	18-40
3	Research Paper: Photocatalytic Studies on Zinc Oxide Nanoparticles Doped with Selenium and Silicon Dioxides for Photodegradation of Lasix Drug L.Ramapriya* and J.Santhanalakshmi Email*: toramapriya@gmail.com DOI: 10.59143/isas.jisas.2.3.YHOJ2087	41-55
4	Review: Chitosan-based Biogenic Nanoparticles for Wastewater Remediation: Synthesis, Characterization, and Applications - A Review Usman Lawal Usman*, S. Ellumalai Anandh, S and Venkatesan Madha Suresh Email*: usman.usman@umyu.edu.ng DOI: 10.59143/isas.jisas.2.3.MUDX2303	56-95
5	Research paper: Temperature Assisted Ligand Conversion from 3R-MoS ₂ to α -MoO ₃ by Preserving Layered Nature Manuja M*, Tintu Thomas and Gijo Jose Email*: manuja.jayan85@gmail.com DOI: 10.59143/isas.jisas.2.3.VRAS7769	96-108
6	Research Paper: Modelling of CO ₂ Sequestration in Deep Saline Aquifer Reservoir using Surface Evolver Software Pradeep Kumar Email*: pradeepk@barc.gov.in DOI: 10.59143/isas.jisas.2.3.LAOI5364	109-121
7	Book Review: Aquatic Pollution – Concerns and Abatement by Imtiyaz Qayoom, Adnan Abubakr, Anu Gopinath, Shabir.A. Dar , & Keezia Khurshid Anoop Krishnan Email*: sree.anoop@ncess.gov.in DOI: 10.59143/isas.jisas.2.3.KRGM6017	122

Synergistic Extraction of Erbium (III) by n-Octyl Phenyl Phosphinic Acid (OPPA) with Oxine and 2-Methyl Oxine in Different Diluents

Sutanuka Roy¹, M. Anitha^{2*}, Rajak Syed², Sukalyan Basu¹ and D. K. Singh²

¹Department of Chemistry, The University of Burdwan, Burdwan- 713104, India;

²Hydrometallurgy & Rare Earths Development Section,

Materials Processing & Corrosion Engineering Division, Bhabha Atomic Research Centre,
Mumbai- 400085, India

*Email: manitha@barc.gov.in

Received: 17.10.2023, Revised: 10.11.2023, Accepted: 18.11.23

Abstract

The synergistic extraction of erbium (III) was investigated using n-octyl phenyl phosphinic acid (OPPA) in combination with oxine and 2-methyl oxine in different diluents. The extraction efficiencies of these synergistic extractants for erbium were measured as a function of extractant concentration, pH, temperature and diluents. The composition of extracted species determined by slope analysis method indicates the formation of $[\text{Er}(\text{HA}_2)_3(\text{HOX})]_{\text{org}}$ complex and was also confirmed by Infrared spectroscopy. Based on the experimental data, the values of the equilibrium constants as well as synergistic coefficients have been calculated. Both the donors (oxine/2-methyl oxines) exhibited almost similar synergistic effect with OPPA. The extraction of erbium with these solvents was exothermic in nature. Diluent dependency on synergism for OPPA-oxine/2-methyl oxine system was explained in terms of regular solution theory of Hildebrand. Experimentally determined solubility parameter of ternary adduct was correlated with theoretically obtained values.

Key words: OPPA, oxine, 8-hydroxyquinoline, erbium, synergistic extraction

Introduction:

The rare earth elements (REE) or lanthanides, scandium as well as yttrium, are a group of elements that have become increasingly important in number of high-tech applications including hybrid cars, wind turbines, magnets, phosphors, lasers, optical fibers etc. Erbium is one of the promising REE and used extensively for up-conversion materials, displays, corrosion resistant coatings, as a tritium permeation barrier for nuclear reactors, solar films, antireflection coating material, bio imaging etc.^{1,2}. The high value of REE depends on its effective individual

separation, which is very challenging to accomplish owing to low separation factors between the adjacent REE because of their similar chemical properties. Among the techniques used, solvent extraction is extensively used in the commercial processing of rare-earth compounds. Several extractants have been used in the past to separate REE from various aqueous streams.

Lanthanides (III) because of their typical hard Lewis acid character, were extracted in early stages by organophosphorus ligands, which act as hard Lewis bases and thereby impose high extraction power for the REE having high coordination number³. Similarly, 8-hydroxyquinoline (HOX) and its derivatives also achieve a high degree of extraction under favorable condition. The extraction efficiencies of these compounds have been extensively investigated on the extraction of REE⁴. Alternatively, synergistic extraction systems have been applied to rare earths, where a significant increase in the extraction efficiency of REE was observed in combination of two extractants. The extractant having higher distribution ratio with the metal ion of interest is considered as the main extractant while the other is referred as donor.

The systematic synergistic solvent extraction of erbium has been carried out with neutral type of extractants⁵⁻⁶. The synergistic effect in the extraction of gadolinium, dysprosium and erbium with a ternary system consisting of tri-n-butyl phosphate (TBP) and tricaprylmethyl ammonium chloride (Aliquat336) in xylene from thiocyanate solution was described along with the composition of extracted species⁷. The effect of various process parameters like pH, concentration of NH₄SCN, Aliquat336 and TBP on distribution ratios have been described. Neutral organophosphorus compounds with a phosphoryl complexing center were found to cause synergistic shifts in the extraction of Nd(III) and Er(III) from chloride based solutions by acidic extractant 3,5-diisopropylsalicylic acid. The extracted neodymium and erbium complexes had the composition NdA₃L₂ and ErA₃L₂, where HA=3,5-diisopropylsalicylic acid and L is a neutral organophosphorus compound⁸.

Though synergistic extraction of Er has been reported, investigations with acidic extractant namely, n-octyl(phenyl)phosphinic acid (OPPA) has not been reported so far, particularly in combination with 8-hydroxyquinoline (HOX), commonly known as oxine. Solvent extraction of cobalt and nickel from aqueous sulphate medium was explored using OPPA in n-dodecane⁹. Extraction behavior of Y(III) from hydrochloric acid medium by OPPA in different diluents was investigated in detail and higher extraction was observed with low dielectric constant diluents. Extraction behavior of lanthanides with OPPA was investigated in detail where OPPA was found to be promising extractant for separation of heavier rare earths from the lighter rare earths¹⁰. The degree of synergism is correlated to stability of the adduct formed, which in turn depends on the nature of extractants as well as on the type of organic diluent used. Thus, the proper choice of

diluent is very important for synergistic enhancement. The dielectric constants of solvents alone cannot explain such type of variation of synergistic effect. Akiba et. al.¹¹ had shown the effect of diluent on synergic extraction of europium by the mixture of thenoyltrifluoroacetone and tri-*n*-octyl phosphine oxide by evaluating adduct formation constants. They found the adduct formation constant is correlated with one of the physical properties of the diluent, solubility parameter (δ_{org}) for the overall reaction, which is useful in selection of diluents in solvent extraction. The formation constants of the tributyl phosphate (TBP) adduct with the tris-thenoyltrifluoroacetone (TTA) chelate in several diluents was evaluated for scandium extraction and was described in the light of solubility parameter concept¹². The activity coefficients of the chemical species vary with the medium, the correlation between the formation constant and the nature of diluent becomes necessary as per Hildebrand regular solution theory¹³.

In the present work, the extraction of erbium with *n*-octyl(phenyl)phosphinic acid (OPPA) in combination with oxine or 2-methyl oxine from chloride solution was explored. This new synergistic extraction system has not been reported so far for erbium and is being reported for the first time. The main objective is to study the extraction behavior of Er(III) from chloride medium by the synergistic extractant(OPPA-HOX) in different diluents under various extraction process parameters like pH, extractant and donor concentration, temperature etc. The solubility of different diluents under the study in OPPA-HOX-Er has been evaluated to understand the effect of the diluents on the extent of synergism.

Experimental:

Materials and Methods

Erbium (III) chloride stock solution of known concentration was prepared by dissolving vacuum dried Er₂O₃ in Conc. HCl followed by evaporating excess HCl. The solution is made up to known volume and pH was adjusted to ~2 with HCl. The stock solution was diluted to the desired concentrations whenever necessary. The extractant OPPA was synthesized as described elsewhere [14]. The Synthesized OPPA extractant was estimated using potentiometry in 75% ethanol and was found to be 99% pure with dibasic acid content below detection limits. Elemental analysis of OPPA was performed on a Thermofinnigan Flash EA TM 1112 elemental analyser. The results were as follows: C-66.67% (theoretical 66.12%), H-9.50% (9.12%) and P-11.58% (12.18%). Oxine and 2-methyl-oxine were purchased from M/s Sigma Aldrich, USA and were used without any purification, pH measurements were carried out using a digital pH-meter, Systronics model 335 and concentration of erbium in aqueous solutions were determined by ICP-OES (JY Ultima 2). IR measurements were carried out using A Bruker Alpha Platinum-ATR.

Procedure

Organic phase was prepared by dissolving appropriate amount of OPPA extractant in desired diluent. The initial pH of the feed (aqueous) solution was adjusted to 2 before the equilibration experiment was carried out. Aqueous solutions (10 ml) containing 0.01 M Er(III) ions was contacted with 0.1 M OPPA (10ml) in n-dodecane for 30 minutes in a mechanical shaker at a certain temperature. After phase separation of organic and aqueous phases, equilibrium pH of the raffinate solutions was measured. The solutions were diluted as required with electronic grade dilute HNO₃ and analysis of erbium was carried out with ICP-OES make Jobin Yvon inductively coupled plasma-atomic emission spectrometer. The erbium concentration in the organic solutions were calculated by material balance. The error in the analysis was within ±1.0%. All experiments were performed in triplicate and average data is reported. The stripping studies were carried out with 3.5 M HCl. To determine the effect of temperature on distribution ratio, experiments were performed in a thermostat (±0.5 °C) with mechanical shaking for 30 min. Temperature was varied in the range of 300 to 333 K. The aqueous phases were separated and analyzed for metal ions. The distribution ratio (*D*) was calculated as follows,

$$D = \frac{Er(III)_{org}}{Er(III)_{aq}} \quad (1)$$

where ‘org’ and ‘aq’ represent organic and aqueous phases respectively. The synergistic coefficient (*S.C*) of adduct, which governs the synergistic effect is evaluated by using the following equation [15].

$$S.C = \log \frac{D_{mix}}{D_0 + D_1} \quad (2)$$

where *D_{mix}*, *D₀* and *D₁* represent the distribution ratio for ternary system, with individual ligand (OPPA) and with individual donor (oxine or 2-methyl oxine) respectively.

Results and Discussion:

Influence of pH

Preliminary experiments were performed to monitor the effect of equilibrium pH on the extraction of Er(III) with OPPA and its mixture with oxine/2-methyl oxine. It was observed that the extraction of Er(III) increased in agreement with equation (5) with increase in pH. However at pH beyond 3, precipitation was observed. Hence all experiments were performed at feed pH 2 for feed solution.

Extraction of Er(III) using OPPA

OPPA concentration was varied from 0.01–1.0 M in different diluents to understand its effect on extraction behaviour of Er(III). The pH of initial feed solution was kept constant at 2 and the data was generated at O/A ratio of 1. The log *D* vs log [OPPA] plot for Er in different diluents is

shown in Fig. 1. The nature of the extracted species was established by slope analysis technique. The plots were straight lines with slope ~ 3 , no changes in the slopes were observed. This confirms that the stoichiometry of Er(III)–OPPA complexes does not change with the diluent. The extraction of Er(III) was found to increase with increase in OPPA concentration irrespective of diluent. This is obviously due to making metal ion sphere more lipophilic by the ligand OPPA. Under the present experimental condition, oxine or 2-oxine show only a poor extraction trend towards Er(III).

Extraction of Er(III) with OPPA in presence of fixed concentration of oxine or 2-methyl oxine

In the case of ternary extraction (OPPA+oxine), the effect of OPPA on the extraction of Er(III) was studied keeping the oxine concentration constant (0.08 M) at O/A=1. The extraction of Er(III) increased with OPPA concentration irrespective of diluents. Fig. 2 shows the extraction of Er(III) using OPPA and oxine using several diluents. The $\log (D_{mix}-D_0)$ against $\log [OPPA]$ plot show straight lines for all diluents with slopes corresponding to ~ 3 . This clearly indicates the presence of three bidentate chelating groups of OPPA, (H_2A_2), denoted as dimer of OPPA in non-polar diluent, surrounding the Er(III) cation in the ternary extraction system. Similar results were obtained for Er(III) extraction with OPPA+2-methyl oxine system, with fixed concentration of 2-methyl oxine (0.08 M) and variation in OPPA concentration as shown in Fig. 3. The synergistic co-efficient (*S.C*) of adduct formed by Er(III) with OPPA and donor are evaluated and tabulated in Table 1. In all the diluents studied synergistic coefficient values increased with increase in concentration of diluents up to 0.08 M and for a given concentration the synergism followed the order: toluene > methyl isobutyl ketone > nitrobenzene > dichloromethane > petrofin.

Extraction of Er(III) with oxine/2-methyl oxine OPPA in presence of fixed concentration of OPPA

The effect of donor concentration (oxine or 2-methyl oxine) at fixed concentration of OPPA concentration (0.02 mol/L) in the organic phase in various diluents on extraction of Er(III) at O/A=1 were investigated to evaluate the stoichiometry of donor molecules (HOX) in Er-OPPA-HoX complex. The results are illustrated in Fig. 4 and Fig. 5. The slope of straight lines of the plot of $\log (D_{mix}-D_0)$ vs. $\log (\text{oxine or 2-methyl oxine})$ correspond to ~ 1 , indicating that one mole of oxine or 2-methyl oxine is present in the extracted moiety in the organic phase. Based on these observations of slope analysis technique, it is evident that the nature of the extracted species in

the organic phase is found to be $[\text{Er}(\text{HA}_2)_3(\text{HOX})]$. Thus, the probable synergistic extraction of Er(III) may be described by the following equations:



The extraction equilibrium constant for the binary system K is related to distribution coefficient D_0 is expressed by the following equation:

$$\log K = \log D_0 - 3 \log [\text{H}_2\text{A}_2] - 3 \text{pH} \quad (5)$$

The ternary extraction constant K' associated with distribution ratio of ternary adduct (D_{mix}) by the following equation:

$$\log K' = \log (D_{\text{mix}} \cdot D_0) - 3 \log [\text{H}_2\text{A}_2] - \log [\text{HOX}] - 3 \text{pH} \quad (6)$$

and hence,

$$\log K_s = \log K' - \log K \quad (7)$$

where K_s is the overall formation constant of ternary adduct. The equilibrium constant, ternary extraction constant and overall formation constants were evaluated for both Er-OPPA-oxine and Er-OPPA-2-methyl oxine systems and are illustrated in the Table 2. This clearly indicates formation of strong ternary adduct for both oxine and 2-methyl oxine complex in toluene media.

IR spectrum of Erbium complex with oxine

Infrared spectra of OPPA and its extraction with erbium(III), the ternary extracted species is shown in Fig. 6. The characteristic absorption of OPPA is 1215 cm^{-1} designated to P=O vibrations, which shifted to 1170 cm^{-1} in the Er(III)-OPPA complex.

Thermodynamic parameters of erbium extraction with OPPA-oxine and OPPA-2-methyl oxine

The effect of temperature is one of the factors affecting the synergistic extraction process. The thermodynamic parameters were deduced for Er(III) extraction by OPPA + Oxine/2-methyl oxine in different diluents by performing experiments at different temperature with fixed feed and extractant concentrations. The change in enthalpy (ΔH_f^0), entropy (ΔS_f^0) and free energy (ΔG_f^0) of each of the extraction system were evaluated using following equation

$$\log K' = \frac{-\Delta H_f^0}{2.303 RT} + \frac{\Delta S_f^0}{2.303 R} \quad (8)$$

The linear variation of $\log K'$ against $1/T$ in different diluents are shown in Figs. 7 and 8, and determined values of ΔH_f^0 and ΔS_f^0 are tabulated in Table 3.

The interaction between hard acid (Er(III)) with hard donor center (O) results in hard-hard interaction as per Pearson's HSAB principle, and this interaction between the cation and the ligands provides a negative enthalpy contribution ($\Delta H_f^0 < 0$). The decrease in the randomness of the system, resulting due to formation of the cation-anion bonds, contributed negatively to the entropy component. ($\Delta S_f^0 < 0$) [16]. Overall ternary complex formation therefore proceeds via outer sphere mechanism as the expansion of co-ordination shell of f-block metal is permitted. Such a mechanism is favored by enthalpy change as there is no breakage in M-H₂O bond.

Diluents dependency

The synergistic effect is known to be strongly diluent dependent [17] as is confirmed by the data presented in Table 1. Such change in distribution ratios could not be explained by dielectric constants of solvents [18]. Arichi¹⁹ reported that only ligands containing a polar group or atom yield high distribution ratios. Also the aromatic compounds are more efficient than corresponding aliphatic compounds. In the present case, the nature of the solvents deciding the extent of synergism can be explained based on the Hildebrand's regular solution theory [13]. The activity and activity coefficient of interacting species can be calculated based on the regular solution theory, using solubility parameters and molar volumes data. Accordingly adduct formation constant K_s is related to the solubility parameter of diluent by the following equation [11].

$$\log K_s = 2B \delta_{org} + \text{constant} \quad (9)$$

$$\text{where, } B = 1/ 2.303 RT [V_{adduct} \cdot \delta_{adduct} - V_{chelate} \cdot \delta_{chelate} - V_{donor} \cdot \delta_{donor}] \quad (10)$$

and, V = molar volumes of adduct, OPPA(chelating agent) and HOX(donor)

δ = adduct solubility parameter, OPPA(chelating agent) and HOX(donor)

Both V and δ depend on nature of diluent used in extraction and constant term in equation (9) is independent of diluent.

A slope of '2B' was observed for both the adducts formed by OPPA-Oxine/2-methyl oxine systems. In Fig. 9, the slope obtained from the plot of adduct formation constant for Er(III) with OPPA-oxine/2-methyl oxine in different diluents vs solubility parameters (δ_{org}) is used in estimating the δ_{adduct} . A comparison of δ_{adduct} values (Table 4) obtained both theoretically and experimentally for two types of ternary complexes involving oxine and 2-methyl oxine establishes the validity of the regular solution theory in these systems.

Conclusions:

The effect of diluents in extraction behaviour of Er from nitric acid medium by synergistic solvent mixture of OPPA as ligand and oxine/2-methyl oxine as donor was investigated in detail. Both the donors (oxine/2-methyl oxines) exerted almost similar synergistic effect with OPPA.

Among the diluents studied, toluene gave a better synergism in comparison to other diluents. The extraction of erbium with these solvents was exothermic in nature. The composition of extracted species determined by slope analysis method indicated the formation of $[\text{Er}(\text{HA}_2)_3(\text{HOX})]_{\text{org}}$ complex and was also confirmed by Infrared spectroscopy. Solubility parameter for the ternary adducts formed in Er-OPPA-Oxine/2-methy oxine system in different diluents were experimentally determined and were compared well with the theoretical calculated values establishing the validity of the solution theory of Hildebrand.

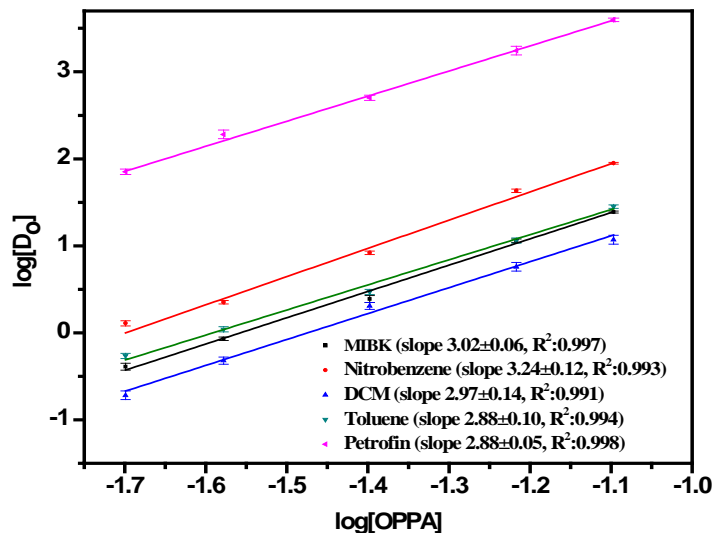


Fig. 1 Variation of distribution ratio of Er(III) in different diluents with concentration of OPPA (Concentration of Er(III) in the feed: 0.01M, O/A:1, Temperature:27°C)

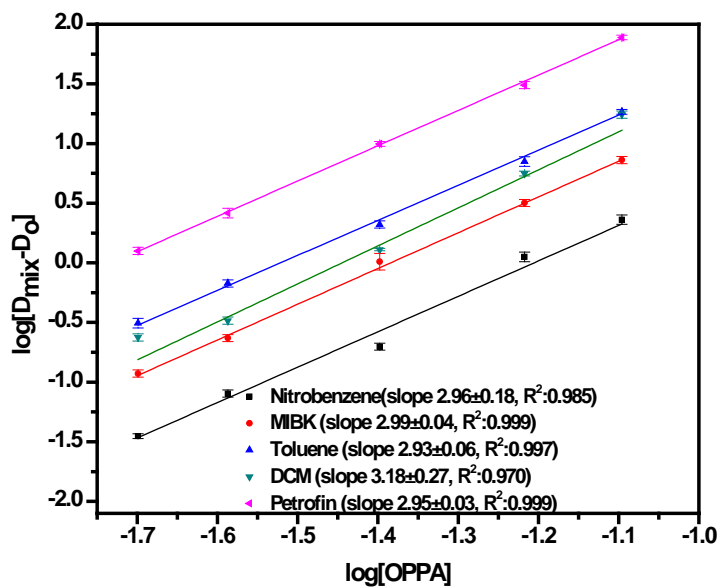


Fig. 2. Effect of OPPA concentration on extraction of Er(III) in constant concentration of oxine.

(Er(III) in the feed: 0.01M, oxine :0.08 M, O/A:1, Temperature:27°C)

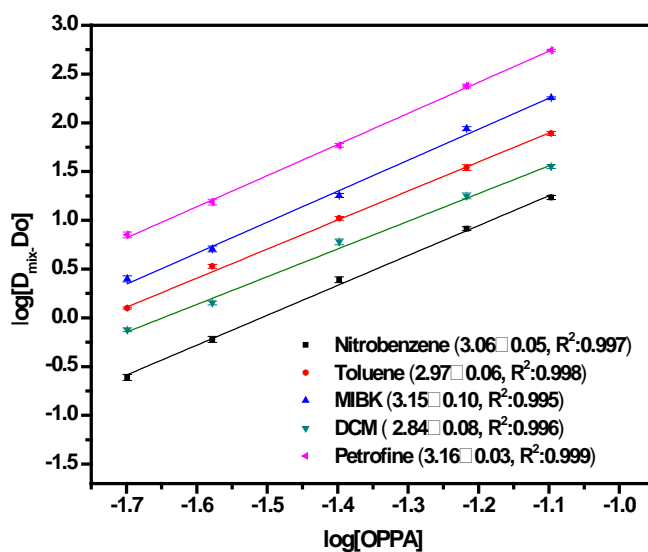


Fig. 3 Effect of concentration of OPPA on Er(III) extraction in presence of fixed concentration of 2-methyl oxine

(Concentration of Er(III) in the feed: 0.01M, 2-methyl oxine :0.08 M, Temperature:27°C)

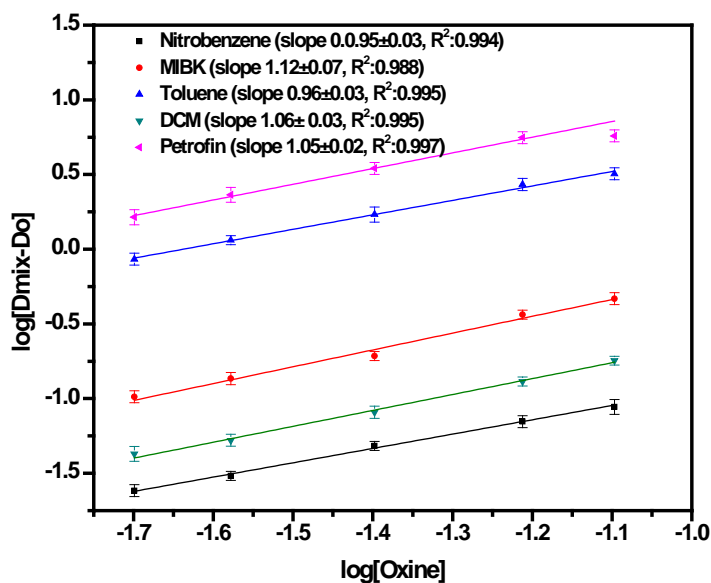


Fig. 4 Effect of concentration of oxine on Er(III) extraction in presence of fixed concentration of OPPA

(Er(III) in the feed: 0.01M, OPPA :0.02 M, O/A:1, Temperature:27°C)

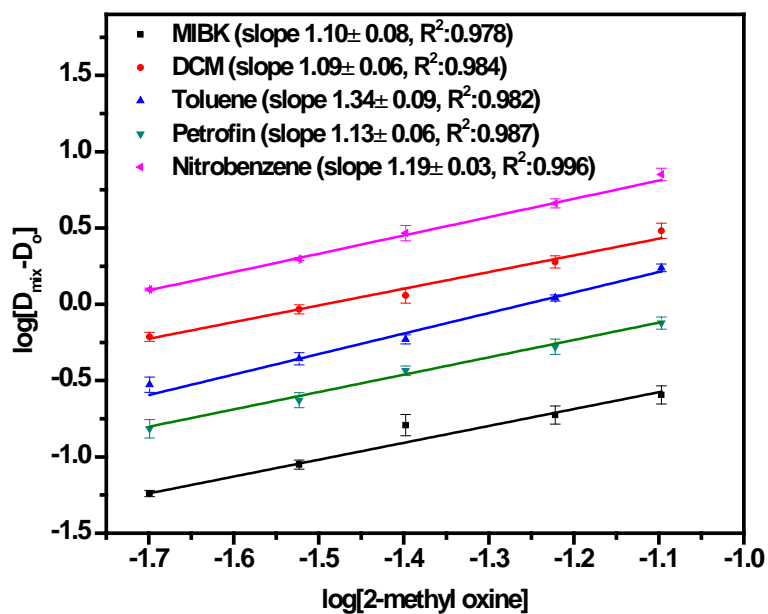


Fig. 5 Effect of concentration of 2-methyl oxine on Er extraction in Er-OPPA-2-methyl oxine system

(Er(III) in the feed: 0.01M, OPPA :0.02 M, O/A:1, Temperature:27°C)

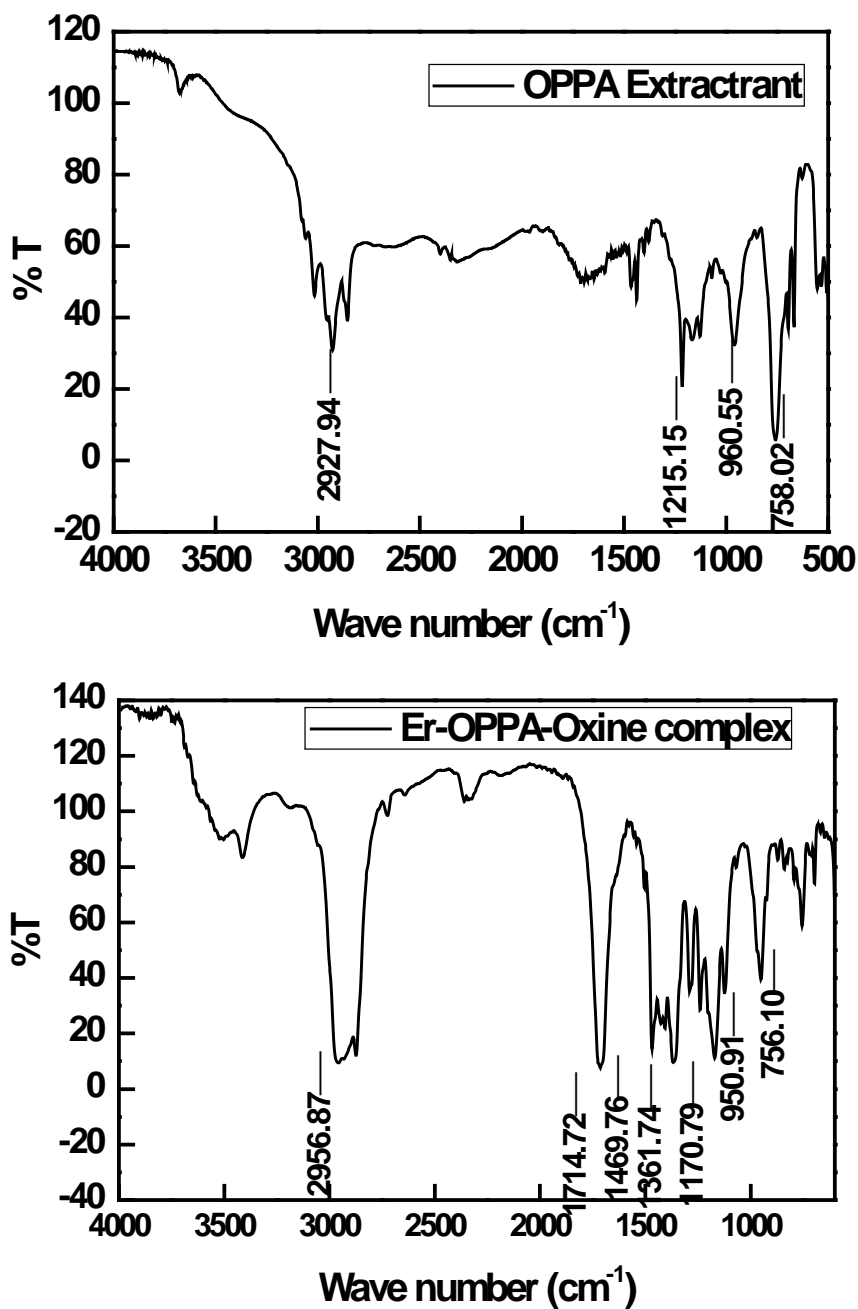


Fig. 6 IR Spectra of extractant OPPA and Er³⁺-OPPA-oxine complex

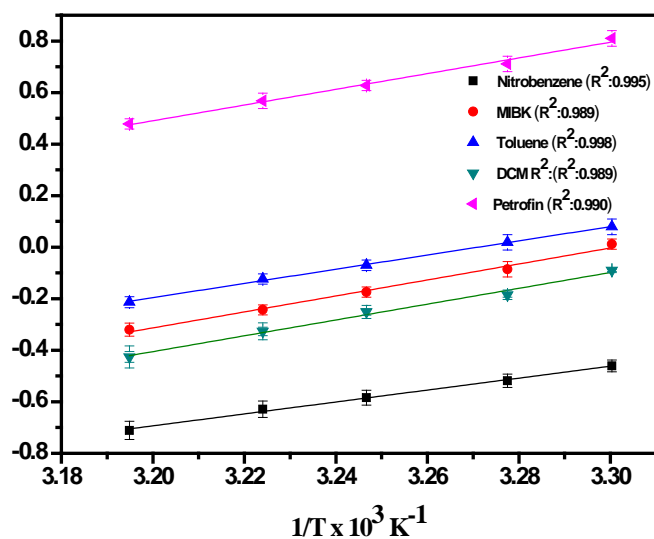


Fig. 7 Variation of equilibrium constant of Er(III) – OPPA – Oxine complex with temperature.

(Er(III) in the feed: 0.01M, OPPA :0.02 M, Oxine: 0.08M, O/A:1)

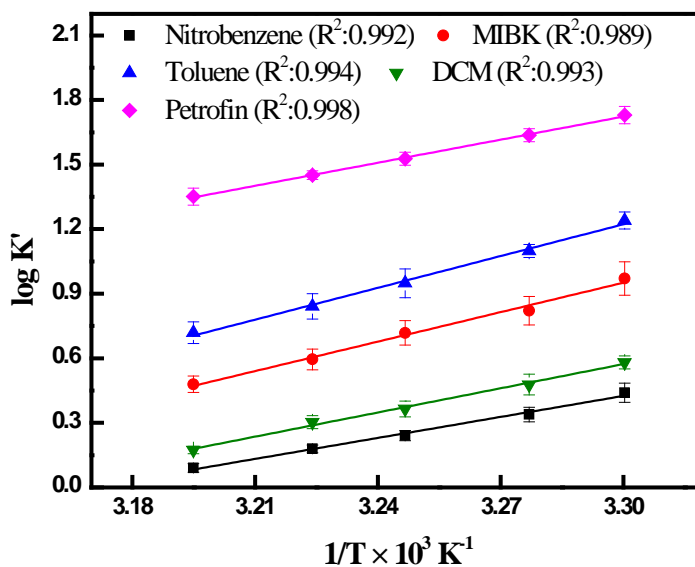


Fig. 8 Effect of temperature on equilibrium constant of Er(III) – OPPA – 2-methyl oxine complex

(Er(III) in the feed: 0.01M, OPPA :0.02 M, Oxine: 0.08M, O/A:1)

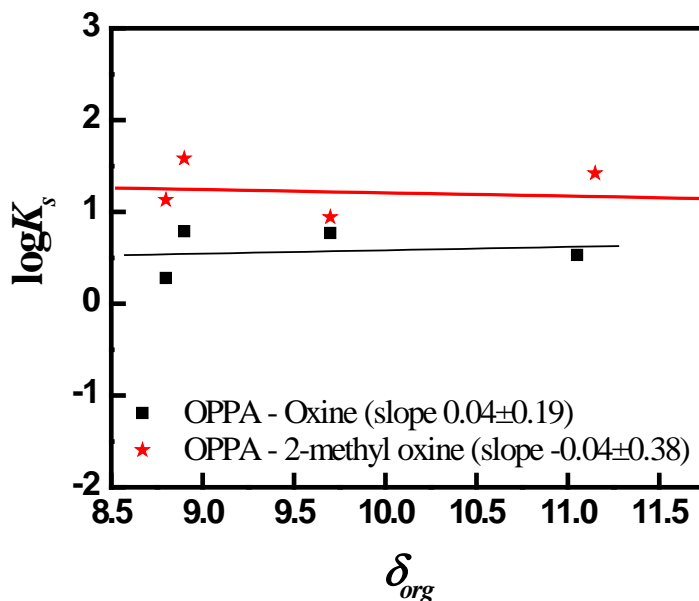


Fig. 9 The variation of $\log K_s$ vs δ_{org} in synergistic extraction of Er^{3+} in different diluents

TABLE 1: Synergistic extraction of Er(III) at fixed concentration of OPPA (0.02 M) with varying concentration of donor

Diluents	Concentration of oxine or 2-methyl oxine[M]	S.C (oxine system)	S.C (2-methyl oxine system)
Nitrobenzene	0.02	0.02 ± 0.001	0.22 ± 0.013
	0.04	0.03 ± 0.001	0.35 ± 0.017
	0.08	0.10 ± 0.003	0.49 ± 0.046
Methyl isobutyl ketone	0.02	0.03 ± 0.002	0.27 ± 0.013
	0.04	0.07 ± 0.002	0.36 ± 0.008
	0.08	0.17 ± 0.003	0.72 ± 0.049
Toluene	0.02	0.74 ± 0.045	0.41 ± 0.010
	0.04	0.99 ± 0.050	0.99 ± 0.04
	0.08	1.25 ± 0.065	1.00 ± 0.05
Dichloromethane	0.02	0.03 ± 0.001	0.11 ± 0.012
	0.04	0.06 ± 0.002	0.22 ± 0.014
	0.08	0.15 ± 0.004	0.38 ± 0.007
Petrofin	0.02	0.01 ± 0.001	0.01 ± 0.001
	0.04	0.02 ± 0.001	0.01 ± 0.001
	0.08	0.03 ± 0.002	0.04 ± 0.002

TABLE 2: Equilibrium constants for binary and ternary systems

Diluents	Er(III) –OPPA system	Er(III) –OPPA – Oxine system		Er(III) –OPPA – 2-methyl oxine system	
	$\log K$	$\log K'$	$\log K_s$	$\log K'$	$\log K_s$
Nitrobenzene	-0.98± 0.026	-0.45 ± 0.015	0.53 ± 0.0	0.44± 0.03	1.42± 0.060
Methyl isobutyl ketone	-0.16± 0.003	0.02± 0.001	0.18± 0.00	0.97± 0.04	1.13± 0.051
Toluene	-0.74± 0.041	0.05± 0.006	0.79± 0.0	1.24± 0.02	1.98± 0.070
Dichloromethane	-0.86± 0.035	-0.09± 0.006	0.77± 0.0	0.54± 0.02	1.40± 0.060
Petrofin	1.39± 0.035	0.81± 0.006	-0.57± 0.0	1.73± 0.02	0.34± 0.056

TABLE 3: Results of Thermodynamic parameters

Ternary System	Diluents	ΔH (k J mol ⁻¹)	ΔS (JK ⁻¹ mol ⁻¹)	ΔG (k J mol ⁻¹)
Er(III) – OPPA – Oxine	Nitrobenzene	-38.40±1.55	-135.52±3.12	-1.24±0.03
	Methyl isobutyl ketone	-56.38±2.71	-185.92±4.25	-0.32±0.01
	Toluene	-47.81±0.29	-156.84±0.95	-0.29±0.02
	Dichloromethane	-53.76±2.27	-179.24±4.42	-1.61±0.02
	Petrofin	-60.25±1.36	-183.24±7.91	-4.73±0.03
Er(III) – OPPA – 2-methyl oxine	Nitrobenzene	-62.19±2.31	-197.22±5.13	-2.44±0.02
	Methyl isobutyl ketone	-87.26±2.66	-269.90±5.12	-5.49±0.03
	Toluene	-94.08±2.67	-287.09±4.05	-7.03±0.04
	Dichloromethane	-71.67±1.78	-225.60±4.98	-3.32±0.02
	Petrofin	-68.32±2.14	-192.66±3.96	-9.95±0.03

TABLE 4: Solubility parameter (δ_{adduct}) of ternary system

Ternary System	δ_{adduct} ($\text{J}^{1/2} \text{cm}^{-3/2}$)	
	Theoretical	Present work
OPPA – Oxine	8.51	8.93
OPPA – 2-methyl oxine	8.58	8.70

References

1. D. Levchuk, S. Levchuk, H. Maier, H. Bolt, A. Suzuki, *J Nucl Mater*, 367, 1033, 2007.
2. S. Saini, K. Chen, X. Duan, J. Michel, L.C. Kimerling, M. Lipson, *J Electron Mater*, 33, 809, 2004.
3. T. Sekine, Y. Hasegawa, *Solvent Extraction Chemistry*; Marcel Dekker: New York, 1978.
4. T. Miaomiao, J. Qiong, L. Wuping, *Journal of Rare Earths*, 31(6), 604, 2013.
5. P.M. Bangroo, H.C. Arora, *Indian Journal of Chemistry Section A*, 30(9), 816, 1991.
6. T. Taketatsu, N. Toriumi, *J. Inorg Nucl Chem*, 31(7), 2235, 1969.
7. A.G. Gaikwad, A.D. Damodaran, *Analytical Sciences*, 6(6), 871, 1990.
8. J.S. Preston, C. Anna du Preez, *Solvent Extraction and Ion Exchange*, 13(1), 27, 1995.
9. S. Mondal, V. Kumar, J.N. Sharma, R.C. Hubli, A.K. Suri, *Separation and Purification Technology*, 89, 66, 2012.
10. M. Anitha, D.K. Singh, R. Ruhela, J.N. Sharma, H. Singh, *Desalination and Water Treatment*, 38(1-3), 65, 2012.
11. K. Akiba, M. Wada, T. Kanno, *J. Inorg Nucl Chem*, 43(5), 1031, 1981.
12. K. Akiba, T. Ishikawa, N. Suzuki, *J. Inorg Nucl Chem*, 33(12), 4161, 1971.
13. J.H. Hildebrand, R.L. Scott, *Solubility of non-electrolytes*. Dover, New York, 1964.
14. G.W. Mason, N.L. Schoffer, *J Inorg Nucl Chem*, 32, 3375, 1970.
15. M. Taube, S. Siekierski, *Nucleonika*, 6, 489, 1961.

16. G.R. Choppin, A. Morgenstern, Solvent Extr Ion Exch, , 18 (6), 1029, 2000.
17. P. Dey, S. Banerjee, S. Basu, Radiochemistry, 54(2), 153, 2012.
18. M. Kyrš, K. Svoboda, P. Lhoták, J. Alexová, J Radioanal Nucl Chem, 254(3), 455, 2002.
19. J. Arichi, G. Goetz-Grandmont, J.P. Brunette, Hydrometallurgy, 82(1-2), 100, 2006.

Molecular Docking Analysis for Evaluating the Efficacy of Active Components of Essential Oils against Water-Borne Multi-Virulent Bacteria and Virus

Kshama Balapure^{*}, Vinay M. Bhandari

Chemical Engineering and Process Development Division

CSIR-National Chemical Laboratory, Pune-411008, India

*Email: kshama.balapure@gmail.com

Received: 13.12.2023, Revised: 25.1.2024, Accepted: 27.1.24

Abstract

Traditional Indian knowledge of Ayurveda mentions a large number of essential oils that contain many active compounds such as thymol, eugenol and cinnamaldehyde etc. which contemplate nontoxic for human being and have been used mostly in the field of medicine. An application of essential oils comprising antimicrobial activities was recently described in the SWASTIIK technology (Safe Water and Sustainable Technology Initiative from Indian Knowledgebase) in conjunction with cavitation/ intense mixing for drinking water treatment. Further, it is intended to demonstrate the efficacy of SWASTIIK technology to combat multi-virulent bacteria and emerging viruses such as *Escherichia coli* and SARS-CoV-2 (Severe Acute Respiratory Syndrome Coronavirus-2) respectively with the help of *in silico* computational tools. Docking study indicated eugenol and thymol were the most effective ligands against the microorganisms, although SARS-CoV-2 performed better with a low binding affinity (-7.2 kcal/mol) than multi-virulent *E. coli* (-4.5 kcal/mol). SWASTIIK technology for eliminating harmful microorganisms is, therefore, expected to be more effective in combating viruses, including SARS-CoV-2. Further, favorable ADMET results suggest suitability of the active components for further clinical trials study or for possible health benefits of water treated using SWASTIIK technology. In view of lack of human studies, to evaluate the effectiveness and safety of essential oils for direct intake, clinical trials with more well-designed protocols are needed.

Key Words: SWASTIIK, Molecular Docking, Water Disinfection, Essential oil, SARS-CoV-2

1. Introduction:

Safe and pure water is important for preventing many waterborne diseases and for saving millions of lives¹. Drinking water contaminated with coliform bacteria, especially *Escherichia coli* (*E. coli*), may cause dysentery, vomiting, abdominal pain, loss of appetite, headaches, fever, and sometimes creates life threatening complications². Waterborne diseases cause millions of deaths worldwide each year because of severe bacterial infections^{3,4}. Nowadays, antimicrobial resistance is also one of the world's biggest concerns, affecting millions of lives. A multidrug-resistant *E. coli* is the one of main culprits in this regard due to its capability to produce a wide variety of virulence factors, especially cell membrane and adhesion proteins⁵. Furthermore, a number of emerging infectious diseases have also been identified in recent years, such as COVID-19, which is caused by Severe Acute Respiratory Syndrome Coronavirus 2 (SARS-CoV-2), declared as a pandemic by the World Health Organization. The spread of it was rapid, infecting 71,351,695 people and causing 1, 612, 372 deaths globally as of 15 December 2020⁶. The traces of the SARS-CoV-2 virus in water samples were also detected⁷. A reliable and sustainable water management is imperative in these types of situations. It is necessary to implement new technologies as possible alternatives to existing chemical methods (e.g. chlorination) which have serious disadvantages, as well as to enhance immunity in the COVID-19 scenario.

Safe Water and Sustainable Technology Initiative from Indian Knowledgebase (SWASTIIK) is recently reported as one of the effective and techno-economically feasible water disinfection technology⁸⁻¹¹. In contrast to most of the physico-chemical methods of treatment, the SWASTIIK technology demonstrated promising application of different essential oils such as ajwain oil, peppermint oil for the disinfection of pathogenic bacteria from water by just simple mixing or in conjunction with hydrodynamic cavitation. The phenomenon of hydrodynamic cavitation involves formation, growth and collapse of cavities in a liquid creating extremely high temperatures (up to 10000 K) and pressures (up to 5000 atm) at the implosion point, consequently producing oxidizing agents and, subsequently creating an environment favorable for disinfection^{12,13}. Hydrodynamic cavitation using essential oils achieves complete disinfection in less than a minute by combining the effects of antimicrobial activity of the essential oils and cavitation. It is cost-effective, sustainable, and offers a greener way to treat water containing variety of disease-causing bacteria. Essential oils can contain large number of chemical compounds such as thymol, carvacrol,

cinnamaldehyde etc. which are considered safe for mankind and have also been accepted by the Food and Drug Administration (FDA)¹⁴. The efficiency of the SWASTIIK technology is already proven at pilot plant scale for disinfecting different harmful microorganisms such as gram-negative (*E. coli*) and gram-positive (*S. aureus*) bacteria, antimicrobial-resistant bacteria (methicillin-resistant *Staphylococcus aureus*) and *Pseudomonas aeruginosa*, within less than 10 min. The basis for the selection of essential oils requires evaluating active components like thymol, menthol, cinnamaldehyde, eugenol, and terpinen-4-ol, which play a significant role in disinfecting water. The SWASTIIK process can give an alternative to the chlorination as well as other water treatment processes such as UV, membrane, ozone etc. However, the technology needs to be evaluated further against multivirulent pathogenic bacteria and viruses in order to determine its broad effectiveness. The requirement of a specialized laboratory for working on multivirulent bacteria and viruses limits the experimentation *in vitro*. Though, hundreds of essential oils are listed having antimicrobial properties, it does not necessarily infer their direct use in water disinfection, and selecting appropriate oils against specific organism is crucial to maximize its usefulness for effective disinfection and for additional health benefits.

Computer- aided drug design (CADD) is a useful tool to check the efficacy of the active ingredients of essential oils against harmful pathogens and for the selection of appropriate oil, to save the time/ laborious experimentations and resources. CADD techniques such as *in silico* molecular docking can virtually analyze binding efficacy of the ligand molecule (active components of essential oil) against target compound (protein compound of an organism^{15,16}. The molecular docking provides insights into the binding conformation of antimicrobial compounds with pathogenic bacteria and viruses, as well as to evaluate the mode of action, protein-ligand interactions. Various essential oils exhibit varied binding activities towards different organisms. It is possible to predict efficacy of essential oils against various organisms by analyzing its binding affinity scores. These predictions will assist in designing and conducting specific experiments for water disinfection under laboratory conditions^{17,18}.

The objectives of this research include evaluation of the efficacy of essential oils used in SWASTIIK technology against two proteins, one from *E. coli* and second from SARS-CoV-2 (Severe Acute Respiratory Syndrome Coronavirus-2) and to determine potential therapeutic benefits associated with essential oils. The present investigations on docking interactions, ADME (absorption, distribution, metabolism, excretion) and toxicity profiles of various active components found in essential oils such as thymol, menthol, eugenol, cinnamaldehyde,

and terpinen 4-ol can shed light on suitability of these compounds against multivirulent *E. coli* and SARS-CoV-2.

2. Experimental:

2.1 SWASTIHK technology

SWASTIHK technology is selected for the present investigation as it seems to be a sustainable methodology and assures safe drinking water⁸⁻¹¹. The process contemplates the use of essential oils and intense mixing, or hydrodynamic cavitation under ambient conditions for the disinfection of bacteria. It is effective for low to very high concentration of bacteria ($\sim 10^5$ CFU/mL) and a small concentration of essential oils, 0.05 to 0.1% (v/v) (500-1000 $\mu\text{g/ml}$) is required. Different kinds of essential oils were examined namely Ajwain oil (*Trachyspermum ammi*), Peppermint oil (*Mentha x piperita*), Tea tree oil (*Melaleuca alternifolia*) Harsingar oil (*Nyctanthes arbor-tristis*), Cinnamon leaf oil (*Cinnamomum zeylanicum*) etc for disinfection of gram-negative (*Escherichia coli*) and gram-positive (*Staphylococcus aureus*), antimicrobial-resistant (methicillin-resistant *Staphylococcus aureus*) and *Pseudomonas aeruginosa*.

2.2 In silico analysis

2.2.1 Protein structure preparation

Molecular docking studies were performed using two different proteins: the outer membrane protein A (OmpA) from *E. coli* (PDB ID: 1BXW) and S1 subunits of the receptor binding domain (RBD) from SARS-CoV-2 (PDB ID: 6M0J). Protein structures were downloaded from Protein Data bank^{5,19}. In the case of *E. coli*, outer membrane proteins (OMPs) were selected for study because they can express numerous virulence factors, such as fimH and kpsM, which are important for adhesion and survival. Similarly, in case of SARS-CoV-2 the glycoprotein (S) was examined. The protein consists of two parts: S1 – a receptor binding domain that binds to Angiotensin converting enzyme 2 (ACE2), and S2, which is responsible for fusion of cellular and viral membranes. To prepare protein for docking experiment, first co-crystallized ligands, water molecules, and cofactors were removed, and then target protein files were prepared using Auto Dock 4.2 (MGL tools 5.6). Protein active sites were recognized by literature scrutiny and structure visualization feature on PDB. In *E. coli* the major region of interest is C8E region, whereas in SARS-CoV-2 the region of interest is S1 subunits of the receptor binding domain (RBD). Further, to define the search space within the protein, AutoDock Vina needs a grid box encompassing the region of interest (active site)

within the macromolecule²⁰. The grid box size (Å°) for outer membrane protein A (OmpA) of *E. coli* was set at 86.51, 54.52, 26.2 for x, y and z respectively, and the grid center was set to, -19.80, 0.167 and 9.66 for the coordinates x, y and z respectively. The grid box size (Å°) for S1 subunits of the receptor binding domain (RBD) from SARS-CoV-2 was set to 104, 114 and 60 for x, y and z respectively, and grid center was set to, -21.02, -14.4 and 0.19 for the coordinates x, y and z respectively. Molecular visualization of the best docked pose was carried out by using in built docking algorithm of Auto Dock Vina. Further, the favorable protein-ligand conformations with a least potential binding energy were selected and consequently examined by Discovery studio visualizer.

2.2.2 Selection and preparation of ligands

The active components of essential oils used in SWASTIIK technology such as Ajwain oil- (thymol), Peppermint oil (menthol), Tea tree oil (terpinen 4-ol), Cinnamon leaf oil (cinnamaldehyde) was selected as ligands to check its suitability against multivirulent *E. coli* and SARS-CoV-2. The structure of ligands thymol, menthol, eugenol, cinnamaldehyde and terpinen 4-ol was downloaded from the PubChem NCBI database. The PubChem ID, 2D, 3D structures and molecular properties of all the compounds are shown in **Table 1**. The docking experiment was performed by creating 3D structures of ligands using SMILES format and saving them into MDL-MOL files, followed by creating PDB files via Open Babel²¹.

2.2.3 PreADMET analysis of active compounds

The pharmacokinetic and toxicological characteristic of all active compounds of essential oils i.e. thymol, menthol, eugenol, cinnamaldehyde, terpinen 4-ol were predicted using online PreADMET server (<https://preadmet.webservice.bmdrc.org->). A number of pharmacokinetic properties were predicted using ADME property prediction, including Caco-2 values for *in vitro* parameters of cell permeability (Caco-2 cell model), intestinal absorption (HIA value), plasma protein binding (PPB value), blood–brain barrier (BBB) penetration, and P-glycoprotein (Pgp) binding parameters. Furthermore, the active compounds were virtually scrutinized to analyze its toxicological attributes such as carcinogenicity and mutagenicity using toxicity prediction tools. The results of ADMET analysis were predicted using existing literature of drug discovery studies. However, for the first time PreADMET analysis has been used to assess the effectiveness of essential oils in SWASTIIK technology.

2.2.4 Prediction of plausible health benefits and/or potential clinical application of active compounds of essential oil

The plausible health effects/application of active compounds were identified by searching the scientific literature via two different platforms PubMed and Clinicaltrials.gov. Reported data

of clinical trials on living beings for the effect of thymol, menthol, eugenol, cinnamaldehyde, terpinen-4-ol were considered.

3. Results and Discussion:

3.1 SWASTIIK technology

SWASTIIK technology reported the application of essential oils such as ajwain oil, peppermint oil, clove oil, cinnamon oil and tea tree oil, etc. in combination with hydrodynamic cavitation and/or by simple mixing for removal of harmful bacteria from water. A complete disinfection was observed using just 0.1% oil concentrations within minutes⁸⁻¹¹. Further, it can efficiently destroy different types of bacteria such as *E. coli*, *S. aureus*, antimicrobial resistant bacteria (AMR), and difficult, opportunistic pathogen *P. aeruginosa*, making it suitable for potential commercial applications of drinking water treatment as well as in rural use. An effective disinfection of pathogenic microorganisms could be attributed to the antibacterial activity of active components of essential oils, such as thymol in ajwain oil, and menthol, cinnamaldehyde, eugenol, and terpinen-4-ol in peppermint oil, cinnamon oil, clove oil, and tea tree oil, respectively, each of which plays significant role in disinfecting water. Essential oils are biological in nature and decontaminate water with high rate of degradation through biochemical reactions within living cells²². A number of essential oils exhibit antibacterial properties, but SWASTIIK technology is the first to demonstrate that these properties could be applied to drinking water treatment in the real life with satisfactory rates of disinfection. Thus, it is instructive to examine the utility of the technology with multi-virulent bacteria and emerging viruses such as *E. coli* and SARS-CoV-2 by *in-silico* analysis of active compounds (e.g. thymol, menthol, cinnamaldehyde, eugenol and terpinen-4-ol) present in essential oils against multivirulent *E. coli* and SARS-CoV-2. *in silico* study.

3.2 Molecular Docking

A Molecular docking technique helps to identify potential inhibitors of a specific protein. Molecular interactions of thymol, menthol, eugenol, cinnamaldehyde and terpinen-4-ol against multivirulent *E. coli* and SARS-CoV-2 are shown in Table 2. Molecular docking of multivirulent *E. coli* indicated that eugenol (-4.5 kcal/mol) and thymol (-3.9 kcal/mol) have the highest binding affinity and docking scores as compared to other ligands. Among all various conformations produced during docking, the conformations with the least RMSD (Root mean square deviation) were chosen. The docking poses of each ligand against multivirulent *E. coli* is shown in Figs 1-5. Eugenol formed one or more hydrogen bonds with

residues ASN 33, Thr 30, His 31, while thymol formed hydrogen bonds with Tyr 63 with bond length 1.8 Å and Thr 30 with bond length 2.1 Å. Thymol also forms Pi alkyl interactions with Lys 64 (Table 2). Cinnamaldehyde also formed hydrogen bond with His 31 and Thr 30 with bond length 2.2 and 2.5 Å. Terpinen-4-ol, and menthol also showed good binding affinity, but none of them formed hydrogen bonds with proteins. The formation of intermolecular hydrogen bonds between the active components of essential oil and amino acid residues is anticipated to exert a stronger influence on the formation of a stable protein-ligand complex, resulting more precise docking results²³. The docking results of all the ligands with SARS-CoV-2 indicated that thymol had the strongest bonding interaction with -7.2 kcal/mol but lacks hydrogen bonding interactions, whereas eugenol and cinnamaldehyde exhibited -6.5 kcal/mol affinity and did not form any hydrogen bonding interactions. The binding of thymol involves Pi alkyl interactions with Pro 415, while eugenol interacts with Lys 541, His 540, and Pro 415. Cinnamaldehyde, on the other hand, forms Pi alkyl interactions specifically with Pro 415. Additionally, menthol forms a hydrogen bond interaction with Ser 420, with a bond length of 3.2 Å, although it exhibits a lower binding affinity in case of SARS-CoV-2. The protein-ligand interactions and residue information are summarized in Table 2. Kulkarni et al.¹⁹ also confirmed the absence of hydrogen bond interactions with thymol, eugenol, for COVID protein. However, in the present study, an amino acid interacted differently than reported by Kulkarni et al.¹⁹, and, the reason for this discrepancy remains unclear. Jani et al.²⁴ found that the interacting residues on the surface of the RBD domain of the SARS-CoV-2 spike protein were Tyr505, Gly502, Asn501, Thr500, Gln498, Gln493, Tyr489, Asn487, Phe486, Ala475, Phe456, Leu455, Tyr453, Tyr449, Gly446 and Lys417. Further, Li et al.²⁵ determined that important amino acids of RBD S-protein of SARS-CoV-2 were found between Gly354, Lys353, Asn330, Glu329, Gln325, Asn90, Tyr83, Met82, Leu79, Leu45, Gln42, Tyr41, Asp38, Glu37, His34, Lys31, Thr27, Gln24. According to Sahlan et al.²⁶ it might be that the different docking algorithms and scoring functions of each simulation were the most likely causes of the differences.

Figs. 6-10 clearly display the binding efficiencies of all of the ligands to SARS-CoV-2 protein along with their molecular interaction. Eugenol and thymol appear to act most effectively against both microorganisms, although SARS-CoV-2 showed better performance with a high potential energy (-7.2 kcal/mol) compared to multi-virulent *E. coli* (-4.5 kcal/mol). Accordingly, SWASTIIC technology can be considered to have potential activity at combating viruses, including SARS-CoV-2. The active compounds have already been proven to eliminate various pathogenic bacteria⁸⁻¹¹. Biologically active compounds are being

increasingly reported for eliminating drug resistant bacteria and viruses. Numerous researchers have sought to identify essential oils that can be applied as safe substitutes for germicides in order to moderate or completely impede bacterial growth. Recently, Elfaky et al.⁵ reported molecular docking study and mice protection assay of active ingredient of the essential oil and stated promising role of thymol, eugenol and curcumin for combating multi virulent *E. coli*. Further, Benencia et al.²⁷ reported eugenol, the active ingredient of clove oil has virucidal activity against human herpes virus, while Terstappen et al.²⁸ noted antiviral activity of clove and oregano oils against polio, coxsackie virus B1, and adenovirus type 3. Kulkarni et al.¹⁹ carried out *in silico* analysis of the active components of plant essential oils and found that cinnamaldehyde, carvacrol, thymol and pulegone etc. have ability to hinder the covid viral spike protein. Nazzaro et al.²⁹ also reported that some essential oils such as rosemary, oregano etc. are effective against *E. coli*, *S. aureus*, *B. cereus* and *Salmonella* sp. but less effective against *Pseudomonas* sp. Essential oils have different binding efficiencies against different microorganisms, and it is essential to select the appropriate oil when seeking antibacterial/antiviral action or disinfection. Thus, molecular docking study can help in the screening of potential active compound against specific pathogens and to prove utility of SWASTIIK technology.

3.3 PreADMET analysis and toxicity assessment

The absorption, metabolism, distribution and toxicity parameters of all five compounds were assessed using the online PreADMET server. The calculated parameters of all active compounds i.e. thymol, menthol, eugenol, cinnamaldehyde and terpinen 4-ol are summarized in Table 3. In general, ADMET properties can be predicted during drug discovery, but in this study, PreADMET analysis was applied to evaluate the efficacy of essential oils used in SWASTIIK technology and to determine how the active components of each essential oil are processed by living organisms. The predicted absorption values for Caco-2 cell permeability were observed to be 23 to 50, henceforth all compounds considered for the study were moderately penetrable (Table 3). In addition, the predicted HIA value for all compounds were observed to be above 95 %, indicating that the compounds were well absorbed through the intestinal cells. Sahar et al.³⁰ stated that maximum intestinal absorption is essential for the absorption of any drug or phytochemical taken orally, since it represents the primary site of absorption for any oral medication. The predicted PPB values of all tested compounds were 100 %, indicating a strong binding, except cinnamaldehyde which had a value of 52.8%, indicating a weak binding³¹. The compounds tested were all inhibitors of P glycoprotein

(PgP), and the inhibition can increase the bioavailability of susceptible molecules. If all the tested compounds pass by all the ADMET properties, it could be said that the compounds are suitable for further clinical trials or for applicability of SWASTIIK technology for drinking water treatment. Additional *in vitro* studies may be required to confirm this. The results of the toxicity study indicated that despite all compounds testing mutagenic in the *in-silico* AMES model, thymol and cinnamaldehyde displayed non-carcinogenicity in mice and rats, while eugenol appeared to be carcinogenic to the rat and mice. To ensure that purified water is fit for drinking, early characterization of its properties may help to eliminate compounds with unacceptable toxicity parameters. The toxicity data showed eugenol to be carcinogenic to rats and mice, but it exhibits proficient antibacterial and antiviral, and disinfection efficiency. Thus, to avoid the toxicity of eugenol in water, it is recommended to remove it through an appropriate separation technique after the disinfection or avoid use of essential oils containing eugenol, as a safer practice at this point of time.

3.4 Health benefits and/or potential clinical application of essential oil active compounds

PubMed and the Clinicaltrials.gov database were used to identify case studies illustrating the potential of active components of essential oils used in SWASTIIK technology and their potential health benefits/clinical applications. The outcome of the case studies and plausible effect of all the essential oils are represented in Table 4. It can be seen that almost all the essential compounds have antibacterial, antifungal, anticancer and antiviral activity, and have related clinical trials also. The active ingredients of ajwain oil and thyme oil are thymol, which has been useful to treat upper respiratory tract infections such as common cold, sinusitis, pharyngitis, bruises, and sprains, as well as applied as a remedy in coughs caused by colds and also used as disinfectants in dentistry³². Thymol has antifungal, antioxidant, and anticancer properties as well as shows antibacterial activity on Gram-positive and Gram-negative bacteria, while showing antiviral activity on herpes simplex virus type I, human rhinoviruses and influenza viruses³³⁻³⁵. Thymol also has anti-inflammatory properties as reported by Zhou et al.³⁶, who examined the effects of thymol on allergic inflammation in ovalbumin-induced mice asthma (OVA) and conclude that pretreatment with thymol bring down OVA-specific IgE antibody in mice and decreased the values of interleukins (i.e. IL-4, IL-5, and IL-13) thereby recommending its application for the treatment of allergic asthma. The efficacy of thymol as a drug for treating high-fat diet (HFD)-induced obesity in rats was demonstrated by Rafiul Haque et al.³⁷. The use of thymol to treat obesity has also been supported by some clinical trials (Table 4). Further, eugenol an active ingredient in clove oil,

has been reported to have multiple applications in dental procedures such as cementing temporary prostheses and restoring teeth and cavities³⁸. The application of propolis, clove oil, and chlorhexidine for managing tooth caries has also been studied clinically. Hussain et al.³⁹ suggested that eugenol enhances the anticancer activity of drug gemcitabine and help to reduce the level of carcinogenic and inflammatory activities in human cervical cancer cells. The wide range of eugenol activities includes antimicrobial, anti-inflammatory, analgesic and antioxidant have been reported by several authors^{40, 41}. Recently, Naz et al.⁴¹ evaluated the strong interactivity of human serum albumin (HAS) and SARS-CoV-2 against eugenol for novel COVID-19 drug discovery. Eugenol is recommended as a safe for consumption, but excessive amounts of clove oil (ten to thirty milliliters) can result in coma, acidosis, respiratory depression and, in some cases, severe hypoglycemia requiring ventilation and intravenous glucose⁴². Several characteristics and activities of eugenol have not yet been discovered and should be investigated further *in vitro* and *in vivo* through comprehensive research on human trials. Furthermore, the antibacterial and antiviral activity of cinnamaldehyde and terpinen-4-ol have also been well documented in the research articles^{43,44}. Cinnamaldehyde was found to be not toxic to vertebrates or invertebrates in an *in vivo* trial conducted by Alves et al.⁴⁵. Subash Babu et al.⁴⁶ found that oral administration of cinnamaldehyde in induced diabetic rats produces a significant antihyperglycemic effect and simultaneously help to reduce total cholesterol and triglyceride levels effect. In addition, several studies have demonstrated terpinen 4-ol's usefulness as an anticancer agent^{47,48}. Clinical trials on the use of terpinen 4-ol for treatment of Demodex Blepharitis eye disease were described in the previous reports. Furthermore, Freires et al.⁴⁹ stated that menthol and eugenol demonstrate antibacterial properties specific to cariogenic bacteria. According to the clinical trials database, menthol may be useful as an antipruritic, an analgesic, and an anticancer agent (Table 4).

According to the aforementioned/ discussed clinical trials and experiments, it is evident that the study can provide insight into a therapeutic relationship between active components of essential oil used in SWASTIHK and their potential benefits. It is important to note that each oil has a different application and health effect. Some of oil also showed toxicity in certain amount, hence it is essential to appropriately implement the devised methodology for separation of the oil from the treated water, where required. A suitable dosage of the oil may also be selected or with a specific oils mix, depending on its nature and requirements of the individual or environment. Formulations of different essential oils may be useful in this respect in order to meet the expectations of both disinfection and health benefits. It is

obligatory to perform detailed *in vitro* and *in vivo* long-term studies in this regard, and controlled separation of oils may be recommended till medical experts validate and consider the health benefits. It may be noted that studying Ayurveda enhances the effectiveness of the SWASTIIK technology and highlights the relevance of traditional knowledge in water treatment and human wellness. The use of natural compounds such as thymol, eugenol, cinnamaldehyde etc in water disinfection can be seen as an extension of the traditional knowledge of Ayurveda, utilizing the inherent properties of essential oil for practical applications in promoting health and well-being.

Conclusions

Molecular docking study indicated that eugenol and thymol exhibited the highest efficacy and demonstrated potential activity against SARS-CoV-2 and multivirulent *E. coli*. However, SARS-CoV-2 displayed superior performance with a high binding affinity value of -7.2 kcal/mol, surpassing multi-virulent *E. coli*, which had a potential energy of -4.5 kcal/mol. The ADMET studies showed that all active compounds exhibited good absorption properties. *In silico* techniques can be advantageous in the selection of innovative essential oils, suitable for drinking water treatment, through virtual screening. The present study provides a useful and innovative strategy to save time and resources and for speedy classical microbiological studies especially used in water disinfection.

Acknowledgement

The author-VMB wishes to acknowledge the financial support from Department of Science and Technology, Ministry of Science and Technology, India Water Innovation Center-Technology, Research and Education (WICTRE) (DST/TM/WTI/WIC/2K17/100(G)), and also financial support from Council of Scientific and Industrial Research (CSIR), Government of India (MLP102326).

Figures:

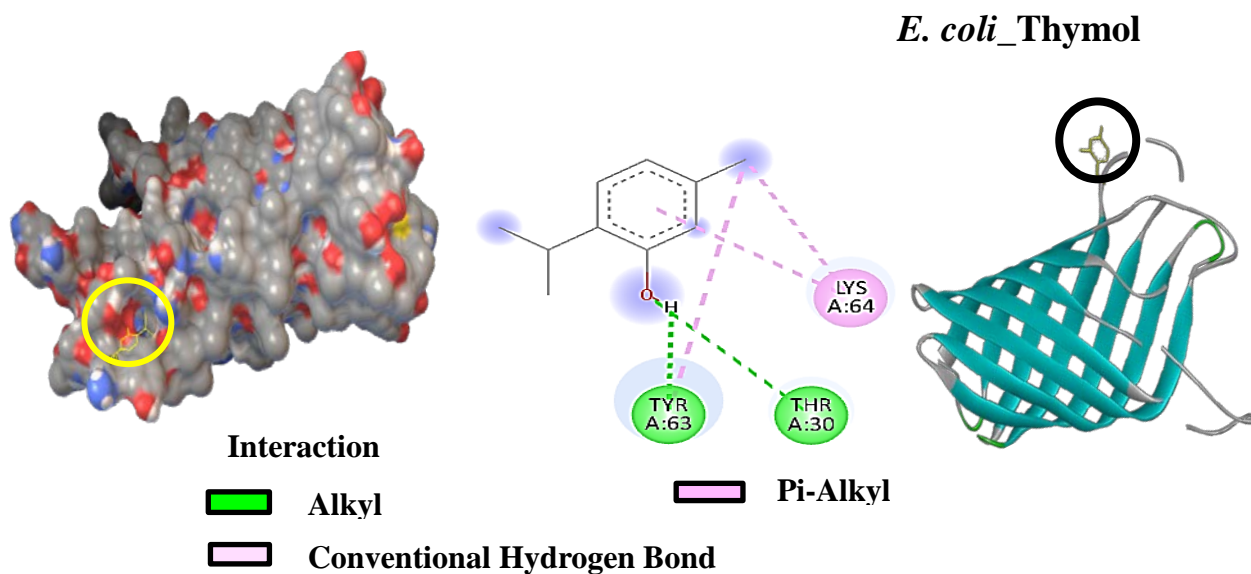


Fig. 1 Molecular interactions of ligand thymol with multi virulent *E. coli*

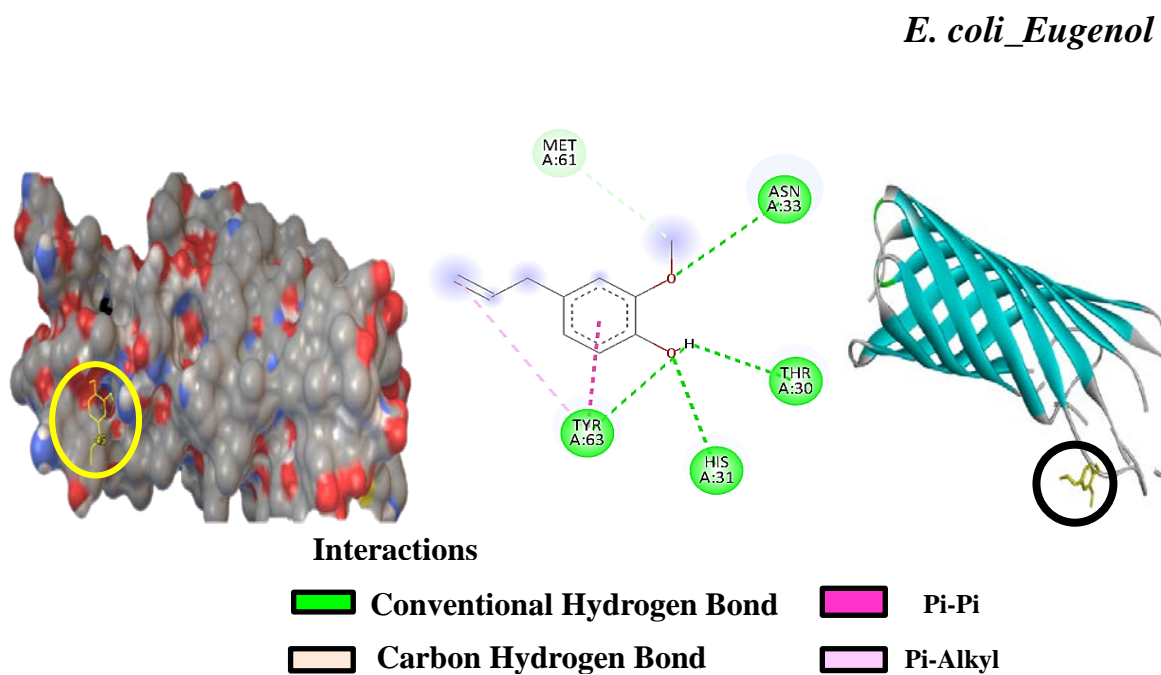


Fig. 2 Molecular interactions of ligand eugenol with multi virulent *E. coli*

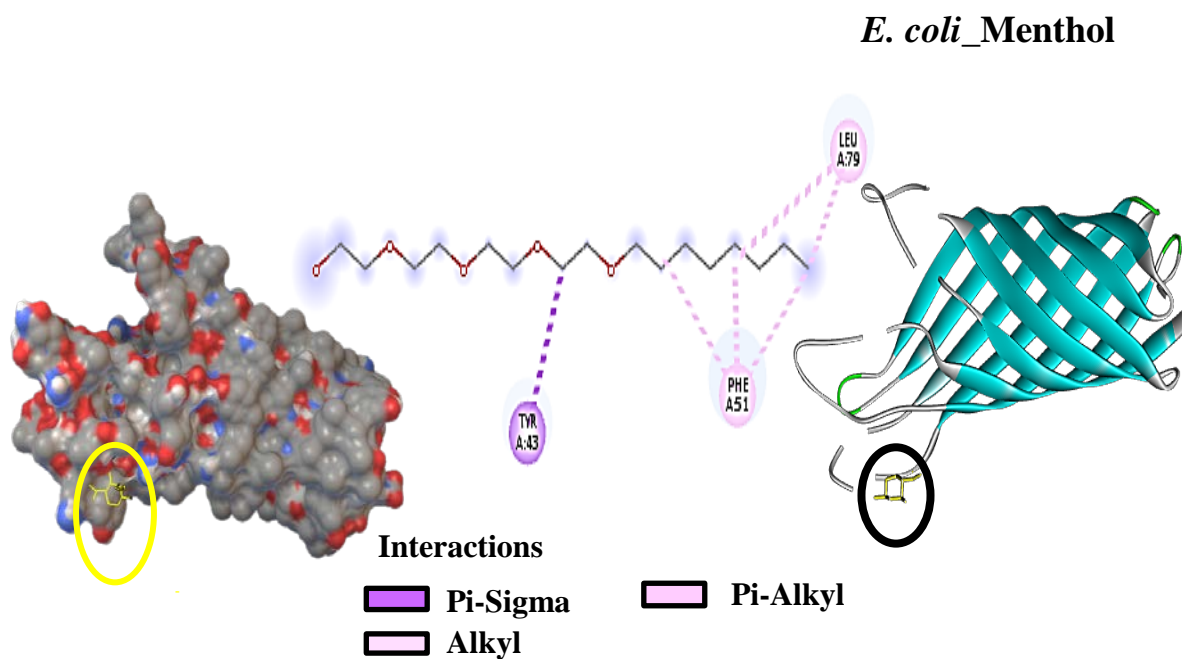


Fig. 3 Molecular interactions of ligand menthol with multi virulent *E. coli*

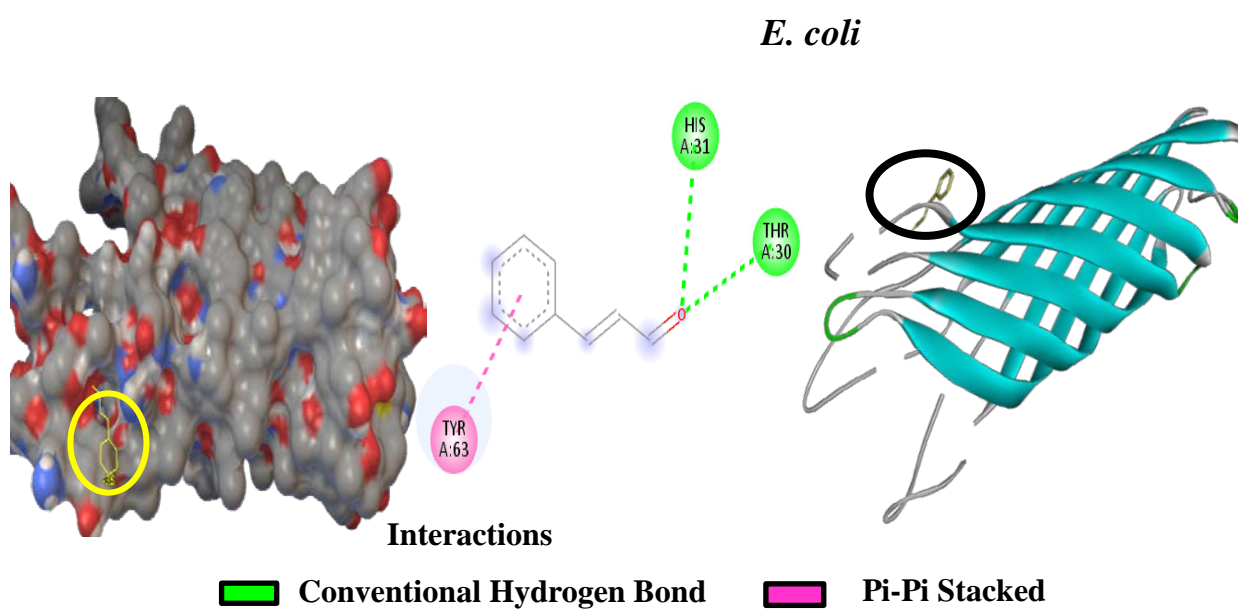


Fig. 4 Molecular interactions of ligand cinnamaldehyde with multi virulent *E. coli*

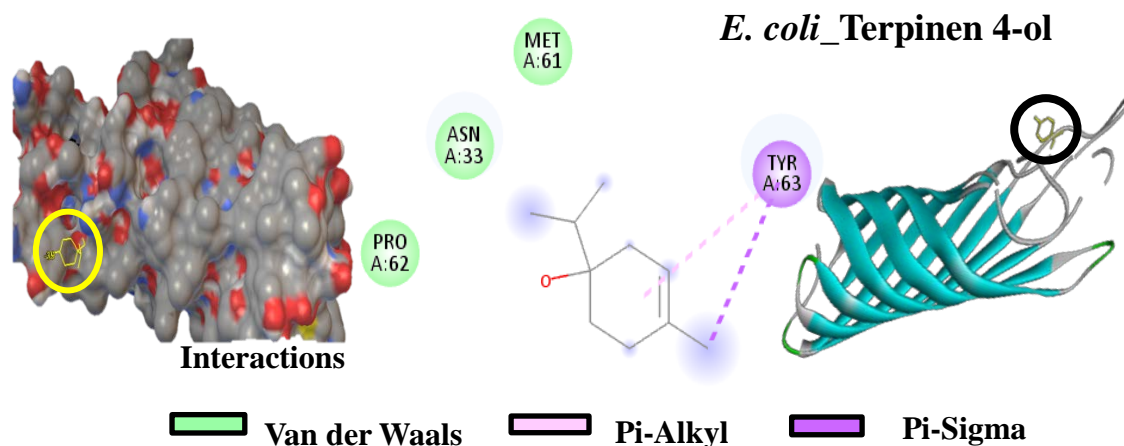


Fig. 5 Molecular interactions of ligand terpinen 4-ol with multi virulent *E*

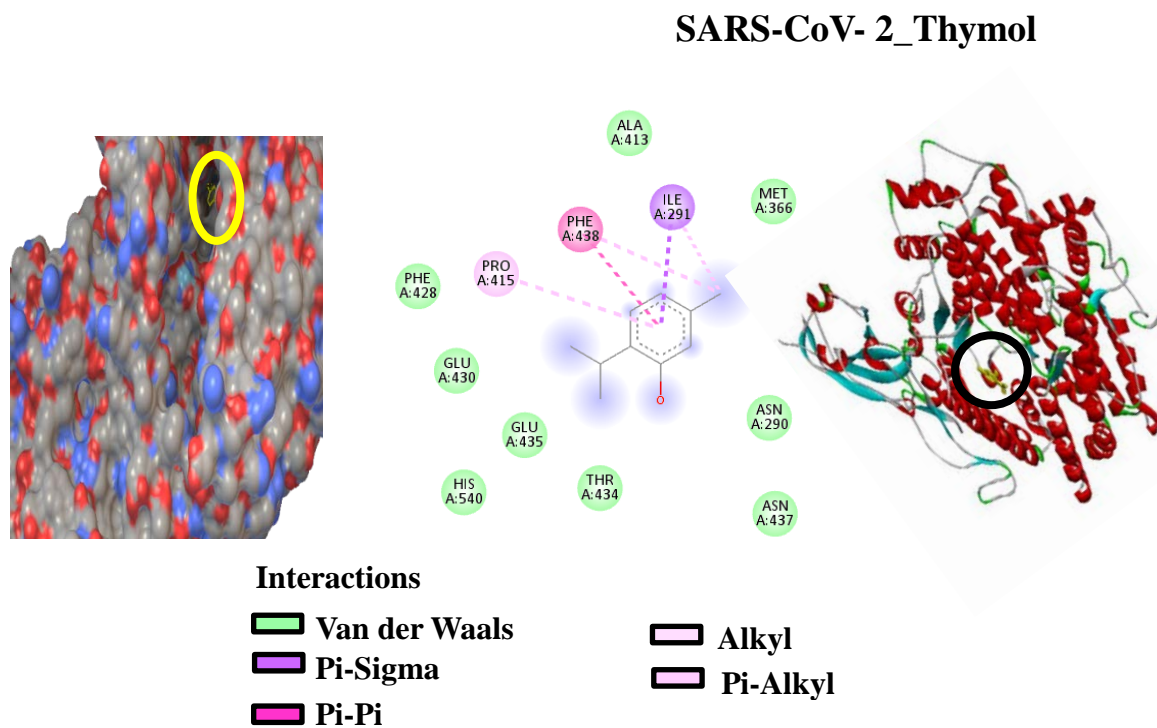


Fig. 6 Molecular interactions of ligand thymol with SARS-CoV-2

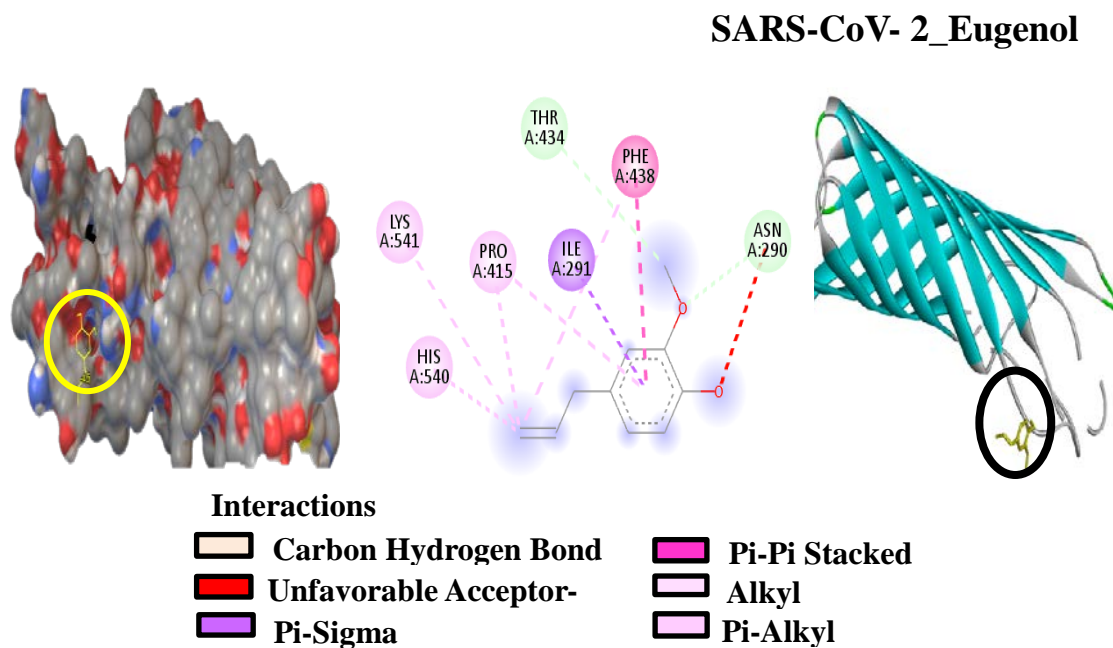


Fig. 7 Molecular interactions of ligand eugenol with SARS-CoV-2

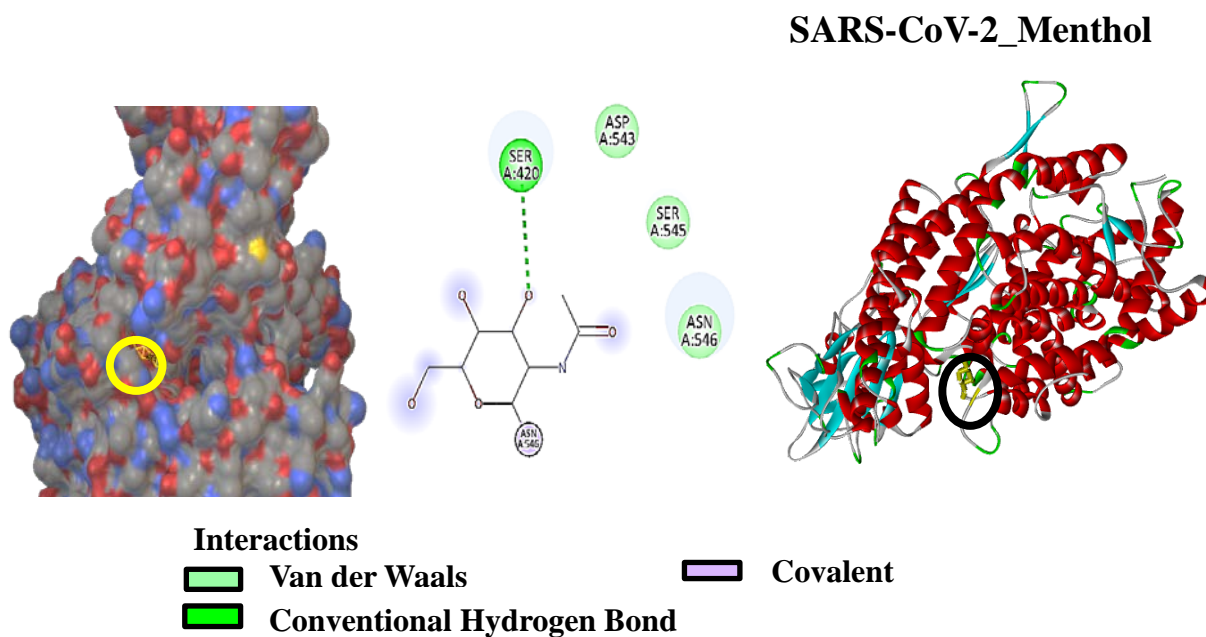


Fig. 8 Molecular interactions of ligand menthol with SARS-CoV-2

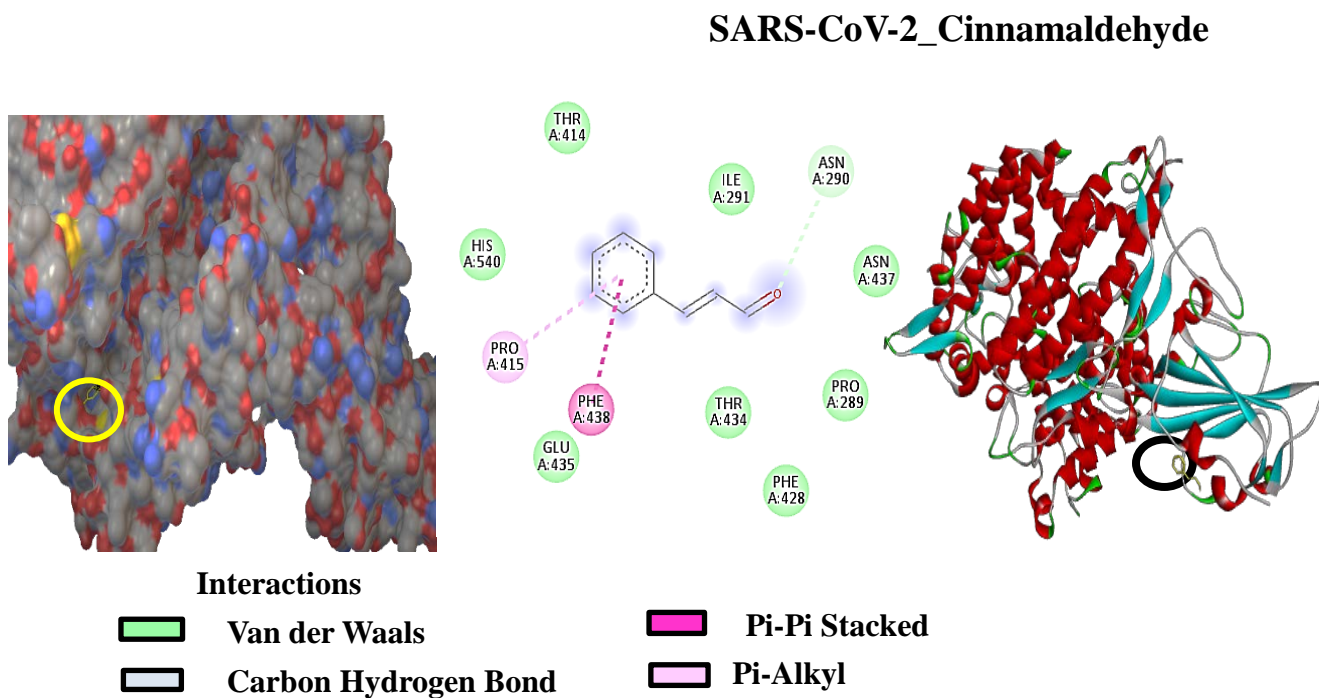


Fig. 9 Molecular interactions of ligand cinnamaldehyde with SARS-CoV-2

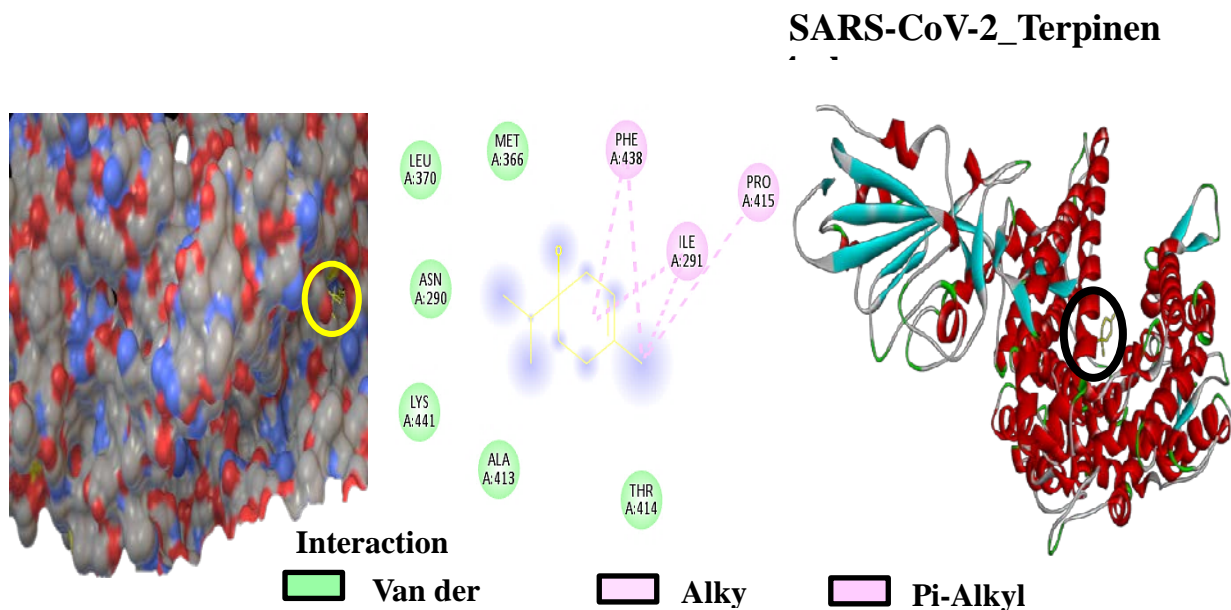


Fig. 10 Molecular interactions of ligand terpinen-4-ol with SARS-CoV-2

Tables:

Table 1: Molecular properties and structure of active components

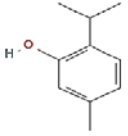
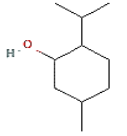
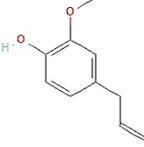
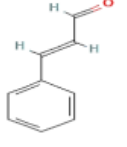
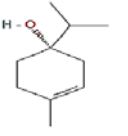
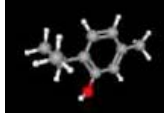
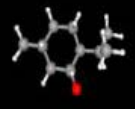
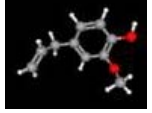
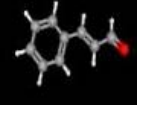
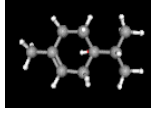
Properties	Thymol	Menthol	Eugenol	Cinnamaldehyd	Terpinen 4-ol
PubChem ID	6989	1254	3314	637511	2724161
Molecular Formula	C ₁₀ H ₁₄ O	C ₁₀ H ₂₀ O	C ₁₀ H ₁₂ O ₂	C ₉ H ₈ O	C ₁₀ H ₁₈ O
Molecular Weight	150.22	156.26	164.2	132.16	154.25
Log P	3.3	3	2	1.9	2.2
2 D structure					
3 D structure					

Table 2: Molecular interactions of active component with Multi virulent *E. coli* and SARS-CoV-2

Organism Name: Multivirulent <i>E. coli</i> (PDB ID 1BXW)					
			Type of Interaction		
Compound Name	Affinity (kcal/mol)	Hydrogen Bond	Pi alkyl	Van dar Waals	Pi Sigma
Thymol	-3.9	Tyr 63, Thr 30	Lys 64	-	-
Menthol	-3.4	-	Liu 79, Phe51	-	Tyr 43
Eugenol	-4.5	ASN 33, Thr 30, His 31	Tyr 63	-	-
Cinnamaldehyde	-3.8	His 31, Thr 30	-	-	Tyr 63
Terpinen 4-ol	-3.9	-	-	Met 61, Asn 33, Pro 62	Tyr63
Organism Name: SARS-CoV-2 (PDB ID: 6M0J)					
			Residual Interaction		
Compound Name	Affinity (kcal/mol)	Hydrogen Bond	Pi alkyl	Van dar Waals	Pi Sigma
Thymol	-7.2	-	Pro 415	Ala413, Met 366, Asn 290, Asn 437, Thr 434, His 540, Glu 435, Phe 428	Ile 291
Menthol	-5.2	Ser 420	-	Asp 543, Ser 545, Asn 546	-
Eugenol	-6.5	-	His A540, Lys A 541	-	ILE 291
Cinnamaldehyde	-6.5	Asn 290	Pro 415	Thr 414, His 540, Glu 435, Thr 434, Phe 428, Pro 289, Asn 437, Ile291	-
Terpinen 4-ol	-5.8	-	Phe 438, Pro 415	Met 366, Leu 370, Asn 290, Lys 441, Ala 413, Thr 414	-

Table 3: ADMET and toxicity analysis of active compounds

Properties	Thymol	Menthol	Eugenol	Cinnamaldehyde	Terpinen 4-ol
Blood Brain Barrier (BBB)	5.53	6.25	2.25	1.26	5.53
CaCO₂	50.8	39.49	46.88	23.78	50.8
CYP_3A4 inhibition	Non	Inhibitor	Non	Non	Non
Human Intestinal Absorption (HIA (%))	100	100	96.77	100	100
Plasma protein binding (PPB)	100	100	100	52.89	100
P glycoprotein (Pgp) inhibition	Non	Non	Non	Non	Non
	Toxicity				
AMES Test	Mutagen	Mutagen	Mutagen	Mutagen	Mutagen
Carcino_Mouse	Negative	Negative	Positive	Negative	Positive
Carcino_Rate	Negative	Positive	Positive	Negative	Negative

Table 4: Application/health benefits of active components of essential oils

Active Ingredients	Plausible application/health benefits	Exemplary Studies (PMID)	Clinical trials.gov.in
Thymol	antioxidant	29799283	Thymol on Netrin-1 on Obese Patients NCT05427721 (Phase 2)
	anti-inflammatory	26553130, 24785965	A Study to Evaluate the Effect and Tolerance of Musclin™ (Thymol) in Healthy Subjects NCT03767504
	Antimicrobial, antiviral	26546890, 36093954	-
	Antidiabetic, antiobesity, Neuropharmacological, antihyperglycemic and hypolipidemic	26680107, 29635674, 24486068, 29069225, 26007642	-
Menthol	Antipruritics, Pain and analgesia	29524352, 36277488	1. Addiction and Behavior Related to Menthol Cigarette Substitutes NCT04844762 2. Menthol for PDT Pain Relief NCT02984072 (Phase 4)
	Anticancer	35467269, 35950244	Topical Menthol Application in Chemotherapy-Related Peripheral Neuropathy in Patients with Breast Cancer NCT05429814
Eugenol	Preventing chronic diseases such as cancer, inflammatory reactions, and other conditions	27771920	Using a Mouthwash Containing Propolis, Clove Oil and Chlorhexidine to Improve the Caries Risk of high-risk Patients NCT03553628
	Anti-inflammatory, anti-oxidant	30425782	Endodontic Medications for Irreversible Pulpitis: Articaine or Eugenol NCT03472456
	Antiviral	36636828, 36450916, 36151910, 35684363, 35836934	-
Cinnamaldehyde	Antioxidant	31735467	Safety and tolerability of cinnamaldehyde in orabase for oral candidiasis treatment: phase I clinical trial (PMID: 35305150)
	Antiviral, antibacterial, antifungal, anticancer, anti-diabetic	35508082, 34722758, 27771918, 17140783	The Effect of Capsaicin and Cinnamaldehyde on Intestinal Permeability. NCT01667523
Terpinen 4-ol	antibacterial, antifungal, antiviral	32630600, 31111285, 19843207, 35744913	Demodex Blepharitis Treatment Study NCT01647217 (Phase 1)
	Anticancer, anti-arthritis	35322742, 28781645, 27275783, 35320496	-

References:

1. V.V. Ranade, V.M. Bhandari, S. Nagarajan, V.P. Sarvothaman, A.T. Simpson, Hydrodynamic cavitation: Devices, Design, and Applications. Disinfection of water, Wiley 145, 2022.
2. M. Cerecedo, C. Dopazo, Rafael Gomez-Lus., Ultrason. Sonochem., 48, 71, 2018.
3. WHO, Quantitative microbial risk assessment: application for water safety management, WHO Press., 187, 2016 (<http://www.WHO.>).
4. WHO, WHO guidelines for drinking water quality: first addendum to the fourth edition, 2017.
5. M. Elfaky, M. Abdel-Hamid, E. Khalifa, W.A. Alshareef, R.A. Mosbah, S.T., Elazab, M.M. Ghoneim, M.M. Al-Sanea, M.M. Bendary, Appl. Microbiolo. Biotech. 106, 691, 2022.
6. T.P.K. Murthy, T. Joshi, S. Gunnan, N. Kulkarni, V.P. Kumar, S.B. Gowrishankar, Curr. Res. Green Sustain. Chem. 4, 10059, 2021.
7. H.N. Tran, G.T. Le, D.T. Nguyen, R.S. Juang, R.J. Bhatnagar, E.C. Lima, H.M.N. Iqbal, A.K. Sarmah, H.P. Environ Res. 193, 110265, 2021.
8. M.B. Mane, V.M. Bhandari, V.V. Ranade, J. Water Process Eng. 43, 102280, 2021.
9. M.B. Mane, V.M. Bhandari, K. Balapure, V.V. Ranade, Ultrason. Sonochem. 61, 104820, 2020.
10. M.B. Mane, V.M. Bhandari, K. Balapure, V.V. Ranade. Ultrasonics Sonochemistry, 69, 105272, 2020
11. Dixit, D., Bhandari, V.M., Mane, M.B., Balapure, K. Biochem. Eng. J. 187, 108631, 2022.
12. P. Jain, V.M. Bhandari, K. Balapure, J. Jena, V.V. Ranade, D.J. Killedar, J. Environ. Manage. 242, 210, 2019.
13. V.V. Ranade, V.M. Bhandari, Industrial Wastewater Treatment, Recycling, and Reuse, in: Ind. Wastewater Treat. Recycl. Reuse, Elsevier, 1–80, 2014.
14. F. Nazzaro, F. Fratianni, R. Coppola, V. Feo, pharmaceuticals (Basel).10, 86, 2017.
15. X.Y.Meng, H.-X. Zhang, M. Mezei, M. Cui, Curr Comput Aided Drug Des. 7, 146, 2011.
16. M.A. Mbock, R.G. Kamkumo, R. Shukla, W.F. Fouatio, P.V.T. Fokou, F.N. Tsofack, C.D. Noussi, R. Fifen, A.E. Nkengfack, T.R. Singh, B.L. Ndjakou, N. Sewald, F.F. Boyom, J.J.E. Ngang, O. Boyomo, Dimo, J. Ethnopharmacol. 307, 116209, 2023.
17. L. Ralte, L. Khiangte, N.M. Thangjam, A. Kumar, Y.T. Singh, Sci. Rep. 12, 3395,

- 2022.
18. V. Puthanveedu, K. Muraleedharan, *Struct. Chem.* 33, 1423, 2022.
 19. S.A. Kulkarni, S.K. Nagarajan, V. Ramesh, V. Palaniyandi, S.P. Selvam, T. Madhavan, *J. Mol. Struct.* 1221, 128823, 2020.
 20. M. Aliye, A. Dekebo, H. Tesso, T. Abdo, R. Eswaramoorthy, Y. Melaku, *Ocimum cufodontii*. *Sci. Rep.* 11, 10101, 2021.
 21. G.M. Morris, H. Ruth, W. Lindstrom, R.K. Belew, D.S. Goodsell, A.J. Olson, *J. Comput. Chem.* 30, 2785, 2009.
 22. T. Hou, S. Sana, H. Li, Y. Xing, A. Nanda, Vasudeva Reddy Netala, Zhijun, Sankar Sana, Z. S., Li, H., Y. Xing, A. Nanda, V. Reddy Netala, Z. Zhang, *Food Bioscience* 47, 101716, 2022.
 23. M.Y.Wu, D.Q. Dai, H. Yan, H. Proteins *Struct. Funct. Bioinforma.* 80, 2137, 2012.
 24. V. Jani, S. Koulgi, V.N. Uppuladinne, U, Sonavane, R, Joshi, *ChemRxiv*. 2020.
 25. F. Li, W. Li, S.C. Farzan, M. Harrison, *Science* 309, 1864, 2005.
 26. M. Sahlan, L.K. Dewi, D.K. Pratami, K. Lischer, H. Hermansyah, *Int. J. Technol.* 14, 387, 2023.
 27. F. Benencia, M.C. Courreges, *Phytother Res.* 14, 1099, 2000.
 28. A. Terstappen, *Trends Pharmacol. Sci.* 22, 23, 2001.
 29. F. Nazzaro, F. Fratianni, L. De Martino, R. Coppola, V. De Feo, *Pharmaceuticals.* 6, 1451, 2013.
 30. G. Sahar Elbager, Abdelrahman H. Abdelmoneim, et al., *ChemRxiv*, 12235181, 2020.
 31. Finch and Pillans, *Aust Prescr* 37, 137–139, 2014.
 32. A. Kowalczyk, M. Przychodna, S. Sopata, A. Bodalska, I. Fecka, *Molecules.* 25, 4125, 2020.
 33. M. Sun, R. Yao, Y. You, S. Deng, W. Gao, *Front. Environ. Sci. Eng.* 1, 95, 2007.
 34. L. Deng, M. Taxipalati, P. Sun, F. Que, H. Zhang, *Colloids Surfaces B: Biointerfaces,* 136, 859, 2015.
 35. K. Rajamanickam, T. Rathinavel, V. Periyannan, S. Ammashi, S. Marimuthu, M. Nasir Iqbal, *J. Biomol. Struct. Dyn.* 7386, 2022.
 36. E. Zhou, Y. Fu, Z. Wei, Y. Yu, X. Zhang, Z. Yang, *Fitoterapia* 96, 131, 2014.
 37. M. Rafiul Haque, S.H. Ansari, A.K. Najmi, M.A. Ahmad. *Toxicol Mech Methods.* 24, 116, 2014.
 38. I. Padhy, P. Paul, T. Sharma, S. Banerjee, A. Mondal, *Life* 12, 1795, 2022.
 39. A. Hussain, K. Brahmhatt, A. Priyani, M. Ahmed, T.A. Rizvi, C. Sharma, *Cancer*

- Biother. Radiopharm. 26, 519, 2011.
40. J.N. Barboza, C. da Silva Maia Bezerra Filho, R.O. Silva, J.V.R. Medeiros, D.P. de Sousa, *Oxid. Med. Cell. Longev.* 3957262, 2018.
 41. F. Naz, I. Khan, S. Baammi, A. Islam, *J. Biomol. Struct. Dyn.* 41, 10161, 2023.
 42. J. H. Hoofnagle, J. Serrano, J.E. Knoben, V.J. Navarro, *Hepatology* 57,873, 2013.
 43. A. Nag, R. Banerjee, S. Paul, R. Kundu, *Computers in Bio Medicine* 146, 105552, 2022.
 44. A. Garozzo, R. Timpanaro, B. Bisignano, P.M. Furneri, G. Bisignano, A. Castro, *Lett. Appl. Microbiol.* 49, 806, 2009.
 45. D.D.N. Alves, R.X. Martins E.D.S Ferreira, A.F. Alves, J.C. Andrade, T.M. De, Batista, J.G. Lazarini, L.S. Amorim, P.L. Rosalen, D.F. Farias, R.D. De Castro, *Biomed Res. Int.* 2305695, 2021.
 46. P. Subash Babu, S. Prabuseenivasan, S. Ignacimuthu, *Phytomedicine* 14, 15, 2007.
 47. W. Cao, R. Tian, R. Pan, B. Sun, C. Xiao, Y. Chen, Z. Zeng, S. Lei, *Bioengineered* 13, 8643, 2022.
 48. K. Nakayama, S. Murata, H. Ito, K. Iwasaki, M.O. Villareal, Y.W. Zheng, H. Matsui, H. Isoda, N. Ohkohchi. *Oncol. Lett.* 14, 2015, 2017.
 49. I.A. Freires, C. Denny, B. Benso, S.M. De Alencar, P.L. Rosalen, *Molecules*, 20, 7329, 2015.

Photocatalytic Studies on Zinc Oxide Nanoparticles Doped with Selenium and Silicon Dioxides for Photodegradation of Lasix Drug

L.Ramapriya^{1*} and J.Santhanalakshmi²

¹Department of Chemistry, Dr.M.G.R. Educational and Research Institute, Chennai

²University of Madras, Guindy Campus, Chennai, Tamilnadu, India.

*Email: toramapriya@gmail.com

Received: 20.7.2023, Revised: 2.11.2023, Accepted: 18.11.23

ABSTRACT

Metal oxide nanoparticles have taken a broad area of intense research because of their unique properties and application in diversified fields. Zinc oxide (ZnO) nanoparticles show varied morphologies and significant activities especially after doped with different metals. In this work, ZnO nanoparticles, Selenium dioxide (SeO₂) doped Zinc oxide nanoparticles and Silicon dioxide (SiO₂) doped Zinc oxide nanoparticles are synthesised by sol-gel method. The dopant effect on ZnO for band gap energy, crystal size and morphology are investigated by analysing the UV-DRS, powder X-ray diffraction and FESEM measurements respectively. The photocatalytic activities of these synthesised nanoparticles are compared by subjecting them into degradation of drug Lasix (furosemide) under UV and Solar irradiation sources. The progress of drug degradation is studied by measuring absorbance versus time interval at constant wavelength (325 nm) of the drug. The rate coefficient values found in this oxidative (H₂O₂) and reductive (NaBH₄) catalytic degradation process of the drug is found efficient in solar irradiations. The results of characterisation studies and the order of photocatalytic activities of the nanoparticles are discussed.

Keywords: ZnO nanoparticles, selenium dioxide doped ZnO nanoparticles, silicon dioxide doped ZnO nanoparticles, drug degradation

Introduction

In recent years, use of drugs to fight against infections and chronic illness has become unavoidable. The emergence of many chemically compounded drugs in medicine field has also increased more discharge in the environments. Especially, the water resources are contaminated with the discharge of popularly used drugs and those from the pharmaceutical manufacturing units¹. Degradation followed by mineralisation of the water soluble drugs in trace amounts is mostly a slow process in nature. Heterogenous photocatalysis using nano crystalline semiconductors has emerged as a potential and developing advanced oxidation processes used in the remediation of industrial polluted water

effluents². Many transition metal oxides are used as catalysts for these processes^{3,4}. In the present work, the use of photoactive metal oxides nanomaterials such as ZnO has been chosen to catalyse photo assisted degradation of Lasix a diuretic class of drug composed of furosemide.

The oxides of the p block elements were opted to dope so that the doping will activate the hole-pair movements during photo catalysis of ZnO⁵⁻⁹. ZnO doped with selenium also have photoelectronic properties and contribute to the crystallite size¹⁰⁻¹¹. ZnO with dopants from p-block elements Selenium and Silicon were synthesised as nanoparticles and their photocatalytic activities were compared on degradation of furosemide drug. Regarding the irradiation sources, solar and UV are chosen for the study. Aqueous solutions of the drugs were used for the degradation in the oxidative degradation H₂O₂ was used while in reductive degradation NaBH₄ was used. The kinetics of degradation of the drug under the oxidation and reduction stresses was studied and the rate coefficient values were determined. Based on the kinetic parameters, the trend set in the degradation processes was evaluated. A plausible reaction pathway was formulated.

Experimental

Materials: Zinc acetate and Ethylene Glycol were purchased from Merck. Selenium dioxide and Silicon dioxide were purchased from SRL and Ethanol from Haymann. Lasix (Furosemide) was purchased from retail pharmacy store and used. Double distilled water was used all through the experiments. UV–Vis spectrometer; double beam, Techcom instrument with 1 cm path length quartz cuvettes was used. Bruker D8 advance diffractometer was used for XRD data. FESEM of the nanoparticles were measured using SU6600, HITACHI model operating at an accelerating voltage of 100 kV. Fourier transform infrared spectrometer (FT-IR Perkin-Elmer Spectrum 2000 Spectrophotometer) was used for the structural analysis. Shimadzu GCMS-QP2010 Ultra and Column: Restek; Rxi-5Sil-MS; 30 m – 25 mm ID was used for gas chromatography and mass spectra analysis in this research work.

Synthesis of Nanoparticles: Nanoparticles were synthesised by sol-gel method¹²⁻¹⁴. The nanocrystalline ZnO was prepared by dissolving the precursor zinc acetate powder in water. To this precursor solution, ethylene glycol (10% v/v of solution) was added in drops under stirring as a stabiliser and the stirring was continued for 1 h at 80 °C. The reaction mixture is cooled, centrifuged and the centrifugate is dried initially at about 80 °C and then annealed at 600-650 °C for 3 hrs.

The doped ZnO nanoparticles were prepared as 10% stoichiometric ratios of dopants precursors and Zinc acetate dissolved in solvents water and ethanol accordingly. The precursors were Selenium dioxide and Zinc acetate for Selenium doped ZnO; Silicon dioxide and Zinc acetate for Silicon dioxide doped Zinc oxide nanoparticles. The two corresponding precursor solutions were mixed under constant stirring and synthesis was continued as for undoped ZnO synthesis.

Photocatalytic studies: 0.5 mM Lasix solution was prepared using water. 1 mg / 20 mL of catalyst to Lasix solution was used for all photocatalytic studies. For oxidative conditions H₂O₂ (30%) 1.0 mL and in reductive conditions, NaBH₄ (10%) 10 ml were used. All the solutions were prepared freshly and used. One pot batch type reactor with the nanomaterial and the substrate solution was set up. For this mixture with and without the addition of Hydrogen peroxide / Sodium borohydride, the absorbance maxima with respect to wavelength were recorded and this wavelength maxima (325 nm) was kept constant while the absorbance change during irradiation was recorded at definite intervals of time. The reaction mixture was irradiated with UV emitting lamps for UV irradiations (~250 nm). For solar irradiation, the reaction mixture was exposed to direct visible light. Absorbance variation plots were made. The kinetic plots for the rate constant determination were drawn from log (OD₀/OD_t) versus time data. The pseudo-first order rate coefficient values were determined by multiplying 2.303 with the slopes of the linear kinetic plots.

GC MS analysis: The kinetics of degradation of Lasix was monitored by measuring the change in absorbance values respective to the drug. Though the change in absorbance values directly reflects the change in concentration of the substrate, the degradation of compound and the formation of fragments were confirmed through GC instrument equipped with Mass analyser^{15,16}. The column oven temperature was 40 °C and the sample was injected at 280 °C. The analysis was done with following specifications; Pressure :49.7 kPa, Total Flow :54.1 mL/min and Column Flow: 1.00 mL/min with Linear Velocity :36.1 cm/sec and Purge Flow :3.0 mL/min. The fragments separated through column were subjected to mass analyser where the fragments produced by ionization sources (280 °C) were detected with detectors running at 0.87 kV from 50 m/z to 450 m/z.

Results and Discussion:

UV- DRS measurements: In Fig 1, UV-DRS spectra of pure ZnO nanoparticles and doped ZnO nanoparticles with variation in the dopant's nature are given. By applying the tauc

relation $\alpha hv = a(hv - E_g)^n$, where 'a' is absorption coefficient and E_g the optical band gap, the band gap energy values of nanopowders of ZnO are determined for direct band gap energy value, $n=2$ has been used. For dopants, it may be seen that band gap energy values have increased to 3.27 eV and 3.3 eV respectively for SeO_2 and SiO_2 from 3.20 eV of undoped ZnO nanoparticles (Table 1). Hence, it is clearly evident that the band gap energy values of ZnO nanopowders are tunable for increased band gap energy values by dopants¹⁷⁻²⁰. This effect can be utilised for shifting in the photocatalytic activity and photo absorption activity of ZnO nanoparticles both in solar and UV regions.

Size measurements: In Fig. 2, the powder x-ray diffractograms are presented for the undoped ZnO nanoparticles and doped ZnO nanoparticles are given. For undoped, the characteristic peaks appeared at angles (2θ) of 31.767, 34.420, 36.252, 47.537, 56.593, 62.853, 66.373, 67.944 and 69.083 corresponding to planes (0 1 0), (0 0 2), (0 1 1), (0 1 2), (1 1 0), (0 1 3), (0 2 0), (1 1 2) and (0 2 1) of hexagonal wurtzite phase; Zincite structure, space group p63mc and matches with ICSD card 76641. The lattice parameters are found to be $a = b = 3.25$ nm, $c = 5.20$ nm and $\alpha = \beta = 90^\circ$, $\gamma = 120^\circ$ respectively. For both the doped nanoparticles; similar pattern is observed, no impurity phase is found, except for change in crystallite size which was calculated from Scherrer equation ($\lambda = 1.54 \text{ \AA}$). The variation in the nano sizes of crystal sizes are found to decrease in case of dopants (Table 1). The inclusion of dopants in the crystal should have caused broad peak during diffraction (lattice disorder) resulting in decrease in the crystallite sizes²¹⁻²³. Although the crystal sizes are calculated from PXRD measurements using Scherrer equation, these inferences are visible in the FESEM photographs (Fig.3). For silicon doping bullet type elongated particles are observed to be formed. In case of selenium too, the hybrid alterations of silicon and tellurium are seen. Based on the size measurements adopted using PXRD and FESEM, the trend observed in the nano size variations among pure ZnO nanocrystals and doped ZnO crystals is as follows:

Pure ZnO nanoparticles > SeO_2 doped ZnO nanoparticles > SiO_2 doped ZnO nanoparticles

FTIR measurements: Using K-Br pellets, the FTIR spectra of pure and doped ZnO nanoparticles recorded within the range of $4000-400\text{cm}^{-1}$ are shown in Fig 4. Regarding metal oxide nanoparticles in the pure form and as well as in the doped form, FTIR spectroscopy plays a significant role in characteristic peaks of metal oxides^{24,25}. A doublet like strong peaks at 445 and 488cm^{-1} in the Fig 4 reveals that pure ZnO characteristic peak are being

present and in many literature reports, such peaks have been reported in the as synthesized condition. Upon doping, it is found that in most cases, the peaks are blue shifted and in some cases red shifted. In general, vibration bands around 445cm^{-1} to 530cm^{-1} could be assigned to Zn-O bond in the lattice. Adsorbed moisture and CO_2 in certain case may cause shifts. However, they are also reflected in the region $3200\text{-}3500\text{cm}^{-1}$ for weak O-H stretching bands. In case of SeO_2 , a doublet around 497cm^{-1} and 447cm^{-1} are observed similar to undoped ZnO nanoparticles while 1030cm^{-1} may be attributed to Se-O bond. Additionally, a broad peak at 3418cm^{-1} seen is characteristic peak of adsorbed moisture, O-H bond. Selenium imparts partial or improved hygroscopicity to ZnO lattice. Regarding Silicon dopant, the characteristic peak of ZnO is broad and a triplet each at 532, 492 and 430 cm^{-1} are detected. Among these peaks 532 cm^{-1} addition to doublet of undoped ZnO, may be due to Si-O-Zn bond vibration. Si-O-Si characteristic peak is observed at 1110cm^{-1} in the ZnO lattice. The secondary vibration of Zn-O is mostly detected around $660\text{-}670\text{cm}^{-1}$ range. The peaks lying from 1500cm^{-1} to 1700cm^{-1} and $3200\text{-}3400\text{cm}^{-1}$ represents the C-O, O-H and C-H stretching due to adsorbed surficial CO_2 and H_2O molecules. Sometimes, these peaks also suffer strong shifts due to dopants lying at the surface.

Photocatalytic degradation studies: In Fig.5 typical UV-VIS spectrum of Lasix drug in concentration of 0.5 mM was given. Under the irradiation source, the variation in absorbance values with time was measured. In the absence of catalyst, mere oxidation of H_2O_2 to the drug solution caused the degradation appreciably only after 8h of the reaction. The degradation commenced instantly upon addition catalyst. During the start of the reaction, the mixture containing drug, with oxidant / reductant and the catalyst with irradiation show sharp changes in spectra. However, the changed spectra are retained until the completion of reaction. In Fig.6, the UV-Vis spectra of Lasix during the oxidative degradation by pure ZnO nanoparticles under solar irradiations stacked with respect to time has been shown and tabulated in table 2. The changes in the absorbance values at fixed λ_{max} of 325nm are taken and the absorbance versus time plots are prepared. The change in the absorbance values with respect to time are noted and used for the kinetic results.

Rate Coefficient Measurements: In Fig.7, the decrease in the absorbance values with time of progress of reaction is plotted under the oxidation stress for Lasix. All the three

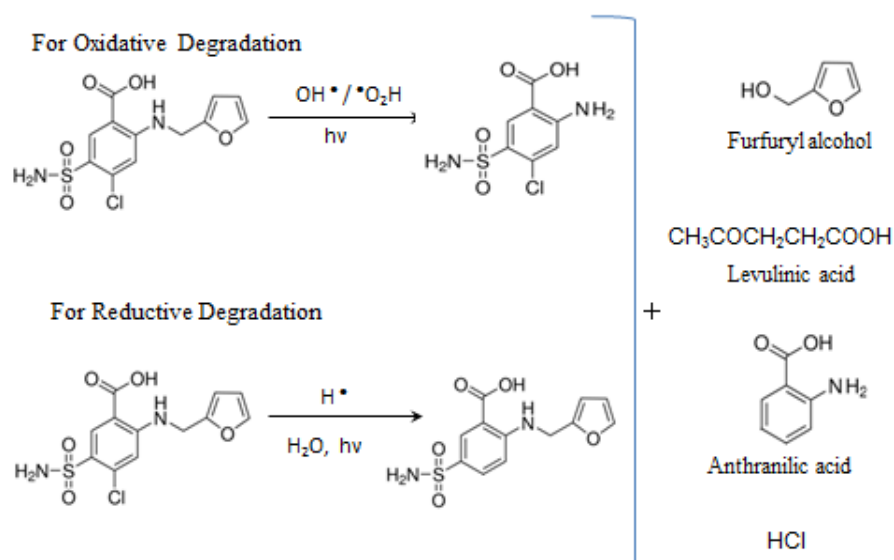
synthesised nano catalysts have been used. The absorbance versus time plot for the solar assisted oxidative degradation of drug by the catalyst (Fig.7) shows there is a gradual decrease in the absorbance value. Since, pseudo first order reaction conditions were maintained, the first order plots for the rate coefficient values are given in the figure 8. The linear plots have confirmed the reaction followed via pseudo first order conditions and the slopes of the linear plots for the rate constant determination.

Replacing the solar irradiations by UV irradiations, the kinetic plots are made adopting similar measurement. The absorbance versus time plot and kinetic plot are given for the UV irradiation assisted oxidative reactions in Fig. 9 and 10 respectively. In table 3, the overall pseudo 1st order rate constant values for both types of irradiations assisted oxidative degradation of the drug Lasix utilising undoped and various doped ZnO nano catalyst are given. Based on the rate constant values, the following trend set in the activity of the oxidative degradation of drugs can be envisaged. It is found that solar irradiations assisted degradation are faster than UV irradiations $K_{\text{Solar}} > K_{\text{UVA}}$. The values indicate that the degradation in solar is nearly three times faster than that in UV irradiations. The higher rate constant values obtained in the degradation by the doped nanoparticles from table 3, infer that the doped nanoparticles have higher photocatalytic activity than the undoped pure ZnO nanoparticles in degrading furosemide. Among the doped nanoparticles, SiO₂ doped ZnO nanoparticles possess higher rate coefficient values and the trend in photocatalytic activity follows the order of SiO₂ doped > SeO₂ doped > undoped ZnO nanoparticles.

However in the case of reduction using NaBH₄, the trend observed is undoped ZnO have higher photocatalytic rate coefficient values than that of dopants and the order is reversed (table 4). The altered trend between the oxidation and reduction stresses on Lasix may be due to the activity of p-block elements towards the peroxide radicals. In the case of reduction reactions, the nascent hydrogen utilised from NaBH₄ is quickly adsorbed on to the ZnO nanoparticles than the doped surfaces. Therefore, such a remarkable change in the dopant effect under the different redox stresses in the catalysis has been observed. It has been well proved in the literature intrinsic dopants have significantly altered the photocatalytic properties of metal oxide nanoparticles^{26, 27}.

Reaction Pathway: Furosemide is a potential diuretic pharmaceutical and susceptible to acid attacks due to secondary amine group presence. In order to rationalise the reaction pathway of the degradation of furosemide drug, the one pot bulk degradation of furosemide in

presence of ZnO catalyst for both oxidation and reduction reaction were performed separately. After the completion of the reaction for 2 hours, the catalyst removed product solutions were subjected to column chromatographic separation of degradation product. The major two separated products were analysed by GC-MS. Here also, during the scaling up of the reaction, photo irradiations were adopted. Both solar and UV irradiations were performed. It was found that the final products were nearly identical. In the oxidation mode, the hydrolysed product by H₂O₂ confirmed with CSA (4-chloro, 5- sulphamoyl anthranilic acid) structure. The GC-MS of the products are given in Fig. 11. Also, the product solutions do not show any traces of unreacted furosemide. In the case of reduction reactions, the GC-MS of the major product supported the evidence of FSA (Furfuryl Sulphamoyl anthranilic acid). Minor quantities of furfuryl alcohol, levulinic acid and anthranilic acid altogether < 2% were detected. In the oxidation mode, methyl group attached to furan group was bifurcated while in reduction mode, dechlorination occurs²⁸⁻³¹. The catalysis by ZnO nanoparticles is brought about in the enhanced production of electron hole pair during irradiation which in presence of H₂O₂ produced hydroxyl radicals and hydroperoxy radicals in sufficient extents. In the case of reduction mode, dechlorination is a possible route of degradation due to H[•] radicals readily forming HCl. The dehydrochlorination product is most prevalent. The plausible schematic routes are presented below.



Plausible schematic routes for degradation of furosemide into fragments

Conclusions:

Nanoparticles of ZnO under doped and undoped conditions are employed as catalyst to bring about the oxidative and reductive degradations of furosemide. Irradiation sources

such as solar and UV are profusely used. Based on the rate coefficient values, the trend set observed is solar irradiations produced higher extent of degradation of furosemide drug Lasix than UV irradiations. In case of ZnO system, incorporation of dopants have altered both the morphology and as well as photocatalytic activity of nano ZnO particles. The increase in bandgap energy and decrease in crystal sizes show the dopant effects in ZnO wurtzite crystals. These observations go in hand that the catalyst involved with higher efficiency in the oxidation reaction exhibited lower efficiency in the reduction reaction conditions.

Acknowledgement:

The PXRD and GC-MS studies were supported by Dr.Sugirdha, Central-XRD and Professor Dr.G.Sekhar, Department of Chemistry, IIT Madras respectively.

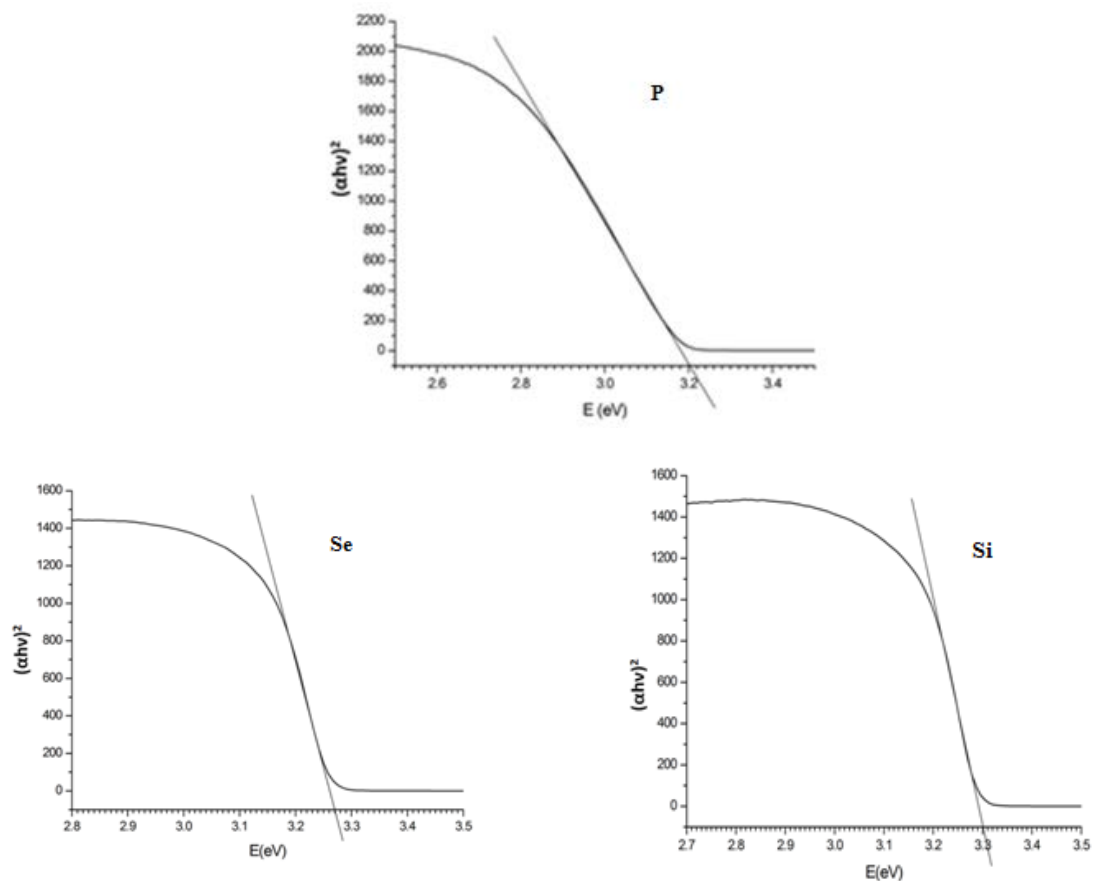


Fig 1: UVDRS plots of undoped ZnO (P), SeO₂ doped (Se) and SiO₂ doped ZnO nanoparticles (Si) respectively.

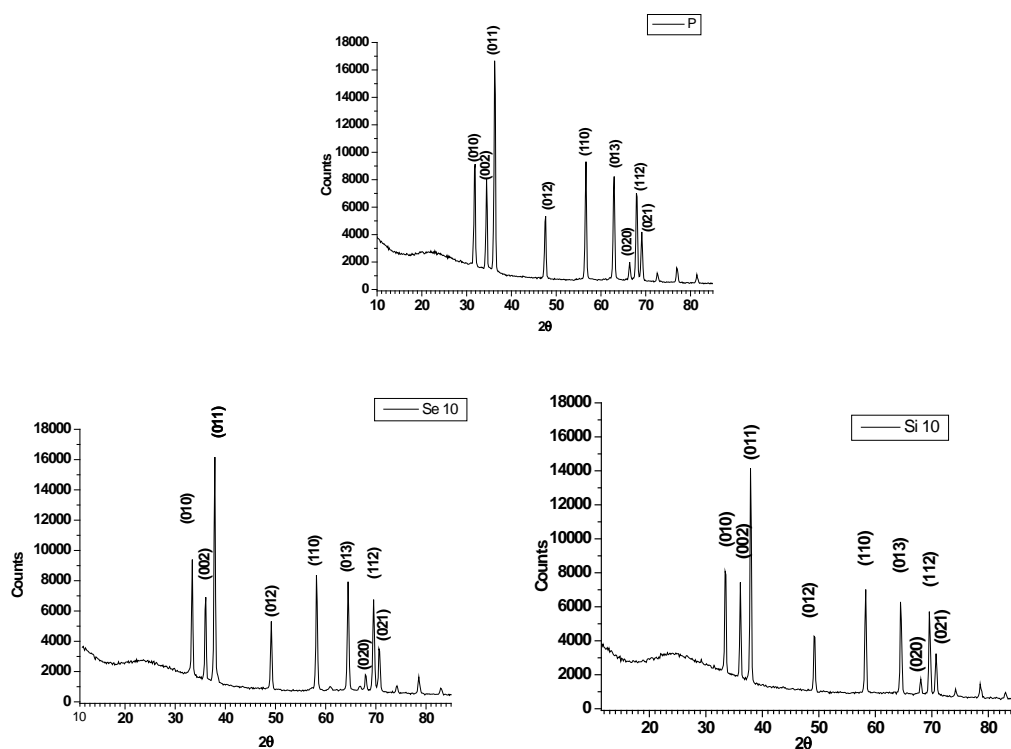


Figure 2: PXRD of undoped ZnO (P), SeO₂ doped (Se 10) and SiO₂ (Si 10) doped ZnO nano particles respectively

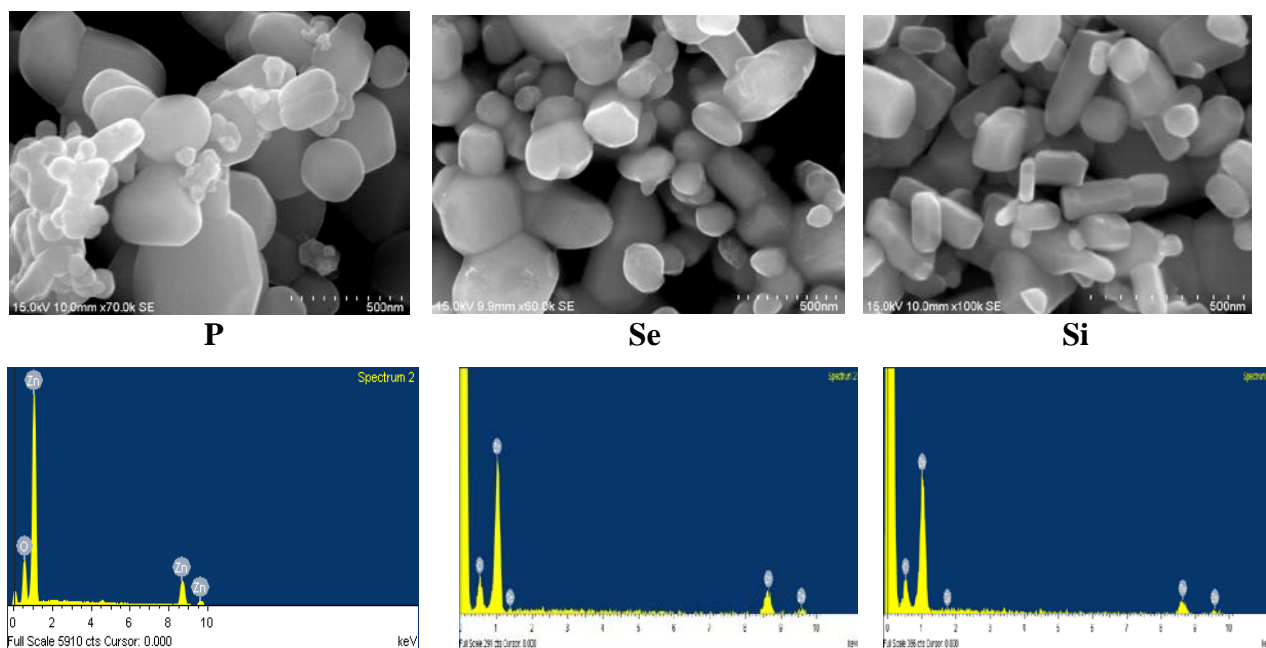


Figure 3: FESEM images and EDAX images of undoped ZnO (P), SeO₂ doped (Se) and SiO₂ (Si) doped ZnO nanoparticles respectively

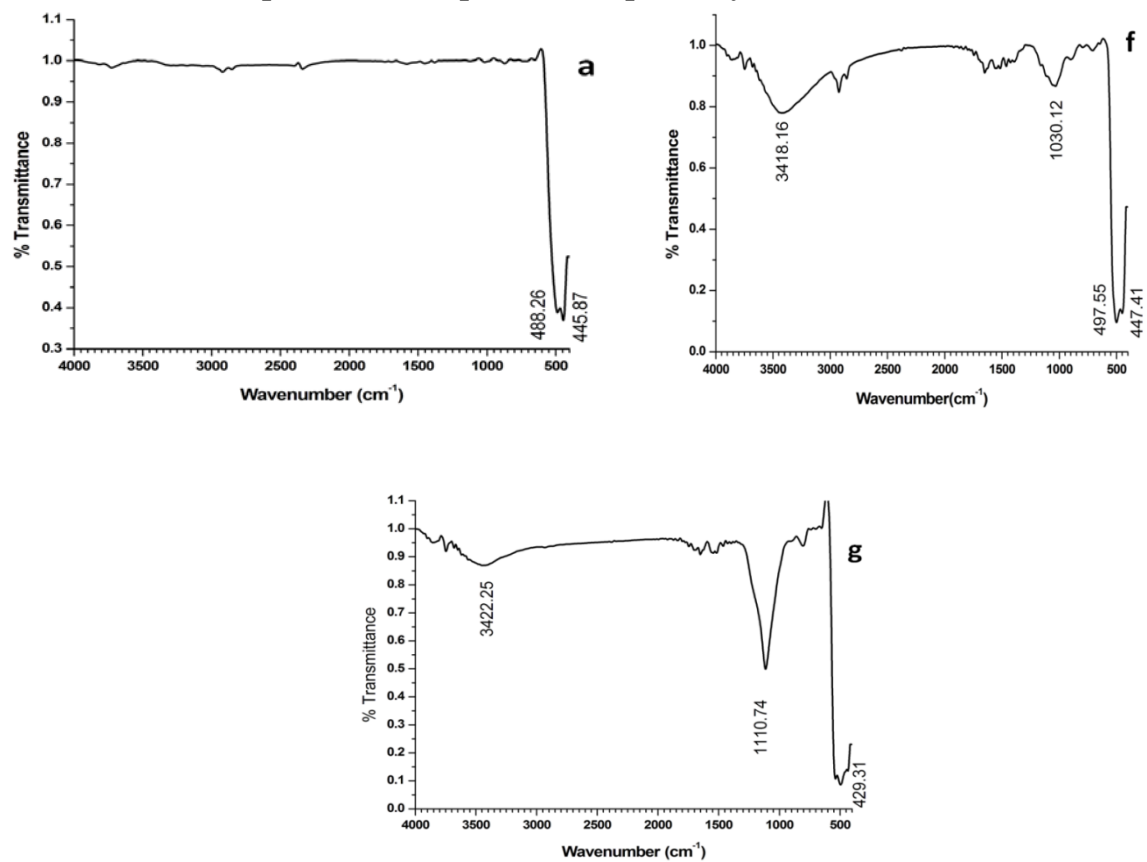


Figure 4: FTIR spectrum of undoped ZnO (a), SeO₂ (f) doped and SiO₂ (g) doped ZnO nanoparticles respectively.

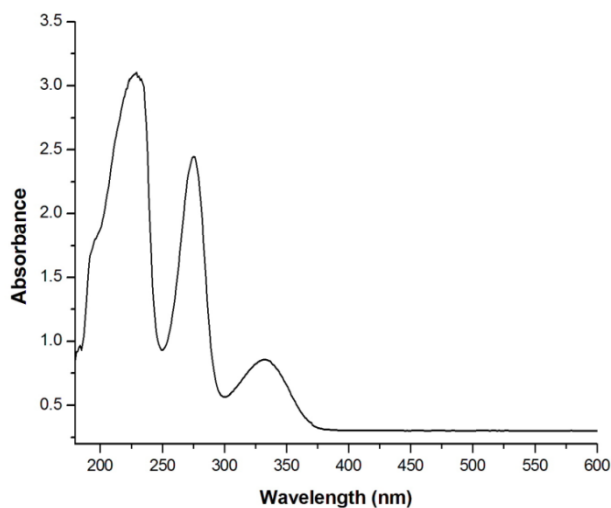


Fig 5: Typical UV-VIS spectrum of Lasix (Furosemide) drug

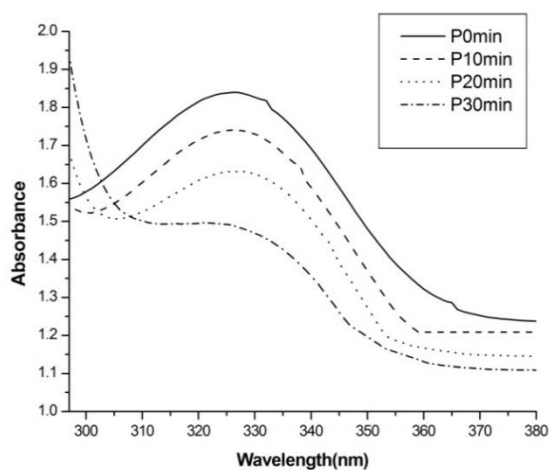


Fig 6: UV-VIS stacked spectra of Lasix degradation

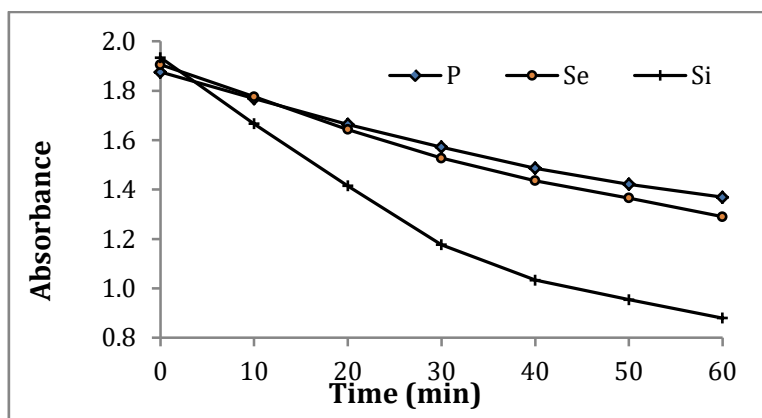


Fig 7: Absorbance versus time plot for solar assisted oxidative degradation of Lasix by catalysts P: ZnO; Se: SeO₂ and Si: SiO₂ doped ZnO respectively.

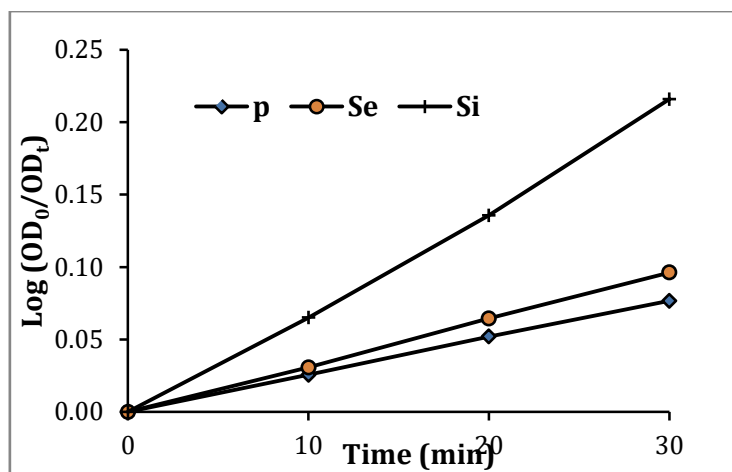


Fig 8: Pseudo first order kinetic plots for solar assisted oxidative degradation on Lasix by P: ZnO; Se: SeO₂ and Si: SiO₂ doped ZnO respectively

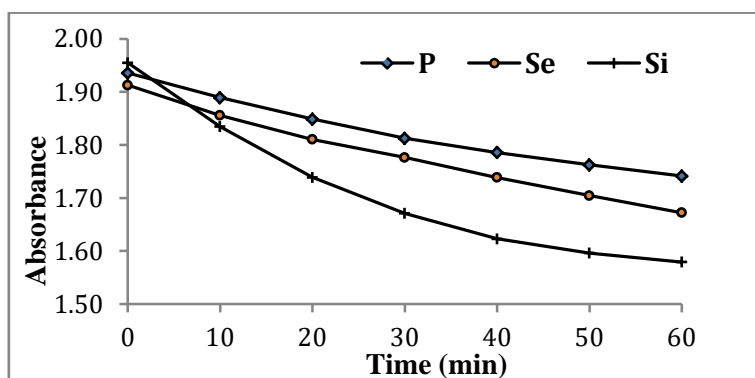


Fig 9: Absorbance versus time plot for UV assisted oxidative degradation by catalysts P: ZnO; Se: SeO₂ and Si: SiO₂ doped ZnO respectively.

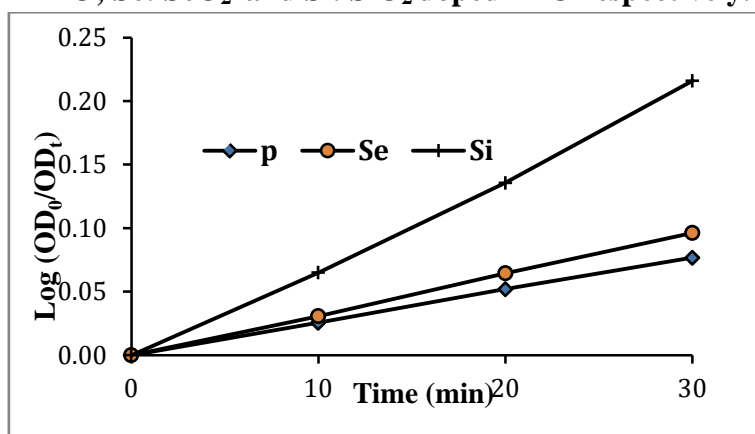


Fig 10: Pseudo first order kinetic plots for UV Assisted oxidative degradation by catalysts P: undoped ZnO; Se: SeO₂ and Si: SiO₂ doped ZnO respectively.

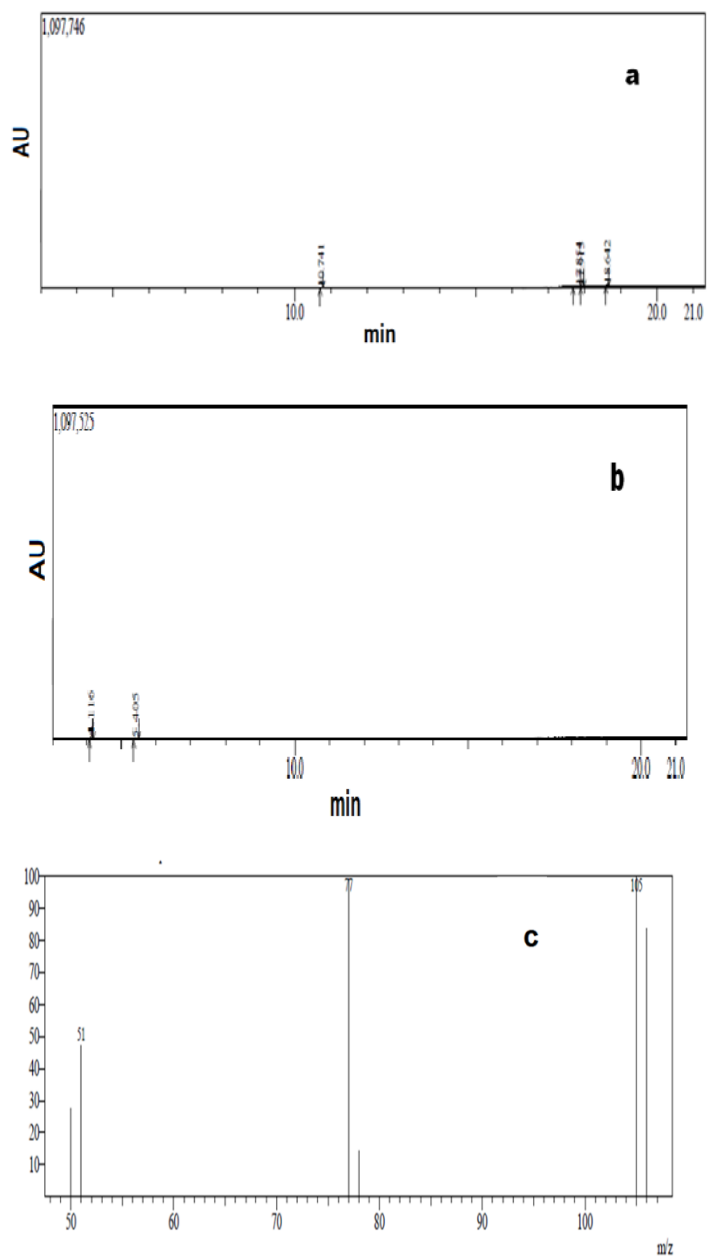


Fig 11: (a) GC pattern of Lasix (b) GC pattern of degraded Lasix (c) Mass spectra of degraded Lasix

Table 1: Band gap energy and Crystal size measurements for pure ZnO nanoparticles and doped ZnO nanoparticles.

Catalyst	Band gap energy values (eV)	Crystallite size from PXRD measurements (nm)
ZnO	3.20	30.0
SeO ₂ -ZnO	3.27	22.0
SiO ₂ -ZnO	3.3	17.0

Table 2: Comparison of Absorbance variation with time of Lasix (furosemide) under Oxidative degradation in solar irradiation

Catalyst	Time (min)	0	10	20	30	40	50	60
P	OD values	1.8754	1.7682	1.6639	1.572	1.4862	1.4215	1.3689
Se		1.9056	1.7756	1.6428	1.5269	1.4357	1.3659	1.2896
Si		1.934	1.6662	1.415	1.1764	1.0335	0.9541	0.8796

Table 3: Pseudo first order rate constant values ($\times 10^{-4} \text{s}^{-1}$) for photo catalytic oxidative degradation of Lasix by the nano catalysts

Irradiations	ZnO	SeO ₂ dopant	SiO ₂ dopant
Solar	1.97	2.48	5.51
UV	0.73	0.84	1.73

Table 4: Pseudo first order rate constant values ($\times 10^{-4} \text{s}^{-1}$) for solar assisted reductive degradation of Lasix catalysed by nanoparticles

Drug	ZnO	SeO ₂ dopant	SiO ₂ dopant
Lasix (Furosemide)	4.62	2.44	2.25

References:

1. K. Samal, S. Mahapatra, Md H.Ali, Energy Nexus, 6, 100076, 2022.
2. A.N. Pestryakov, ACS, 222, U322-U322, 2022.
3. B. Bethi, CEP:PI, 109, 178, 2016.
4. D. Astruc, F. Lu and J. Ruiz Aranzaes, Angew.Chem.Int.Ed., 44, 7852, 2005.
5. N. S. Parmar and K. G. Lynn, Appl. Phys. Lett., 106. 022101, 2015.
6. Y. Yu *J. Phys. Chem. C*, 118 (24), 12727, 2014.
7. A. Catellani and A. Calzolari, Materials, 10(4), 332, 2017.
8. A. R. Puigdollers, F. Illas, and G. Pacchioni, *J. Phys. Chem. C*, 20 (8), 4392, 2016.
9. M. Louhich, S. Romdhane, A. Fkiri, L. Smiri, H. Bouchriha, Applied Surface Science, 356, 998, 2015.
10. A. Majid, F. Javed, S. Akhtar, U. Saleem, F. Anwar, B. Ahmad, A. Nadhman, G. Shahnaz, I. Hussain, S.Z. Hussain and M.F. Sohail, *J. Mater. Chem. B*, 8, 8444, 2020.

11. A.S. Rini, Y. Rati, M. Agustin, Y. Hamzah and A. A. Umar, *Sains Malaysiana* 49(12), 3055, 2020.
12. A. Kuc, *Chemical Modelling*, RSC, 11, 1, 2014.
13. H. R. Pant, *Ceram. Int.* 38, 2943, 2012.
14. P. Coudray, Y. Moreau, P. Etienne and J. Porque, *Proc. SPIE* 10290, *Sol-Gel and Polymer Photonic Devices: A Critical Review*, 102900C, USA, 237, July, 1997.
15. C. Brunelli, C. Bicchi, A. D. Stilo, A. Salomone and M. Vincenti, *J. Sep. Sci.*, 29, 2765, 2006.
16. M. Balouiri, M. Sadiki and S. K. Ibsouda, *J. Pharm. Anal.*, 6 (2), 71, 2016.
17. N.B. Saleh, D.J. Milliron, N. Aich, L.E. Katz, H.M. Liljestrand and M. J.Kirisits, *Science of the Total Environment*, 568, 926, 2016.
18. C.Mao, L.Fang, H. Zhang, W. Li, F. Wu, G. Qin, H. Ruan and C. Kong, *J. Alloys Compd.*, 676, 135, 2016.
19. S.Talukdar and R. K. Dutta, *RSC Adv.*, 6, 928, 2016.
20. S. Kumar, P. Chauhan and V. Kundu, *J. Mater. Sci.: Mater. Electron*, 27(3), 3103, 2016.
21. L. Wang, S. Zheng and H. Chen, *J. Electron. Mater.*, 46, 5, 2017.
22. M.Samadi, M. Zirak, A Naseri, E. Khorashadizade and A. Z. Moshfegh, *Thin Solid Films*, 605, 2, 2016.
23. T. Ruf, S. Repp, J. Urban, R. Thomann and E. Erdem, *Journal of Nanoparticle Research* 18, 1, 2016.
24. K.S. Babu, A.R. Reddy, C. Sujatha, K.V. Reddy and A.N. Mallika, *J. Adv. Ceram.*, 2 (3), 260, 2013.
25. A.Vanaja, G. V. Ramaraju and K. Srinivasa Rao, *Indian J Sci Technol.*, 9 (12), 1, 2016.
26. S. Ananda, *Am. Chem. Sci. J.*, 4 (5), 616, 2014.
27. I. Khan, S. Khan, R. Nongjai, H. Ahmed and W. Khan, *Optical Materials*, 35 (6), 1189, 2013.
28. I.L.T. Dias, J. L.S. Martins and G.O. Neto, *Anal. Lett.*, 38,1159, 2005.
29. S Katsura, N. Yamada, A. Nakashima, S. Shiraishi, T. Furuishi and H. Ueda, *Chem. Pharm. Bull.* 63, 617, 2015.
30. S.C. Broch, J.E. Romero and M.C.G.A. Coque, *J. Pharm. Biomed. Anal.*, 23, 803, 2000.
31. X. Pang, C. Chen, H. Ji, Y. Che and W. Ma, *Molecules*, 19, 16291, 2014.

Chitosan-based Biogenic Nanoparticles for Wastewater Remediation: Synthesis, Characterization, and Applications - A Review[#]

Usman Lawal Usman^{1*}, S. Ellumalai², Anandh, S³ and Venkatesan Madha Suresh⁴

¹Department of Biology, Umaru Musa Yar'adua University Katsina, Nigeria

²Department of Biotechnology and The Registrar, University of Madras, Chennai India

³Centre for Environmental Sciences, University of Madras, Chennai India

⁴Department of Civil Engineering, SRM University, Chennai India

*Email: usman.usman@umyu.edu.ng

Received: 20.9.2023, Revised: 2.11.2023, 26.1.24, Accepted: 27.1.24

Abstract

Wastewater pollution has been a global concern, necessitating the development of efficient and sustainable treatment technologies. Biogenic nanoparticles have emerged as a potential solution owing to their low cost, eco-friendliness, and high remediation efficiency. Among these nanoparticles, chitosan-based nanoparticles have gained significant attention for the treatment of wastewater. Chitosan, a biodegradable polysaccharide derived from chitin, possesses unique physicochemical properties that make it a suitable candidate for nanoparticle synthesis. The present review focuses on the synthesis, characterization, and applications of chitosan-based biogenic nanoparticles for wastewater remediation. Various synthesis methods, such as chemical cross-linking, precipitation, biosynthesis, solvent evaporation, and emulsion techniques are discussed. The characterization of chitosan nanoparticles using techniques such as transmission electron microscopy (TEM), scanning electron microscopy (SEM), X-ray diffraction (XRD), and, Fourier-transform infrared spectroscopy (FTIR) among others were also highlighted to provide insights into their structural and chemical properties. Additionally, the applications of chitosan-based nanoparticles in wastewater remediation, including the adsorption of heavy metals, organic dyes, and pharmaceuticals, are discussed. Finally, the review concludes with a discussion of the prospects and potential research directions in employing chitosan-based nanoparticles for wastewater remediation.

Keywords: Chitosan, Biogenic Synthesis, Nanoparticles, Wastewater, Remediation, Characterization

Paper presented during 3rd International Conference on Recent Trends in Analytical Chemistry (26-28 June 23) organized by Department of Analytical Chemistry, University of Madras, Chennai and ISAS Tamilnadu Chapter

Introduction

Wastewater pollution has emerged as a pressing global concern, necessitating the development of efficient and sustainable treatment technologies. Rapid industrialization, urbanization, and population growth in recent decades have contributed to the generation of large volumes of wastewater, which often contains a diverse range of contaminants¹. These contaminants can include heavy metals, organic dyes, pharmaceuticals, pathogens, and various other pollutants derived from industrial, domestic, and agricultural activities. The discharge of untreated or inadequately treated wastewater into the environment has severe implications for human health, ecosystem integrity, and overall environmental quality². Contaminants present in wastewater can enter water bodies, leading to the contamination of drinking water sources, rivers, lakes, and oceans. This not only poses a direct threat to aquatic organisms but also has the potential to enter the food chain, affecting human populations. Traditional wastewater treatment techniques, such as physical, chemical, and biological processes, have been widely employed. However, these methods often suffer from drawbacks like high cost, energy intensity, and the generation of large amounts of sludge or secondary pollutants³. Therefore, there is a rising need for alternate and sustainable approaches to address the challenges of wastewater pollution effectively. In recent years, biogenic nanoparticles have emerged as a promising solution for wastewater remediation owing to their low cost, eco-friendliness, and high remediation efficiency. These nanoparticles are derived from natural materials and possess unique properties that make them suitable candidates for pollutant removal. Chitosan-based nanoparticles, in particular, have garnered significant attention in the field of wastewater remediation⁴. Chitosan, a biodegradable polysaccharide derived from chitin, exhibits remarkable physicochemical properties, including high surface area, adsorption capacity, biocompatibility, and antimicrobial activity. These properties make chitosan an ideal material for the synthesis of nanoparticles with tailored characteristics and enhanced performance in wastewater treatment applications. Natural chitosan is known to be insoluble in water, organic solvents, and alkaline media, but soluble in organic acids at pH values below 6. Preparation of different water-soluble chitosan salts is possible by its neutralization with hydrochloric acid, acetic acid, lactic acid, or formic acid⁵. Its solubility in diluted aqueous solutions can be correlated with the conversion of glucosamine units into the soluble form of R-NH³⁺. Experimental data proved that water-insoluble chitosan shows antimicrobial activity in acidic medium, being appropriate for use as a preservative in acidic foods. Economic aspects and cost considerations associated with chitosan-based nanoparticles revolve around raw material costs, manufacturing and

processing expenses, customization for specific applications, regulatory compliance, market demand, and competitive pricing strategies. Balancing these factors is essential for determining the economic viability of chitosan-based nanoparticles in various industries.

This review aims to provide a comprehensive analysis of chitosan-based biogenic nanoparticles for wastewater remediation. We will delve into the synthesis methods used to fabricate these nanoparticles, explore the characterization techniques employed to evaluate their properties and examine their diverse applications in pollutant removal. By understanding the fabrication, characterization, and applications of chitosan-based biogenic nanoparticles, researchers can harness their potential to develop efficient and sustainable technologies for wastewater treatment. By bridging the gap between research and application, this review seeks to contribute to the advancement of wastewater remediation strategies and promote the synthesis of eco-friendly nanoparticles. Ultimately, the utilization of chitosan-based biogenic nanoparticles has the potential to significantly improve water quality, protect ecosystems, and safeguard public health in the face of the rising challenge of wastewater pollution.

Chitosan

Chitosan is a natural biopolymer that is made up of a linear polysaccharide that contains a primary amino group and it's considered a derivative of chitin. Chitin is considered one of the most ubiquitous natural biopolymers which form an integral part of the crustaceans. Similar to that cellulose chitin is a polysaccharide, strong, inelastic, and whitish with a replaced acetamide group at their carbon-2 position from the hydroxyl group⁶. The process of deacetylation of the chitin marks the production of the novel chitosan biopolymer.

Sources of the Biopolymer – Chitosan

The enormous chitin distribution is majorly found among crustacean shells such as lobsters, shrimps, and crabs. Similarly, they are also found in the exoskeleton structure of some marine species such as squid pens, jellyfish, and corals (Fig. 1). In addition, some microbes such as the yeast species and other fungi are known to possess chitin on their cell wall. The crustacean shells are made up of about 15 to 40% chitin, and 20 to 40% protein while calcium carbonate (CaCO_3) and magnesium carbonate (MgCO_3) compose of 20 to 50%, and other trace amounts of minerals, astaxanthin, and lipids⁷. Thus, chitosan derived from the shells of crustaceans has a high amount of molecular weight hence resulting in the removal of a large quantity of waste materials from the shells⁸. Crab shells are also a source of chitosan, they are

considered to have carotenoids which provide colouration for the shells⁹. The majority of the available chitosan (α -form) that is commercially synthesized is extracted from crab shells. Recently, chitosan of nanoparticle size has been extracted via encapsulation techniques from the shells of crabs¹⁰. The shells of shrimps are considered the second most common source of chitosan among crustaceans. Various shrimp species are well distributed across the entire world which increases their commercial production. A large number of shrimp heads and skin are generated as biological waste materials with less cost value. However, great value is obtained from this biowaste through the extraction of chitosan. The shells of lobster are known for their large and commercially scale chitosan synthesis. One of the most imperative merits of chitosan extraction from lobster shells is that the chitin steps during the extraction process can be removed¹¹. This helps to reduce the lengthy procedure thereby making the synthesis feasible and time efficient. The shells of the mussel are commonly found along the river banks which differs from that of crustaceans that are only found in the sea. The calcium carbonate content in the shells of the mussels is considered to be higher compared to that of other crustaceans like crabs and shrimps and is slightly less in the cuticles of the oyster¹². The chitin synthesis from the shells of the mussels loses much content moisture during the deacetylation stage of the chitosan extraction.

Significance of Chitosan Nanoparticles

The main constituents of the exoskeletons of terrestrial insects like honeybees and silkworms, as well as the cell walls of moulds, yeast, and ray fungus like *Streptomyces*, are chitin and chitosan. Crustacean shells include those of prawns, squid, crab, and lobster. Chitin can be fully or partially deacetylated to yield chitosan, a cationic biopolymer. Deacetylation of N-acetyl-D-glucosamine yields (1–4)-linked 2-amino-2-deoxy- β -D-glucopyranose, which forms a linear polysaccharide¹³. Because of their degree of deacetylation, polymerization, molecular mass, viscosity, and acid dissociation constant, or pka, chitosan refers to a collection of co-polymers rather than a single substance¹⁴. The chitosan obtained from microbial sources is seen to be promising since the underlying method may be adjusted to produce a clean, consistent product with the required unique properties¹⁵. It is a very adaptable biopolymer with a wide range of applications in the fields of sewage treatment, cosmetics, agriculture, medicine, and food industry¹⁶. Because of its distinct polymeric cationic character, capacity to enhance absorption, mucoadhesive properties, biocompatibility, and biodegradability, Chitosan nanoparticles are utilised extensively. Chitosan is an important biopolymer for the creation of nanoparticles because it is a modified

linear polysaccharide with variable amounts of free amino groups in its polymeric chain and cationic characteristic. This allows it to provide ionic cross-linking of multivalent anions¹⁷. In vivo, the positively charged Chitosan nanoparticles target particular sites with greater affinity for the negatively charged cellular membrane. When chitosan is applied to soil or foliage, it can cause the plant to produce phytoalexins, antifungal hydrolases, or lignin-like substances, which can induce structural barriers and help the plant fend off insect and disease attack¹⁸. Furthermore, the plant's biophysical characteristics are greatly improved by Chitosan nanoparticles. When nano-chitosan is applied, it accelerates photosynthesis, causes root nodulation, increases nutrient absorption, speeds up seed germination, and increases plant vigour¹⁸.

Furthermore, chitosan enhances the gradual release of the medication with improved solubility, it is frequently utilised in the administration of insecticides, fertilisers, and micronutrients¹⁴. Similarly, because it forms a complex by electrostatic contact and shields the nucleic acid from nuclease destruction, chitosan-mediated genetic transformation is also effective. In comparison to plants developed using conventional gene delivery techniques, chitosan-mediated results in plants that are stable transformed¹⁹.

Chitosan Extraction methods

The chitosan extraction from the organism's sources involves a unique successive technique. The general procedure comprised demineralization, deproteinization, decolourization, and deacetylation²⁰.

Demineralization

The process that involves the reduction of the minerals present in a substance is known as demineralization. This is commonly achieved via the treatment of the exoskeleton or shells of some organisms e.g., shrimps, lobster, fungi, etc. with a hydrochloric acid (HCl) solution. The acid concentration controls the demineralization process and it differs according to the content of minerals present in the different sources of materials used for the extraction process. Hydrochloric acid and lactic acids are the major acids used in the process of demineralization of crab and shrimp shells. However, the biological techniques used for the demineralization of the shells involve the use of Lactobacillales (lactic acid bacteria) for treating the shell extract²¹. In the demineralization process, chitosan with less viscosity is synthesized when using a high concentration of acid during the extraction. However, the synthesized chitosan's solubility is neither influenced by the acid type nor the concentration of the acid used during the demineralization process²².

Deproteinization

Deproteinization is the process of treating the shells with a strong solution of alkali for a longer time, which is followed by the dropping of the pH solution to the neutral range. This procedure can be carried out before or after demineralization. In this stage, the protein is removed from the shells alongside the ones that are bound with chitin due to the recurrent pH change. The repeated deproteinization procedure will result in a better chitin yield which will give rise to the chitosan from the animal shells. Similarly, following the deproteinization process, the amount of amino acid that is acidic will be greater compared to that of the alkaline amino acid²³.

Decolourization

The decolourization process is generally carried out among marine chitosan sources. This is conducted to remove the excess pigment found on the shells of marine crustaceans. The short period of the shells making contact with the weak acid solution results in the removal of the colour or bleaching of the shells²⁴. Thus, before the decolouration process, the extracted chitin usually has a slightly pink colour.

Deacetylation

The elimination of the acetyl group from the extracted chitin to give rise to chitosan is a term for the deacetylation process. This is considered the major step that involves the chitosan production process. The amount of deacetylation of the chitin determines the physical characteristics and chemical properties alongside the quality of the synthesized chitosan. The deacetylation techniques comprise long chitin treatment using a strong concentrated solution of alkaline. Continual deacetylation under heat helps in the synthesis of chitosan which has a higher rate of solubility and a degree of deacetylation (DDA). The deacetylated chitin that ascribes to the hydroxyl and amine groups tends to make the extracted chitosan more reactive compared to the chitin²⁵.

Types of Biopolymer Chitosan

Chitosan is majorly categorized into three forms according to their structural orientation, these are alpha (α), beta (β), and gamma (γ) chitosan. Most of the chitosan that is commercially produced are alpha (α) types which are extracted from the crustacean's shells. While the beta (β) type which is mostly reactive is extracted from the pens of squid. Generally, all three (α , β , and γ) forms of chitosan are soluble in acid. In addition, the alpha type of chitosan demonstrates a greater bactericidal effect as compared to the beta and gamma types²⁶. Table 1. depicts different properties among the various types of Chitosan.

Chitosan Properties and Chemical Structure

Chitosan is a natural polysaccharide substance composed of a glucosamine copolymer that is partly deacetylated polymer is derived via the process of deacetylation of chitin using an alkaline solution, for example, a biopolymer that is extracted from shell-fish. The chitosan structure is composed of a rigid material containing a unit of glucosamine substance and acetyl glucosamine polymer β : -1-4, 2-amino-2-deoxy-D-glucose with a structure of linear hydrophilic amino-polysaccharide groups as shown in Fig. 2. Natural chitosan tends to become insoluble in water or organic solvent, however, after protonating the free amino group and the pH range is decreased to below 5 scales, the chitosan now becomes soluble and possesses a high-density charge of positive polymers²⁷. Nevertheless, the protonated polymer having positive charges can be able to effectively flocculate and neutralize the negatively charged particles that are suspended in the form of colloidal materials. Thus, reducing the concentration of chlorides, turbidity, and chemical oxygen demand in the contaminated water²⁸.

Synthesis Methods for Chitosan-based Nanoparticles

Several specific techniques are employed for the fabrication of chitosan-based biogenic nanoparticles, each offering distinct advantages in terms of control over nanoparticle properties and scalability. Because they are more stable and have a higher adsorption capacity and better transport capability, chitosan nanoparticles enhance the benefits of chitosan²⁹. The past several decades has seen the use of a variety of techniques, including ionic gelation, microemulsions, emulsification, cross-linking, and polymerization, to generate chitosan nanoparticles. The chitosan particle size and molecular structure produced by this approach vary depending on some changes in the procedure. 300 nm to 500 nm is typically the range of findings from such procedures²⁹. The synthesis of nanoparticles via biogenesis is favoured over chemical or physical methods because it is a less time-consuming, safe, environmentally benign, economically and energetically feasible process that maximises the redox potential of metabolites produced by biological entities to transform macromolecules into nano form³⁰. Below are some of the commonly used techniques for nanoparticle fabrication:

i. *Chemical cross-linking method*: The chemical cross-linking method involves the cross-linking of chitosan molecules using cross-linking agents such as tripolyphosphate (TPP), sodium sulfate (Na_2SO_4), glutaraldehyde, citric acid, genipin, ethylenediamine (EDA), etc. Chitosan and the cross-linking agent are mixed, and the reaction leads to the formation of a three-dimensional network, resulting in nanoparticle formation. One commonly used cross-

linking agent for chitosan is tripolyphosphate (TPP). When chitosan and TPP are mixed, the interaction between chitosan amino groups and TPP phosphate ions forms strong ionic bonds, resulting in the formation of a three-dimensional network structure. This network traps the chitosan molecules and stabilizes them in a nanoparticle configuration. Sodium sulfate is another agent used similarly for cross-linking chitosan, leading to the creation of chitosan nanoparticles³¹. Glutaraldehyde is a cross-linking agent that forms covalent bonds with chitosan molecules, producing more stable and rigid nanoparticles. It can be utilized to tailor the mechanical properties and biodegradability of chitosan-based nanoparticles. Citric acid, genipin, and EDA are other cross-linking agents employed for chitosan modification, each offering unique advantages and characteristics for different applications. The size and properties of the chitosan nanoparticles can be adjusted by varying several factors, including the concentration of chitosan, the type and concentration of the cross-linking agent, and the reaction time. A higher concentration of chitosan typically results in larger nanoparticles, while increasing the cross-linking agent concentration or extending the reaction time can lead to smaller nanoparticles with enhanced stability³².

ii. *Biosynthesis using microorganisms*: Biosynthesis involves the use of microorganisms, like bacteria or fungi, as living factories for the production of chitosan-based nanoparticles. The redox processes that take place when a biological entity or microbe absorbs a metal ion and converts it to an element metal through cellular enzymatic activity form the fundamental basis for the biogenic creation of nanoparticles. Both external and intracellular synthesis fall under this category. The process of intracellular synthesis involves the transportation of metal ions into the cell, thereafter the reduction reaction takes place within the cell wall, cytoplasm, or periplasmic space. As a result, the resulting nanoparticles are formed inside the cell. But in the second case, the foreign object that has been trapped causes the reductase enzyme to catalyse the creation of nanoparticles on the cell surface³³. Extracellular synthesis of nanoparticles is often preferred over intracellular production due to the laborious procedure of harvesting nanoparticles from the cell matrix. Because of their capacity to produce nanoparticles on a vast scale, with relative control over their size and form (controlled by surrounding environmental conditions) and a simplified process of manufacturing, microorganisms are sometimes described as environmentally benign green nano-factories³⁰. Typically, a magnetic stirrer is used to constantly mix the plant component extract after the metal ions are injected during the phytofabrication of nanoparticles. When the resulting solution changes colour, the creation of nanoparticles may be visually verified³⁴. The metal ion is affected by antioxidants like polyphenols, flavonoids, and phytoalexins, which change

it into a harmless element metal in nanoform. Therefore, for the phytofabrication of nanoparticles, a plant with a larger percentage of naturally reducing elements is preferred. El-Naggar et al.¹³ combined an equivalent amount of *P. graveolens* phytoextract with chitosan solution, then incubated the combination in a rotating shaker at 50°C. After that, the turbid solution that remains after the redox reaction is created is centrifuged for 10 minutes at 10,000 × g. To get rid of the unreacted chitosan, it was further cleaned with an acetic acid solution. The Chitosan nanoparticles in the solution were then extracted by freezing and drying it. Similarly, fungal sources rich in chitosan were used to biogenically synthesise Chitosan nanoparticles by Boruah and Dutta¹⁸. The fungal biomass was subjected to a series of controlled alkali and acid treatments to isolate the chitosan. After first treating the fungal biomass with NaOH, an alkali-insoluble material (AIM) was produced. To extract the fungal chitosan, this AIM was next treated with an acid. Next, it was mixed with 1% TPP solution in a magnetic stirrer to create nano-chitosan.

iii. *Enzymatic synthesis*: Enzymatic synthesis utilizes enzymes, such as lysozyme or chitinase, to degrade chitosan into nanoparticles. Enzymes break down the chitosan polymer chains, resulting in the formation of nanoparticles. This method allows for precise control over the size and morphology of the nanoparticles by adjusting the enzyme concentration, reaction conditions, and chitosan properties. Enzymatic synthesis offers advantages such as mild reaction conditions, high specificity, and the potential for tailoring nanoparticle properties through enzyme engineering. These techniques provide researchers with a range of options for fabricating chitosan-based biogenic nanoparticles with specific properties and characteristics. However, it is important to note that the choice of technique depends on various factors, including the desired nanoparticle size, shape, surface properties, and specific application requirements.

iv. *Precipitation method*: The precipitation method involves the dissolution of chitosan in a suitable solvent, followed by the addition of a precipitating agent. Commonly used precipitating agents include sodium tripolyphosphate and calcium chloride. The addition of the precipitating agent causes chitosan to undergo phase separation and form nanoparticles. The size and morphology of the nanoparticles can be regulated by adjusting the concentration of chitosan, the precipitating agent, and the rate of mixing. This method offers simplicity, scalability, and the ability to produce chitosan-based nanoparticles with a narrow size distribution³⁵.

v. *Emulsion method*: The emulsion method utilizes the emulsification of chitosan in an organic solvent followed by the formation of nanoparticles through solvent evaporation.

Chitosan is dissolved in an organic solvent, and the resulting solution is emulsified in an aqueous phase using surfactants. The organic solvent is then evaporated, resulting in the formation of nanoparticles. The size and morphology of the nanoparticles can be controlled by adjusting the emulsion droplet size, surfactant concentration, and the rate of solvent evaporation. This method allows for the production of chitosan-based nanoparticles with controlled sizes and shapes.

vi. *Solvent evaporation method*: In the solvent evaporation method, chitosan is dissolved in a volatile organic solvent and then added dropwise to an aqueous solution under stirring. The organic solvent rapidly evaporates upon contact with the aqueous solution, leading to the precipitation of chitosan and the formation of nanoparticles. The size and morphology of the nanoparticles can be controlled by adjusting the chitosan concentration, solvent composition, and the rate of solvent addition. This method offers simplicity and scalability for the fabrication of chitosan-based nanoparticles. Gallic acid and chitosan were used in the combination of ultrasonication and chemical reduction methods by Guzman et al.³⁶ to synthesise colloidal AgNps. Upon characterization, they discovered that the resulting gallic acid-chitosan-modified silver nanoparticles (GC-AgNps) were spherical, monodispersed, and stable for four weeks without exhibiting any discernible changes in size. After 120 minutes of exposure, it was discovered that GC-AgNps had great efficacy against *Escherichia coli* even at 1 µg/mL³⁶.

In addition to the aforementioned techniques, other methods can be employed for chitosan-based nanoparticle fabrication. These include electrostatic assembly, template-assisted synthesis, spray drying, and supercritical fluid technology. Electrostatic assembly involves the layer-by-layer deposition of chitosan and oppositely charged polymers or nanoparticles, resulting in the formation of chitosan-based nanoparticles with controlled layer thickness and surface functionality. Template-assisted synthesis utilizes templates or molds to shape chitosan solutions into specific nanoparticle structures, offering precise control over size and shape. Spray drying involves atomizing chitosan solutions into fine droplets, which subsequently dry and form nanoparticles³⁷. Supercritical fluid technology employs supercritical fluids to dissolve chitosan and then rapidly depressurize it to induce nanoparticle formation. Moreover, various modifications and advancements can be incorporated into these techniques to enhance the fabrication process and nanoparticle properties. For instance, the introduction of microfluidic devices enables precise control over reactant flow rates, resulting in uniform nanoparticle size and shape. Ultrasonication can be utilized to aid in the dispersion and homogenization of chitosan solutions, promoting uniform nanoparticle formation.

Furthermore, the integration of green chemistry principles, such as using environmentally friendly solvents and reducing waste generation, contributes to the development of sustainable and eco-friendly nanoparticle fabrication methods. Table 2: depicts some chitosan nanoparticle synthesis techniques alongside their advantages and disadvantages.

Characterization Techniques for Chitosan-based Nanoparticles

Characterization techniques are essential tools for assessing the properties of chitosan-based nanoparticles and evaluating their suitability for various applications, including wastewater remediation. These techniques provide valuable insights into the structural, morphological, surface, and physicochemical properties of the nanoparticles, allowing researchers to understand their behavior, performance, and interactions with pollutants³⁸. Below are various characterization techniques commonly used to assess chitosan-based nanoparticles.

i. Spectroscopic Techniques: Spectroscopic techniques are widely employed to investigate the structural properties of chitosan-based nanoparticles. These techniques provide information about the chemical composition, functional groups, and molecular interactions within the nanoparticles. Some commonly used spectroscopic techniques include:

a) Fourier Transform Infrared Spectroscopy (FTIR): FTIR is a powerful technique for analyzing the functional groups and chemical bonds present in chitosan-based nanoparticles. It measures the absorption of infrared light by the nanoparticles, providing information about their molecular structure, degree of deacetylation, and any modifications or surface functionalization. FTIR provides valuable insights into the interactions between bonds and their respective functions. The fundamental idea behind the FTIR approach is that molecules, whether inorganic or organic, absorb electromagnetic radiation in the infrared range (4000–400 cm^{-1}). When a molecule absorbs infrared light, its dipole moment should alter, making it infrared active. An interference pattern is recorded when the data is measured in terms of wavenumbers, and this data is then transformed into a spectrum (transmittance/absorbance form)³¹. Fig. 3 provides a schematic illustration of the procedures involved in FT-IR analysis²⁰. The type of bonds, functions related to molecular structures, and interactions may all be determined with the aid of the spectrum, which is often represented by separate lines that can be broad or thin and correspond to a certain frequency³¹. Samples can be liquid, solid, or gaseous; however, KBr (100:1) is typically used to make solid or liquid samples, and a hydraulic press machine is used to create the pellet. First, at room temperature, a blank KBr background is recorded on the instrument, and then a KBr pellet containing the samples of

interest let's say chitosan nanomaterial/NPs in an absorbance/transmittance mode is recorded. It is important to note that the FTIR method is a very powerful analytical instrument that has been used to better understand the functions of NPs made of chitosan³⁹.

b) Ultraviolet-Visible Spectroscopy (UV-Vis): UV-Vis spectroscopy is used to determine the optical properties of chitosan-based nanoparticles. It measures the absorption or scattering of UV or visible light by the nanoparticles, providing information about their size, aggregation state, and optical behavior. UV-Vis spectroscopy can be used to assess the stability, dispersion, and surface plasmon resonance of the nanoparticles.

c) X-ray Diffraction (XRD): XRD Chitosan-based nanomaterials/NPs are not simple molecules, like any other nanoparticle system; instead, they are organised into three primary layers. First and foremost is the surface layer, which can be functionalized appropriately by coating with surfactants, encasing metal ions, etc. The third layer, which is effectively the core and is the central/innermost segment of chitosan-based NPs, is chemically separate from the second layer, also known as the middle layer or shell layer. The solid-state characteristics of crystallinity, composition, defect structure, grain size, etc. may all be efficiently used to shed light on the molecular dynamics of chitosan-based nanoparticles, or NPs. One effective method for examining the solid-state characteristics of chitosan-based nanomaterials/NPs is X-ray diffraction (XRD)^{40,41}.

Determining the crystallographic structure of nanoparticles is a crucial step in the field of material research. Max Von Laue made a significant finding in 1912 that the behaviour of a substance's two-dimensional diffraction gratings (also known as nanomaterials or NPs) in the presence of an X-ray wavelength is comparable to that of a crystal lattice's plane spacing. With the use of X-ray diffraction (XRD), a non-destructive analytical method, it is possible to identify the surface or phase of chitosan-based nanomaterials and get data on their cell sizes and atomic spacings. The incoming X-rays from the 1.5418 Å cathode ray "Cu X-ray tube" in XRD are filtered to create monochromatic radiation, which is then collimated to concentrate and utilised to irradiate the sample (a nanomaterial based on chitosan)^{42, 43}. The interaction between the incoming rays and the chitosan-based nanomaterial results in a diffracted ray and constructive interference after meeting Bragg's equation ($n\lambda = 2d \sin\theta$). According to Bragg's equation, the wavelength of an incoming ray (λ) may be correlated with the diffraction angle (θ) and lattice spacing (d) to determine the scattering angle and intensity that are diffracted from the sample⁴². The chitosan-based nanomaterial sample material, whether it is in the form of a powder or a film, has to be homogenised. It is possible to obtain a finite diffraction

direction for the lattice by varying the 2θ (2 theta) angles to all possible points. Every material has a distinct set of d-spacings, and the International Centre for Diffraction Data (ICDD) or, formerly, the Joint Committee on Powder Diffraction Standards JCPDS data, may provide the appropriate places and intensities as a reference pattern or database⁴². Therefore, it is simple to determine the particle size, content, crystalline nature, form of a unit cell, and other characteristics of chitosan-based nanomaterials/NPs by converting diffraction peaks to d-spacings⁴³. Notably, the size, shape, and nature of a unit cell of chitosan-based nanomaterials or NPs determine the direction of the diffraction angle, while the internal structural arrangements of the atoms determine the intensities of the diffraction patterns. The XRD spectra of chitosan powder were successfully reported by Usman et al.²⁰. The spectra showed features peaks corresponding to 2θ values of 10.9° and 19.8° , which correlate to the amorphous structure of chitosan (Fig. 4). The literature is widely aware that chitosan's internal lattice structure configurations are changed by structural alterations. Changes in the structural arrangements of chitosan are caused by several factors, including the degree of deacetylation, molecular weight, drying, precipitation, chemical processing, and dissolving process⁴⁴.

ii. Imaging Techniques: Imaging techniques allow for the visualization and characterization of the morphology, size, and shape of chitosan-based nanoparticles. These techniques provide valuable information about the physical characteristics and surface properties of the nanoparticles. Some commonly used imaging techniques include:

a) Transmission Electron Microscopy (TEM): Transmission electron microscopy, or "TEM," is a widely used technology for characterising chitosan-based nanomaterials because of its better spatial resolution, or equivalency with atomic dimensions. TEM offers chemical information and internal structural arrangements in an image format. A highly charged electron beam is sent through a thin foil in a TEM, changing its shape from elastic to inelastic. These altered electrons subsequently interact with the specimen, which contains a sample of chitosan nanomaterial. Particles that were transmitted or reflected were released as a result of the interactions between the inelastic/elastic electrons and the specimen. Following the detection of the energy difference, the camera produces better-resolution magnified pictures, which are subsequently visualised on a monitor. It is important to note that the ratio of the specimen, image plane, and objective lens-which has to be amplified by the lens- is taken into consideration⁴⁵. In comparison to SEM, TEM offers higher resolution (down to 0.2 nm) and higher-quality analytical measurements. This is because both methods show the

visualisation of nanomaterials, including how they appear, how their atoms are arranged, the degree of aggregation, and details about their size and dimensions. Because TEM uses energetic electrons to infer composition, morphology, imaging, and crystallographic analysis, it may yield comprehensive information. Consequently, TEM employed three primary methods, namely, diffraction pattern, imaging, and electron microscopy. For TEM analysis, sample preparation is rather straightforward: following sonication, a drop or two of a suspension of chitosan-based nanomaterials is added to a carbon-coated copper grid, which is then dried or, in certain cases, exposed to infrared radiation. Additionally, TEM differentiates between chitosan-based nanomaterials/NPs that are polycrystalline, amorphous, and monocrystalline⁴⁰. It is important to note that while there is a possibility of aggregation during the sample preparation procedure, the size distribution or size estimation of nanomaterials using TEM is precise rather than exact. Cryo-TEM is better than traditional TEM analysis because in the former case, a suspension of nanomaterial is solidified at cryogenic temperatures (-100 to -175 °C), and the visualisation is carried out when the specimen is frozen. By avoiding the issues of nanoparticle aggregation, heavy-metal contrasting agents, and solvation, the previously described technique produced a size estimation that was both exact and accurate⁴⁵.

The cryo-TEM is very helpful in determining if the self-assembly of chitosan-based nanomaterials is a natural occurrence or whether it only happens during sample preparation, in which case solvation/evaporation processes come into play⁴⁵. TEM analysis has been used for chitosan-based nanomaterials/NPs in some papers in the literature. By adopting a benzyl alcohol/water emulsion technique, Facchi et al.⁴⁶ effectively reported the synthesis of N-modified chitosan NPs for curcumin administration. TEM investigation further reveals that the average particle size of TMC/TPP NPs is around 99 nm, but it may reach up to 317 nm for DMC/TPP NPs⁴⁶. Using a reverse micellar system comprising surfactant, namely sodium bis (ethylhexyl) sulfosuccinate (AOT) and n-hexane, Banerjee et al.⁴⁷ reported the production of ultrafine chitosan nanoparticles in which the amine groups are cross-linked (10% or 100%)⁴⁷. According to the TEM study, the particles have a spherical shape and aggregate with dimensions of 30 nm when 10% amine functionalization (for chitosan NPs) is cross-linked, but the particle size increases to 110 nm when 100% cross-linking is applied⁴⁷. Several additional studies have reported on the spherical-type morphologies of chitosan-based nanoparticles⁴⁸ and their combination with chitosan to encapsulate metals like Cu⁴⁹.

b) Scanning Electron Microscopy (SEM): SEM is an effective technique for determining surface visualizations, studying functionalized/ agglomerated chitosan nanoparticles (NPs) in

detail, and estimating sample composition by energy-dispersive X-ray spectroscopy (EDX) is scanning electron microscopy (SEM). SEM achieves resolutions in the nanometer range by using an energised electron beam (usually 1–30 eV) to scan the sample's surface in a raster pattern and identify secondary emitted or backscattered electrons. Different types of radiated electrons are produced at or on the surface of the sample depending on the electronic interaction between the sample (chitosan nanoparticles) and the sample. The electrons of various energies that are detected are processed and shown as a pixel on the monitor, allowing the visualisation of three-dimensional pictures or the makeup of nanomaterials. Field emitter scanning electron microscopy (FE-SEM) is the term used when these electrons are beamed under a strong electric field⁵⁰. Traditionally, high vacuum conditions are employed to apply an ultrathin coating of noble metals, such as gold (Au), silver (Ag), and platinum (Pt), to increase the electrical conductivity and contrast of nanomaterials⁵¹. SEM analysis is widely applied in the literature for chitosan-based nanomaterials/NPs to provide a graphical visualisation⁵¹. Poly (lactic acid)/chitosan (PLA/CS) nanoparticles were synthesised by Dev et al. in 2010⁵² by the use of solvent evaporation and emulsion methods. The surface shape of ZnO-Chitosan NPs is depicted in Fig. 5, which displays SEM images of the particles²⁰. Using a two-step procedure of oil-in-water emulsion followed by ionic gelation, Hosseini et al.⁵³ produced the essential oil-encased chitosan NPs⁵³

iii. Surface Analysis Techniques: Surface analysis techniques are employed to evaluate the surface properties, charge, and interactions of chitosan-based nanoparticles. These techniques provide insights into the surface chemistry, charge distribution, and surface energy of the nanoparticles. Some commonly used surface analysis techniques include:

a) Brunauer-Emmett-Teller (BET) Analysis: BET analysis is a technique used to determine the specific surface area and porosity of chitosan-based nanoparticles. It measures the adsorption of gas molecules onto the nanoparticles, providing information about their surface area, pore size distribution, and surface roughness. BET analysis is valuable for assessing the adsorption capacity, surface reactivity, and surface accessibility of the nanoparticles.

b) Zeta Potential Analysis: Zeta potential analysis measures the electrical charge and surface potential of chitosan-based nanoparticles. It provides information about the stability, dispersibility, and potential for aggregation of the nanoparticles. Zeta potential analysis is valuable for understanding the electrostatic interactions between the nanoparticles and pollutants, as well as their colloidal stability in aqueous solutions. By measuring the zeta

potential, researchers can gain insights into the surface charge, surface functionality, and the potential for nanoparticle-pollutant interactions.

iv. Thermal Analysis Techniques: Thermal analysis techniques are used to investigate the thermal stability, decomposition behavior, and thermal properties of chitosan-based nanoparticles. These techniques provide information about the thermal transitions, degradation temperature, and thermal stability of the nanoparticles. Some commonly used thermal analysis techniques include:

a) Thermogravimetric Analysis (TGA): TGA measures the weight changes of chitosan-based nanoparticles as a function of temperature. It provides information about the thermal stability, decomposition kinetics, and thermal degradation behavior of the nanoparticles. TGA analysis can help assess the temperature range at which the nanoparticles maintain their structural integrity and stability.

b) Differential Scanning Calorimetry (DSC): DSC measures the heat flow into or out of chitosan-based nanoparticles as a function of temperature. It provides information about the phase transitions, melting points, glass transitions, and thermal behavior of the nanoparticles. DSC analysis can be used to determine the crystallinity, degree of cross-linking, and thermal stability of the nanoparticles.

v. Particle Size and Size Distribution Analysis: Characterizing the particle size and size distribution of chitosan-based nanoparticles is crucial for understanding their behavior, stability, and performance in wastewater remediation. Several techniques can be employed for particle size analysis, including:

a) Dynamic Light Scattering (DLS): A flexible and effective technique for analysing the diffusion behaviour of molecules in the solution phase is dynamic light scattering (DLS), also known as quasi-elastic light scattering (QELS) or photon correlation spectroscopy (PCS). The DLS or PCS approach determines the hydrodynamic radii or diffusion coefficient, which in turn affects the size distribution, particle size, surface charge, and morphologies of the particles (nanoparticles/macromolecules)⁵⁴. Since the sample to be analysed in DLS often needs to be in the solution phase, the size is determined by observing the Brownian motion of suspended particles with varying scattered angles, or " θ "⁵⁴. The constant bombardment of solvent molecules around suspended particles and molecules causes their random motion. Particles with dimensions less than one nanometer can be measured using the DLS method. The Stoke-Einstein equation was utilised in DLS to determine the NPs' size. Chitosan nanomaterials, or NPs, have hydrodynamic radii " d_h " that may be calculated from particle diffusion (D) using the formula $d_h = kT/3\pi\eta D$, where η represents the medium viscosity, T is

the absolute temperature, and k is the Boltzmann constant⁵⁴. Numerous scientific studies have previously been published in the literature, and they show that the DLS approach is useful in determining surface charge characteristics and size distribution⁵⁵. It is crucial to combine the DLS approach with more complex methods like microscopy to obtain trustworthy results. Reliable and reproducible data may be acquired for completely dispersed chitosan nanoparticles/nanomaterials, eliminating the idea of aggregation. Because chitosan is polymeric in nature and the DLS technique's fundamental theory is based on the Brownian motion of particles, the real size of the particle is always smaller than the average particle that is detected. Using the DLS approach, Li et al.⁵⁶ determined the average particle size distribution of ferrite-coated chitosan NPs, which range in size from 10 to 100 nm⁵⁶

b) Laser Diffraction: Laser diffraction is a technique that measures the scattering pattern of a laser beam passing through a dispersion of chitosan-based nanoparticles. It provides information about the particle size distribution and the volume-based particle size of the nanoparticles. Laser diffraction analysis is valuable for assessing the size range, polydispersity, and agglomeration state of the nanoparticles.

c) Atomic Force Microscopy (AFM): AFM is a high-resolution imaging technique that can be used to determine the size and topographical features of chitosan-based nanoparticles. It provides three-dimensional images and surface profiles of individual nanoparticles. AFM analysis allows for the direct measurement of particle size, height, and surface roughness.

vi. Rheological Analysis: Rheological analysis is used to assess the flow behavior, viscosity, and rheological properties of chitosan-based nanoparticle suspensions or gels. It provides information about the stability, dispersion, and potential for aggregation of the nanoparticles in complex fluids. Rheological measurements can be performed using techniques such as:

a) Rheometry: Rheometry involves the measurement of the flow and deformation of chitosan-based nanoparticle suspensions under controlled shear or stress conditions. It provides information about the viscosity, shear-thinning behavior, viscoelastic properties, and gelation characteristics of the nanoparticle systems. The rheological analysis is crucial for understanding the flow behavior and stability of nanoparticle suspensions in practical applications.

vii. Elemental Analysis: Elemental analysis is used to determine the elemental composition and elemental distribution within chitosan-based nanoparticles. It provides information about the presence of impurities, functional groups, and chemical elements incorporated into the nanoparticles. Some commonly used elemental analysis techniques include:

a) *Energy-dispersive X-ray spectroscopy (EDS)*: EDS is used in conjunction with scanning electron microscopy (SEM) to analyze the elemental composition of chitosan-based nanoparticles. It provides qualitative and quantitative information about the presence of different elements within the nanoparticles.

b) *Inductively Coupled Plasma Mass Spectrometry (ICP-MS)*: ICP-MS is a highly sensitive technique used to measure the elemental composition and trace element concentrations in chitosan-based nanoparticles. It provides quantitative information about the presence of various elements and can detect impurities or contaminants in the nanoparticles. An inductively coupled plasma is used to atomize the sample in inductively coupled plasma mass spectroscopy, or "ICP-MS." It atomizes to produce atomic and small-polyatomic ions, which were subsequently discovered. A sample solution is first introduced into the system, processed through a nebulizer, and then an inductively coupled plasma is created in the presence of an inert gas, such as argon. Following the atomization of the material by the highly ionizable plasma, polyatomic ions (fine aerosol form) were extracted to an interface area using ion optics. The polyatomic ions are focused into a quadrupole mass analyzer by the electrostatic lens of an ion optic. The detection and separation of ions occur in line with the mass by charge ratio, or "m/z ratio." In the case of AAS sample preparation, for example, the samples to be analysed are also similarly digested in an aqueous phase before being sent to ICP-MS. Deionized water is used as the diluent in sample preparation, which also involves the use of hydrochloric or nitric acid, or in certain situations, alkaline solutions⁵⁷. In 2017, Palomo-Siguero et al. synthesised Selenium NPs in the presence of stabilisers such as non-ionic surfactant (Triton X-100) or chitosan (polysaccharides) using a solution-phase approach⁵⁸.

c) *X-ray Photoelectron Spectroscopy (XPS)*

XPS techniques is one of the popular surface science methods for determining or analysing the chemical state, electrical states, and elemental composition/empirical formula of nanomaterials is called "XPS." The photoelectric effect was discovered in 1887 by Hz, and this discovery is the foundation of the XPS operating concept. The study was expanded to surface analysis later in the 1960s by Siegbahn and his research group at Uppsala University in Sweden. They also invented the acronym XPS, or electron spectroscopy for chemical analysis, for which Siegbahn was awarded a Nobel prize in physics in 1981. In qualitative analysis, the sample is bombarded with single energy, monochromatic, or monoenergetic X-ray photons (Mg K α 1253.6 eV or Al K α 1486.6 eV, line width \approx 0.7–0.85 eV), and the kinetic energy of the electrons that are emitted from the sample's topmost layer (1–10 nm) is

then calculated⁵⁹. The XPS spectrum shows distinctive peaks for the electrons released from outermost/surface atoms, making it possible to identify and measure the surface elements (apart from hydrogen and helium) that are present. By measuring or examining the minute differences that occur in the binding energies of emitted photoelectrons, auger electrons, multiple splitting, satellite peaks, etc., one can easily identify and quantify the chemical states of the elements contained inside. With the use of XPS, an extremely sensitive and high vacuum method, it is possible to identify certain elements or species by simply detecting changes in the electrical configuration of atoms or chemical bonds. Elements like C, N, O, and P are easily distinguished in the case of chitosan-based nanomaterials as they make up the majority and have distinctive peaks that match their binding energies⁶⁰. The XPS for the mildly wet synthesised gold/silver NPs in an aqueous chitosan solution was reported by Boufi et al. in 2013⁵⁹.

d) Atomic Absorption Spectroscopy (AAS)

Atomic absorption spectroscopy, or "AAS," is a very sensitive elemental analytical method that is used to ascertain the metal content at the pictogram level in a range of substances. The AAS measures the decrease in the optical radiation intensity of a cell that contains gaseous atoms from the samples. An analyte in AAS typically absorbs particular wavelengths generated by a hollow cathode lamp, or "HCL," which is utilised as a light source⁶¹. The two most often utilised atom-cells in AAS are either flames or graphitic furnaces/electrothermal atomizers, or "ETAs." In comparison with ETAs, which have a temperature that can be monitored by a power source, flames have a highly regulated combustion environment, so their sensitivity is comparatively lower. Use of inert gas, such as argon, is used to stop the combustion process at high temperatures. The sample/analyte in a "atom-cell" absorbs the particle wavelength and becomes gaseous. It then moves to a detector, which measures and separates the wavelengths of interest before processing the data in a computer/control instrumentation operation. The analyte or samples are produced by digestive processes and are often of a certain concentration in an aqueous phase in order to give maximum accuracy, precision, and fewest interferences⁶¹. It is noteworthy to highlight that each element has a unique absorption of electromagnetic radiation wavelengths for the HCL source. Put another way, the standards are used to quantify how specific and unique an element's absorbance is for the absorbing wavelength of interest. The unknown sample may be processed and the concentration can be retrieved from the digital output display unit when the standards are measured, indicating that the instrument is calibrated for specific components of interest. The underlying concept behind AAS is ionisation energy, which is essentially the energy needed

to excite an electron and varies depending on the element. Every atom in chitosan-based nanomaterials/NPs has a unique fingerprint area, which makes qualitative AAS analysis of the material possible⁶². AAS analysis may be performed against several reaction parameters, including agitation duration, reaction rate, pH, and so on because chitosan-based nanomaterials have been widely employed to encapsulate the metal ions⁶³. Generally speaking, one may compute the Concentration of encapsulated metals (%) by multiplying the ratio of released metal ions by the total amount of metals in a nanomaterial, and then storing the result. AAS was subsequently used to determine the number of metal ions after Liu et al.⁶⁴ proved the utilisation of chitosan-based nanomaterials for the metal encapsulation⁶⁴.

Applications of Chitosan-based Biogenic Nanoparticles in Wastewater Remediation

Chitosan-based biogenic nanoparticles have gained significant attention for their potential applications in wastewater remediation due to their unique properties, such as large surface area, high adsorption capacity, and versatile surface chemistry. These nanoparticles offer promising solutions for the removal of numerous contaminants from wastewater which are sourced from various routes such as natural incidence comprising of geological parental materials or outcropping of rocks, sources from agricultural activities such as application of organic and inorganic fertilizers, depositions from atmospheric emissions such as exhaust of vehicles, wear of asphalt, tires, leakage of oil or gasoline, etc. (Fig. 6) and sources from industrial activities such as mining, metals smelting, finishing, recycling, etc.⁶⁵.

Below are some of the applications of chitosan-based biogenic nanoparticles in wastewater remediation.

i. Heavy Metal Removal: Chitosan-based nanoparticles have demonstrated excellent efficiency in the removal of heavy metal ions from wastewater. The amino and hydroxyl functional groups on the chitosan surface provide active sites for chelation and complexation interactions with heavy metal ions. The large surface area and high adsorption capacity of the nanoparticles allow for the effective removal of heavy metals, comprising cadmium (Cd), lead (Pb), mercury (Hg), and arsenic (As)⁶⁶. Chitosan-based nanoparticles offer a cost-effective and environmentally friendly solution for heavy metal remediation in wastewater.

ii. Dye Degradation: Chitosan-based nanoparticles have shown remarkable potential in the degradation and removal of dyes from wastewater. The nanoparticles can adsorb and catalytically degrade a wide range of dyes, including synthetic dyes used in textile, printing, and dyeing industries. The adsorption capacity of chitosan-based nanoparticles enables the

removal of dyes from wastewater, while their catalytic properties promote the degradation of dyes through chemical reactions or photocatalysis⁶⁷. The use of chitosan-based nanoparticles for dye degradation contributes to the reduction of color and toxicity in wastewater.

iii. Organic Compound Adsorption: Chitosan-based nanoparticles have been widely investigated for the adsorption of various organic compounds present in wastewater. These nanoparticles can effectively adsorb organic pollutants such as pharmaceuticals and pesticides. The functional groups on the chitosan surface facilitate interactions, including hydrophobic interactions, hydrogen bonding, and electrostatic interactions, enabling the efficient removal of organic compounds. Chitosan-based nanoparticles offer a sustainable and efficient approach to the removal of organic pollutants from wastewater⁶, antibiotics and pharmaceutical compounds from wastewater. These nanoparticles can effectively adsorb and bind to antibiotics and pharmaceuticals, reducing their concentration in wastewater. The surface properties of chitosan, such as its positive charge, enable electrostatic interactions with negatively charged pharmaceutical compounds. By removing antibiotics and pharmaceuticals, chitosan-based nanoparticles contribute to the reduction of potential ecological risks and the prevention of antibiotic resistance in aquatic environments⁶⁸.

iv. Nutrient Removal: Chitosan-based nanoparticles have shown potential for the removal of nutrients, particularly nitrogen, and phosphorus, from wastewater. These nutrients contribute to water eutrophication and can have detrimental effects on aquatic ecosystems. Chitosan-based nanoparticles can adsorb and immobilize nutrients, preventing their release into receiving water bodies. The large surface area and high adsorption capacity of the nanoparticles make them suitable for nutrient removal, contributing to the preservation of water quality and the prevention of ecological imbalances⁶⁹.

v. Antibacterial Applications: Chitosan-based nanoparticles possess inherent antibacterial properties, making them effective in controlling microbial contamination in wastewater. The cationic nature of chitosan enables interactions with bacterial cell membranes, leading to cell disruption and inhibition of bacterial growth. Incorporating chitosan-based nanoparticles into wastewater treatment systems can help reduce bacterial contamination, prevent the spread of waterborne diseases, and enhance the overall microbiological safety of treated wastewater⁷⁰.

The efficiency of chitosan-based nanoparticles for pollutant removal

Chitosan-based nanoparticles have emerged as promising materials for pollutant removal in wastewater treatment due to their unique properties, including high adsorption capacity, versatile surface chemistry, and biodegradability. The efficiency of chitosan-based

nanoparticles in removing various pollutants depends on several factors, including the type of pollutant, nanoparticle characteristics, operating conditions, and the specific wastewater treatment process⁷¹. Below is the efficiency of chitosan-based nanoparticles for pollutant removal.

a. Adsorption Capacity: Chitosan-based nanoparticles exhibit a high adsorption capacity for a wide range of pollutants. The amino and hydroxyl groups on the chitosan surface provide active sites for adsorption through electrostatic interactions, van der Waals forces, and hydrogen bonding. The large surface area of nanoparticles allows for increased contact with the pollutants, enhancing the adsorption efficiency. The adsorption capacity of chitosan-based nanoparticles can be further improved by modifying their surface properties through functionalization or incorporation of other materials⁶.

b. Selectivity: The selectivity of chitosan-based nanoparticles refers to their ability to preferentially adsorb specific pollutants while ignoring or minimizing the adsorption of other constituents in wastewater. The surface chemistry of chitosan nanoparticles can be modified to enhance selectivity towards target pollutants. Functional groups or coatings can be introduced to promote specific interactions with the desired pollutants, allowing for more efficient removal while minimizing interference from other substances. The selectivity of chitosan-based nanoparticles contributes to their effectiveness in treating complex wastewater matrices⁷².

c. pH and Ionic Strength: The pH and ionic strength of wastewater play a crucial role in the efficiency of chitosan-based nanoparticles for pollutant removal. The surface charge of the nanoparticles and the charge distribution of the pollutants can be influenced by pH, affecting the electrostatic interactions and adsorption capacity. Adjusting the pH within the optimal range can enhance the adsorption efficiency. Additionally, the ionic strength of the wastewater affects the competition between ions and pollutants for adsorption sites. Proper consideration of pH and ionic strength is essential for optimizing the efficiency of chitosan-based nanoparticles in pollutant removal⁷².

d. Regeneration and Reusability: One of the advantages of chitosan-based nanoparticles is their potential for regeneration and reusability. After adsorbing pollutants, the nanoparticles can be regenerated through desorption or other methods, allowing for repeated use in wastewater treatment. Regeneration techniques such as pH adjustment, solvent extraction, or thermal treatment can be employed based on the nature of the pollutant and nanoparticle characteristics. The ability to regenerate and reuse chitosan-based nanoparticles enhances their cost-effectiveness and sustainability as compared to single-use adsorbents²⁰.

Chitosan-based incorporated Nanoparticles

In recent years, various studies have explored the synthesis of chitosan-based biogenic nanoparticles by incorporating different types of nanoparticles. This approach aims to enhance the properties and functionality of chitosan nanoparticles for efficient wastewater remediation. Here, we discuss the synthesis and adsorption potential of chitosan-based biogenic nanoparticles incorporated with other nanomaterials reported in the literature as shown in Table 3.

i. Metal Nanoparticles:

a. Silver Nanoparticles (AgNPs): The synthesis of chitosan-based biogenic nanoparticles incorporating silver nanoparticles has been widely investigated. One common method involves the reduction of silver ions using chitosan as a reducing and stabilizing agent. The resulting chitosan-silver nanoparticles exhibit antimicrobial properties, making them effective for the removal of bacteria and pathogens from wastewater⁷³.

b. Iron Oxide Nanoparticles (Fe_3O_4 NPs): Chitosan-based biogenic nanoparticles combined with iron oxide nanoparticles have been developed for the removal of heavy metals from wastewater. The synthesis typically involves the co-precipitation of chitosan and iron salts, followed by the reduction of the iron ions. The resulting chitosan-iron oxide nanoparticles exhibit excellent adsorption capacity for heavy metal ions, such as lead and cadmium⁷⁴.

c. Cobalt Ferrite Nanoparticles ($CoFe_2O_4$ NPs): Chitosan-based biogenic nanoparticles combined with cobalt ferrite nanoparticles have shown promising potential for wastewater treatment. The synthesis typically involves the co-precipitation of chitosan and metal salts, followed by the addition of ferrite precursors and subsequent annealing. The resulting chitosan-cobalt ferrite nanoparticles exhibit high adsorption capacity and magnetic responsiveness, enabling the effective removal of pollutants, particularly heavy metal ions⁷⁵.

ii. Carbon-based Nanoparticles:

a. Graphene Oxide Nanoparticles (GO NPs): Chitosan-based biogenic nanoparticles incorporating graphene oxide have gained attention for their excellent adsorption properties. The synthesis involves the dispersion of graphene oxide in a chitosan solution, followed by the crosslinking of chitosan chains to form nanoparticles. The resulting chitosan-graphene oxide nanoparticles possess a large surface area and high adsorption capacity for organic pollutants, including dyes and pharmaceutical compounds⁷⁶.

b. Carbon Nanotubes (CNTs): Chitosan-based biogenic nanoparticles combined with carbon nanotubes have been investigated for wastewater treatment applications. The synthesis

typically involves the dispersion of carbon nanotubes in a chitosan solution, followed by the formation of nanoparticles through crosslinking or precipitation methods. The resulting chitosan-carbon nanotube nanoparticles exhibit enhanced adsorption capacity for various pollutants, like heavy metals and organic compounds⁷⁷.

iii. Semiconductor Nanoparticles:

a. Titanium Dioxide Nanoparticles (TiO₂ NPs): Chitosan-based biogenic nanoparticles incorporating titanium dioxide nanoparticles have been widely studied for photocatalytic wastewater treatment. The synthesis typically involves the dispersion of TiO₂ nanoparticles in a chitosan solution, followed by the formation of nanoparticles through gelation or precipitation methods. The resulting chitosan-TiO₂ nanoparticles exhibit photocatalytic activity and can efficiently degrade organic pollutants under light irradiation⁷⁸.

b. Zinc Oxide Nanoparticles (ZnO NPs): Chitosan-based biogenic nanoparticles incorporating zinc oxide nanoparticles have also been explored for wastewater remediation. The synthesis involves the dispersion of ZnO nanoparticles in a chitosan solution, followed by the formation of nanoparticles through chemical or physical methods. The resulting chitosan-ZnO nanoparticles exhibit adsorption and photocatalytic properties, making them effective for the removal of pollutants in wastewater²⁰.

iv. Composite Nanoparticles:

a. Hybrid Nanoparticles: Chitosan-based biogenic nanoparticles can be synthesized by combining chitosan with multiple types of nanoparticles, creating hybrid systems with enhanced functionalities. For example, a chitosan-based hybrid nanoparticle could incorporate both metal nanoparticles and carbon-based nanoparticles, combining the adsorption and catalytic properties of different materials. This approach allows for synergistic effects, improving pollutant removal efficiency in wastewater treatment⁷⁹.

b. Core-Shell Nanoparticles: Chitosan-based biogenic nanoparticles can also be designed as core-shell structures, where a chitosan core is coated with a layer of another nanoparticle material. This design provides additional advantages such as controlled release of active components and protection of the core material from degradation. For example, a chitosan core coated with silver nanoparticles can provide both antimicrobial properties and adsorption capabilities for wastewater treatment⁸⁰.

v. Quantum Dots: Quantum dots (QDs) are semiconductor nanoparticles with unique optical and electronic properties. Incorporating QDs into chitosan-based biogenic nanoparticles offers exciting possibilities for pollutant removal and detection in wastewater. One approach involves the synthesis of chitosan-QD hybrid nanoparticles through electrostatic interactions

or covalent bonding. The resulting chitosan-QD nanoparticles can effectively adsorb heavy metals and organic pollutants, while the QDs provide a fluorescence-based detection platform for monitoring pollutant concentrations in real-time⁸¹.

vi. Clay Nanoparticles: Clay nanoparticles, such as montmorillonite and halloysite, possess a high surface area and a layered structure, making them suitable for pollutant adsorption. Chitosan-based biogenic nanoparticles incorporating clay nanoparticles have been developed for wastewater treatment. The synthesis typically involves the dispersion of clay nanoparticles in a chitosan solution, followed by crosslinking or gelation. The resulting chitosan-clay nanoparticles exhibit enhanced adsorption capacity for a wide range of pollutants, including heavy metals, dyes, and organic compounds⁸².

vii. Metal-Organic Frameworks (MOFs): Metal-organic frameworks are porous materials made up of metal ions or clusters coordinated with organic ligands. Combining MOFs with chitosan-based biogenic nanoparticles offers a synergistic effect for pollutant removal and degradation. The synthesis typically involves the encapsulation of MOFs within the chitosan matrix or the functionalization of chitosan with MOF particles. The resulting chitosan-MOF nanoparticles exhibit high surface area, porosity, and selective adsorption properties, making them efficient for removing various pollutants, such as volatile organic compounds, dyes, and heavy metals⁸³.

Drawbacks and Challenges of chitosan-based nanoparticles

Chitosan-based nanoparticles have gained attention in recent years as a promising solution for wastewater treatment due to their unique properties, including biocompatibility, biodegradability, and excellent adsorption capabilities. However, like any technology, they also come with their share of drawbacks and challenges. Below are some of the key limitations and obstacles associated with chitosan-based nanoparticles in wastewater treatment:

- i. **Limited stability and agglomeration:** Chitosan-based nanoparticles can exhibit poor stability in aqueous environments, leading to aggregation or precipitation. This can reduce their effectiveness in adsorbing contaminants and may require the addition of stabilizing agents.
- ii. **Cost and production:** The production of chitosan-based nanoparticles can be expensive, especially when obtaining high-quality chitosan from natural sources like crustacean shells. Additionally, the synthesis of nanoparticles often involves energy-intensive processes, increasing operational costs.

iii. Difficult recovery and regeneration: Once chitosan-based nanoparticles adsorb contaminants in wastewater, their recovery and regeneration for reuse can be challenging. Regenerating the nanoparticles typically requires harsh chemical treatments, which may decrease their efficiency over time and generate additional waste.

iv. Limited selectivity: Chitosan-based nanoparticles are generally effective at adsorbing a wide range of contaminants, but they may not exhibit high selectivity for specific pollutants. This lack of selectivity can lead to the removal of both harmful and beneficial substances from wastewater.

v. pH and ionic strength sensitivity: The adsorption capacity and stability of chitosan-based nanoparticles can be influenced by the pH and ionic strength of the wastewater. These sensitivity issues may limit their applicability in treating wastewater with varying chemical compositions.

vi. Competitive adsorption: In complex wastewater matrices, chitosan-based nanoparticles may compete with other ions and molecules for adsorption sites. This competition can reduce their efficiency in removing target pollutants.

vii. Limited scalability: While chitosan-based nanoparticles have shown promise in laboratory studies, scaling up their production and application for industrial wastewater treatment can be challenging. Ensuring consistent performance and cost-effectiveness at larger scales is a significant hurdle.

Conclusion and Future Research Directives

Chitosan-based nanoparticles offer versatile functions for wastewater remediation owing to their unique properties, including biodegradability, biocompatibility, and high surface area. Various synthesis methods have been explored to fabricate chitosan-based nanoparticles, incorporating different types of nanoparticles, such as metal nanoparticles, metal oxides, or carbon-based nanoparticles. Characterization techniques have been employed to assess the physicochemical properties, including size, shape, surface area, and porosity, of chitosan-based nanoparticles. The efficiency of chitosan-based nanoparticles in pollutant removal has been demonstrated through their applications in heavy metal removal, dye degradation, and organic compound adsorption. The mechanisms involved in pollutant adsorption and degradation by chitosan-based nanoparticles have been elucidated, including chemical interactions, electrostatic attraction, and catalytic processes. The significance of chitosan-based biogenic nanoparticles in wastewater remediation cannot be overstated. They offer a sustainable and cost-effective solution for the removal of various pollutants from wastewater,

contributing to the protection of our environment and human health. The unique properties of chitosan-based nanoparticles, coupled with their ability to be synthesized with different nanoparticles, enable tailored approaches for specific pollutant removal. In light of the findings presented in this review, several suggestions for further research can be proposed. Firstly, exploring the potential of chitosan-based nanoparticles in the removal of emerging contaminants and microplastics is an important area of investigation. These pollutants pose significant challenges to conventional wastewater treatment methods and require innovative approaches for effective removal. Additionally, the development of scalable synthesis techniques, optimization of process parameters, and integration of chitosan-based nanoparticles with other treatment technologies should be further explored to enhance their applicability in real-world wastewater treatment systems. Furthermore, comprehensive studies on the long-term environmental impacts and the fate of chitosan-based nanoparticles in wastewater treatment are essential. Understanding their potential accumulation, biodegradability, and ecotoxicity is crucial to ensure their safe and sustainable use.

Figures:

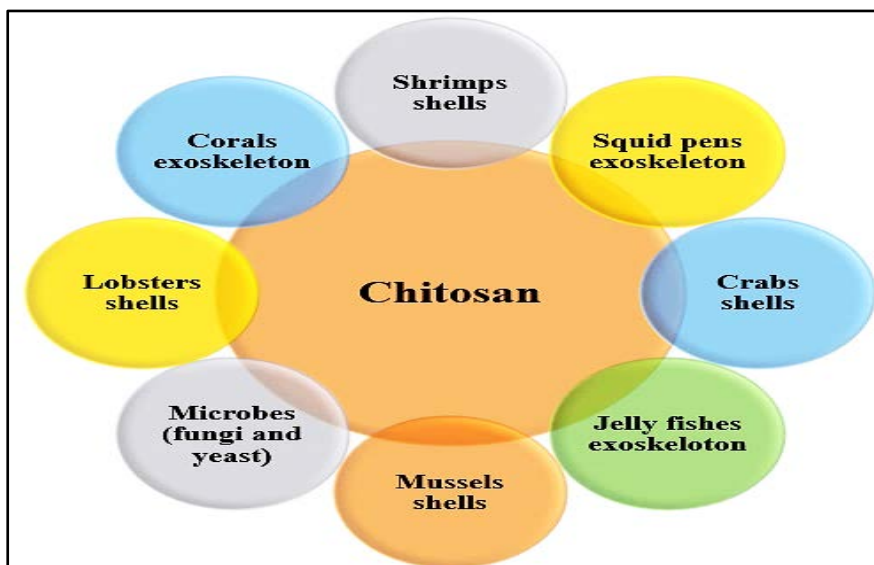


Fig. 1: Various shells and cell walls sources of biopolymer chitosan

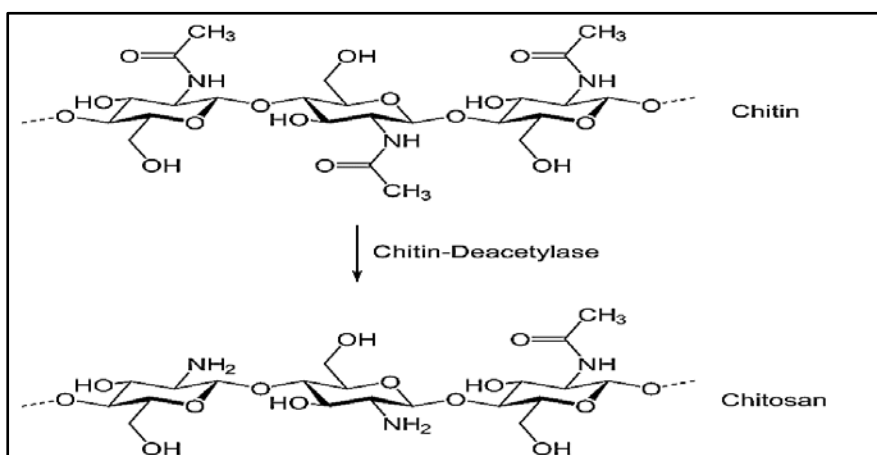


Fig. 2: The structural configuration of Chitin and Chitosan biopolymer

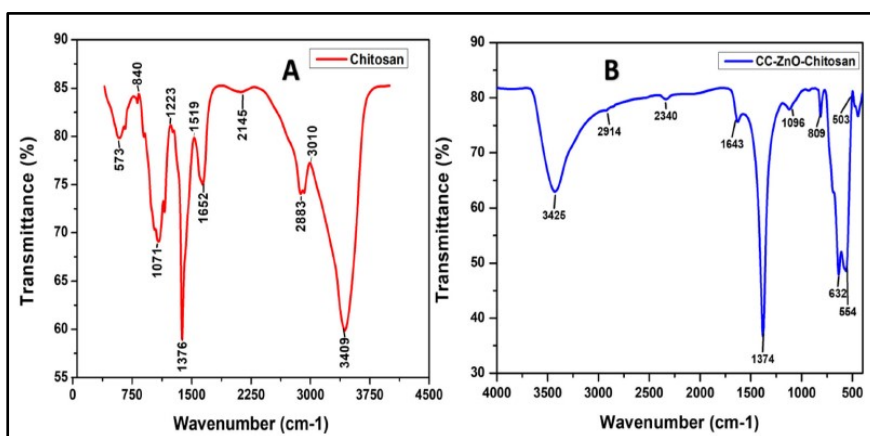


Fig. 3: FTIR spectra of synthesized nanomaterials. A) Chitosan, (B) CC-ZnO-Chitosan²⁰.

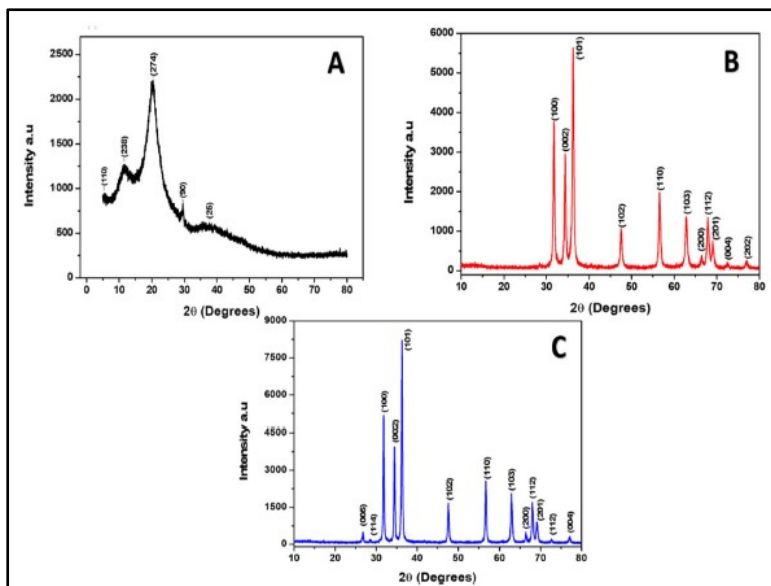


Fig. 4: XRD spectra of a synthesized nanomaterial. A) Chitosan, (B) ZnO, (C) ZnO-Chitosan²⁰

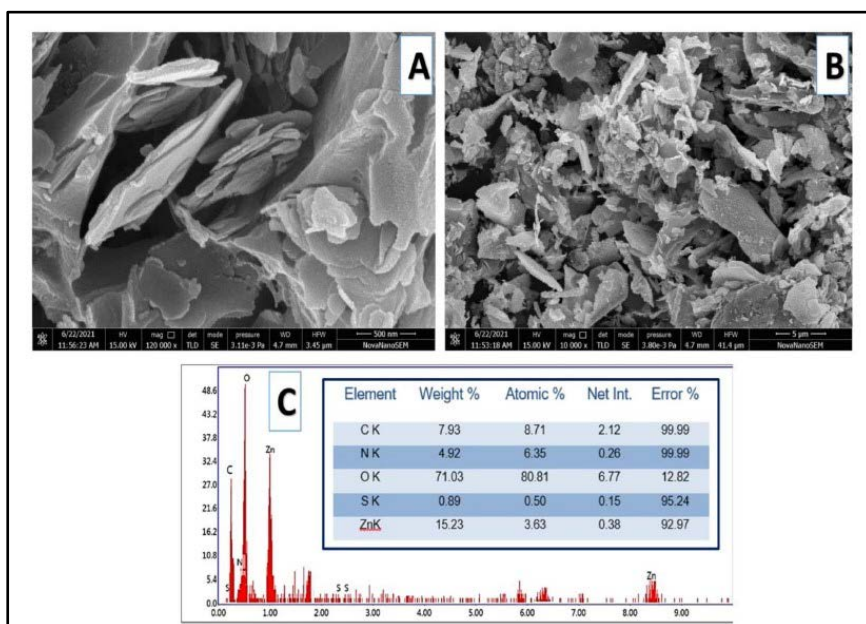


Fig. 5: A) FE-SEM of synthesized CC-ZnO-Chitosan. B) EDX of Synthesized ZnO-Chitosan²⁰

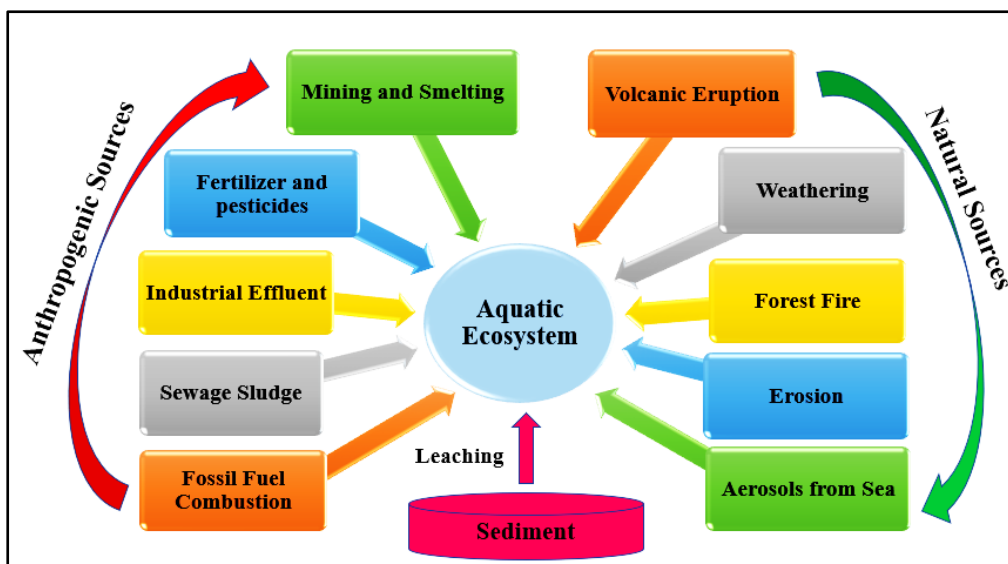


Fig. 6: Sources of heavy metals pollution in the aquatic ecosystem

Tables:

Table 1: Different types of chitosan and their characteristics

Chitosan Properties	α -Type Chitosan	β -Type Chitosan	γ -Type Chitosan	References
Chitosan source	Shrimps and Crabs	Squid's pens	Fungi cell wall	84
Degree of crystallinity	Moderately Lower crystallinity	Higher crystallinity	Moderately lower	85
Rate of stability	Higher stability rate	Least stability rate	Lower stability rate	86
Medium of solubility	Soluble in acid medium	Soluble in acid medium	Soluble in acid medium	87
Molecular weight volume	Highest volume	Higher volume	Lower volume	7
Structural shape	Strands are antiparallel	Strands are Parallel	Contain both parallel antiparallel strands	84
Rate of reactivity	More reactive	Most reactive	More reactive	88

Table 2: Preparation techniques for synthesizing chitosan nanoparticles

Technique	Principle	Merit (s)	Demerit (s)	References
Spray drying	Atomization	simple and speedy process, other drying or separation steps not required	particle size is large, incompatible with sensitive temperatures, substances	⁸⁹
Emulsification and crosslinking	Covalent crosslinking	Simple processing	harmful chemicals involved	90
Phase inversion precipitation	Precipitation	High encapsulation of some compounds	shear force is required, harmful chemicals involved	91
Reversed micelles	Covalent crosslinking	NPs Ultrafine less than 100 nm	Complex application, harmful chemicals involved, Time-consuming process	92
Ionic gelation with radical polymerization	Polymerization and crosslinking	-	Complex application, Time-consuming process	93
Supercritical-CO ₂ -assisted solubilization and atomization (SCASA)	Atomization	Non-harmful solvent, other drying or separation steps not required	Complex application, Time-consuming, harmful chemicals involved, specially designed system required, large particle size involved	94
Emulsion-droplet coalescence	Precipitation	-	high shear force required, harmful chemicals involved,	95
Self-assembly	Hydrophobic and/or electrostatic interaction	NPs Highly stable, with mild chemicals involved, and Modifiable procedure	Difficulty in controlling at large scale	96

Ionic gelation	Ionic crosslinking	Simple process, mild Chemicals involved, NPs adjusting	-	97
Top-down	Acid hydrolysis and deacetylation	-	Complex application, Time-consuming, extra step for drug loading is required	98

Table 3: Chitosan-based incorporated nanoparticles and removal efficiency from literature

Adsorbent	Adsorbate	Adsorption Capacity (mg/g)	Reference
ZnO/CHS	Methylene Blue	99%	20
CdO/NiO	Rhodamine B	90%	67
CSGO aerogels	Methyl orange	686.89	99
	Amido black 10B	573.47	99
ZnO-Chitosan	Malachite green	54%	100
Ce-ZnO-Chitosan	Malachite green	87%	100
Fe ₃ O ₄ /GO/CHS	Reactive Blue 19	102.06	101
Fe ₃ O ₄ -CHS	Pb(II)	78.58 -487.5	71
CHS/Fe ₃ O ₄	Cr(VI)	162	102
Fe ₃ O ₄ /GO/CHS	Ni(II)	80.48	101
Fe ₃ O ₄ /CHS	Cd(II), Pb(II)	36.42, 79.24	103
SiO ₂ @CHS	As(V), Hg(II)	198.6, 204.1	104
CHS-EDTA	Pb(II), Cd(II), Cu(II)	370.37, 243.90, 227.27	105
TiO ₂ /CHS	Cu(II), Pb(II)	526.5-715.7, 475.5-579.1	106
Fe ₃ O ₄ @CHS@DMSA	Cd(II)	314.12	81

Magnetic xanthate CHS /polyacrylic acid	Cu(II), Cd(II), Pb(II), Co(II)	178, 168,140	107
3,3-diphenylpropylimine methyl benzaldehyde / CHS	Pb(II)	230.48	108
Glucan/CHS	Pb(II), Cu(II), Co(II), Cd(II), Ni(II)	395, 342, 232, 269, 184	109
NOCC-MNPs/CHS-citrate gel beads (CCGBs)	Cu(II)	294.11	110
CHS grafted with methyl methacrylate (M-CS)	Cu(II)	192.31	111
CHS/calcium alginate /bentonite	Pb(II), Cu(II), Cd(II)	434.89, 115.30, 102.38	112
CHS/g-acrylamide	Cr(VI), Cu(II)	178.34, 181.88	113
CHS grafted UiO-66-NH ₂	Pb(II), Cu(II)	555.56, 364.96	114
CHS microspheres	Cu(II)	75.52	115
AgNPs/GO/CHS	Mn(II)	1605	116
CHS -carboxyl groups	Cu(II), Zn(II)	220.5, 124.3	117
CHS microspheres/sodium alginate hybrid beads	Pb(II), Cr(VI)	180, 16	118
Magnetic thiolated /quaternized-CHS	Pb(II), As(V), Hg(II), As(III), Cu(II)	235.63, 66.27, 28.00, 67.69, 33.99	119

References

1. M. A. Onu, O. O. Ayeleru, B. Oboirien, and P. A. Olubambi. *Envi. Chall.* 10(6),86, 2023.
2. P. Rajasulochana, and V. Preethy. *Res. Tech.* 9(4), 69, 2016.
3. D. Dutta, S. Arya and S. Kumar. *Chemos.* 13(1), 245, 2021.
4. M. C. Goci, T. Leudjo, A. L. Martin and M. J. Klink. *Polym.* 15(3), 482, 2023.
5. E. I. Rabea, M. E. T. Badawy, C. V. Stevens, G. Smagghe and W. Steurbaut, 34(1), 30, 200.
6. D. C. Alves, B. Healy, L. A. Pinto, T. R. Cadaval and C. B. Breslin. *Mole.* 26(3), 594, 2021.
7. S. Kou, L. M. Peters and M. R. Mucalo. *Int. Jou. Biol Macromol.* 12(5), 784 2020.
8. L. Bastiaens, L. Soetemans, E. D'Hondt and K. Elst, Sources of chitin and chitosan and their isolation. Wiley Eastern Limited, edn. 4 (2019).
9. S. Kumari, P. Rath, S. H. Kumar and T. N. Tiwari. *Environ. Tech. Innov.* 6(25), 476, 2015.
10. D. Sakthivel, N. Vijayakumar and A. V. Hum. *Journals Res. Artic.* 13(5),2015.
11. M. A. García, P. Nilia, C. Castro, L. J. Rodríguez, M. R. Robin, Z. P. Gañán, C. J. Alicia *Radiat. Res. Appl. Sci.* 13(4), 2015.
12. L. Handayani, F. Syahputra, and A. Y. J. Kim. *Sains. dan Apl.* 21(4), 224-231 2018.
13. N. E. A. El-Naggar, W. E. A. Saber, A. M. Zweil and S. I. Bashir. *Sci. Rep.* 4 (15), 98, 2022.
14. M. Malerba and R. Cerana. *Int. Jou. of Mol. Sci.* 17(7), 996, 2016.
15. Z. K. Jugovic, Z. Petronijevic and A. Smelcerovic, *Bio. Act. and App.* 14(3), 981, 2010.
16. M. Yanat, and K. Schroën, *React. Funct. Polym.* 10(4), 849, 2021.
17. U. M. S. P. Perera, and N. Rajapakse 46(14), 9590, 2014.
18. S. Boruah and P. Dutta, *Indian Phytopathol.* 42(3), 60, 2021.
19. M. Iriti, and E. M. Varoni, *Environ. Sci. Pollut. Res.* 11(3), 56, 2015.
20. U. L. Usman, N. B. Singh, B. K. Allam and S. Banerjee, *Macrom. Sym.* 20(21), 357, 2023.
21. G. Ilangumaran, G. Stratton, S. Ravichandran, P. S. Shukla, P. Potin, S. Asiedu, and B. Prithiviraj. *Front. Microbiol.* 7(81), 593, 2017.

22. M. Abhinaya, R. Parthiban, P. S. Kumar and D. V. N. Vo, *Environ. Res.* 11(9), 96, 2021.
23. X. Jingwen, X. Wancui, J. Yu, R. Xin, Z. Shi, L. Song and X. Yang *Front. Microbiol.* 67(7), 126, 2021.
24. I. Younes and M. Rinaudo. *Marine Drugs* 13(3), 133, 2015.
25. S. C. M. Queiroz, A. Rayane, B. R. L. F. Paschoal, Lima, V. A. O. Í. de Farias R. Raid, E. P. N. Lima, R. J. L. da Silva, C. P. C. Andrés, and M. V. Lia Fook. *Mar. Drugs* 15(5), 141, 2017.
26. G. A. Martau, M. Mihai and D. C. Vodnar. *Polymers.* 11(18), 37, 2019.
27. N. A. Negm, H. H. H. Hefni, A. A. A. Abd-Elaal, E. A. Badr & A. Kana, M. T. H. *Int. Jou. of Bio. Macromo.* 2(1), 96, 2020.
28. S. Islam, M. A. R. Bhuiyan and M. N. Islam. *Jou. of Poly. and the Env.* 10(9), 24, 2017.
29. S., Syamdidi, H. Sidauruk, A. Munandar, and S. Haryati *Web of Conferences.* 14(7), 3025, 2020.
30. X. Li, H. Xu, Z. S. Chen and G. Chen, *Jou. of Nanoma.* 27(9), 74, 2011.
31. B. Andujar, Dr. thesis, UCL (University Coll. London). 2014.
32. S. Ying, Z. Guan, P. C. Ofoegbu, P. Clubb, C. Rico, F. He, J. Hong. *Env. Tech. and Inn.* 10(2), 336, 2022.
33. P. Mohanpuria, N. K. Rana and S. K. Yadav. *Jou. of Nanop. Res.* 11(5), 79275, 2008.
34. P. Dutta, and P. K. Kaman. *Int. J. Curr. Microbiol. Appl. Sci.* 60(6), 336, 2017.
35. D. Sharma, S. Kanchi and K. Bisetty. *Arab. Jou. of Chem.* 20(15), 11002, 2019.
36. K. Guzmán, B. Kumar, M. J. Vallejo, M. Grijalva, A. Debut, L. Cumbal. *Prog. Org. Coatings* 10(10), 1568, 2019.
37. C. Thambiliyagodage, M. Jayanetti, A. Mendis, G. Ekanayake, H. Liyanaarachchi, S. Vigneswaran. *Materials* 60(5), 2073, 2023.
38. L. Pellenz, C. R. S. de Oliveira, A. H.S. Júnior, L. J. S. Silva, L. Silva, A. A. U. Souza, S. M. Arruda, G. U. de Souza, F. H. Borba, A. Silva. *Sep. and Pur. Tech.* 12(2) 435, 2023.
39. M. M. López, A. R. Moraga, A. J. L. Jimenez, J. C G. Martínez, O. Ahrazem, L. G. Gómez, E. Niza *Carbohydr. Polym.* 11(8), 815, 2022.
40. S. Mourdikoudis, R. M. Pallares and N. T. K. Thanh, *Nanoscale* 21(2), 785, 2018.
41. F. Brunel, N. E. El Gueddari and B. M. Moerschbacher *Carb. Polym.* 20(12), 1025, 2013

42. W. Wong-Ng, H. F. McMurdie, C. R. Hubbard and A. D. J. Mighell Res. Natl. Inst. Stand. Technol. 10(6), 152, 2001.
43. M. Gonon, Encyclopedia of Materials: Techn. Ceram. and Glass. 81(8), 542, 2021.
44. J. W. Rhim, Hong, S. I., Park, H. M. and Ng, P. K. W. J. Agric. Food Chem. 6(6), 58, 2006.
45. A. Parupudi, S. H. R. Mulagapati and J. A. Nanoparticle Therapeutics 82(7), 574, 2022.
46. S. P. Facchi, D. B. Scariot, P. V. A. Bueno, P. R. Souza, L. C. Figueiredo, H. D. M.Follmann, C. S. Nunes, J. P. Monteiro, E. G. Bonafé, C. V. Nakamura, E. C. Muniz, A. F. Martins Int. J. Biol. Macromol. 10(16), 363, 2016.
47. T. Banerjee, Mitra, S., K. Singh, A., K. Sharma, R. & Maitra, A. Int. J. Pharm. 267(3), 378- 5173 2002.
48. V. Saharan, A. Mehrotra, R. Khatik, P. Rawal, S.S. Sharma, A. Pal Int. J. Biol. Macromol. 31(12), 236, 2013.
49. R. C. Choudhary, R. V. Kumaraswamy, S. Kumari, S. S. Sharma, A. Pal, R. Raliya, P. Biswas and V. Saharan Sci. Rep. 41(5), 98, 2017.
50. T. Jain, Srivastava, K., S. Kumar and P. K. Dutta, Plant Sciences 10(16), 9739, 2022.
51. R. C. Choudhary, R. V. Kumaraswamy, S. Kumari, A. Pal, R. Raliya, P. Biswas & V. Saharan. Nanotechnology 97(8), 981, 2017.
52. A. Dev, N. S. Binulal, A. Anitha, S.V. Nair, T. Furuike, H. Tamura, R. Jayakumar Carbohydr. Polym. 20(9), 12040, 2010.
53. S. F. Hosseini, Zandi, M., Rezaei, M. and Farahmandghavi, F. Carbohydr. Polym. 10(16), 684, 2013.
54. S. E. Harding, Methods Mol. Biol. 8(9), 603, 1994.
55. J. Stetefeld, S. A. McKenna, and T. R. Patel, Biophysical Reviews 25(5), 60218, 2016.
56. G. L. yin, Jiang, Y. ren, Huang, K. long, Ding, P. and Chen, J. J. Alloys Compd. 6(13), 270, 2008.
57. S. C. Wilschefski, and M. R. Baxter, Clin. Biochem. 3(3), 176, 2019.
58. M. Palomo-Siguero, P. Vera, Y. Echegoyen, C. Nerin, C. Cámara, Y. Madri. Spectrochim. Acta - Part B At. Spectrosc. 6(7), 239, 2017.
59. S. Boufi, Vilar, M. R., Ferraria, A. M. and Botelho do Rego, A. M. Colloids Surfaces Physicochem. Eng. Asp. 16(2), 836.

60. A. Trapani, E. De Giglio, D. Cafagna, N. Denora, G. Agrimi, T. Cassano, S. Gaetani, V. Cuomo, G. Trapani *Int. J. Pharm.* 10(16), 7036, 2011.
61. M.J Cal-Prieto, M Felipe-Sotelo, A Carlosena, J. M. Andrade, P López-Mahía, S Muniategui, D. P. Talanta. 39(9), 140434, 2002.
62. D. J. Butcher, *Encyclopedia of Analytical Science: Second Edition* 36(9), 397, 2004.
63. Y. A. Azarova, Pestov, A. V., Ustinov, A. Y. and Bratskaya, S. Y. *Carbohydr. Polym.* 6(15), 7086, 2015.
64. X. D. Liu, Tokura, S., Haruki, M., Nishi, N. and Sakairi, N. *Carbohydr. Polym.* 10(6), 8617, 2002.
65. M. S. Islam, Hossain, M. B., Matin, A. and I. Sarker, M. S. *Chemosphere* 8(3), 771, 2018.
66. L. Zhang, Zeng, Y. and Z. Cheng. *Journal of Molecular Liquids* 10(16), 654, 2015.
67. S. A. Qamar, Ashiq, M., Jahangeer, M., Riasat, A. and Bilal, M. *Chem. Environ. Eng.* 10(21), 3682, 2020.
68. A. M. Eltaweil, H. G. Omer, N. M. G. El-Aqapa, F. A. Nour, M. G. El-Subruiti, M. S. Mohy-Eldin, E. M. Abd El-Monaem. *Carbohydrate Polymers* 16(1), 8671, 2021.
69. M. Másson *Polymer Science* 10(11), 712, 2021.
70. E. M. Abd El-Monaem, A. S. Eltaweil, H. M. Elshishini, M. Hosny, M. M. Abou Alsoaud, Nour F. Attia, G. M. El-Subruiti, A. M. Omer. *Arab. Jou. of Chem.* 16(2), 103743, 2022.
71. U. L. Usman, Singh, N. B., Allam, B. K. and Banerjee, S. *Mater. Today Proc.* 2(2), 2311, 2022.
72. A. Benettayeb, F. Seihoub, P. Pal, S. Ghosh, M. Usman, C. Hua Chia, M. Usman and M. Sillanpää *Nanomaterials* 30(3), 447, 2023.
73. Y. Yu, Z. Zhou, G. Huang, H. Cheng, L. Han, S. Zhao, Y. Chen, F. Meng. *Water Research* 11(8), 901, 2022.
74. T. A. Aragaw, Bogale, F. M. and Aragaw, B. A. *Journal of Saudi Chemical Society* 10(1), 280, 2021.
75. V. Srivastava, Kohout, T. and Sillanpää, M. J. *Environ. Chem. Eng.* 16(6), 1342, 2016.
76. A. K. Sarkar, J. K. Bediako, J. W. Choi and Yun, Y. S. *NPG Asia Mater.* 41(4), 27018, 2019.
77. B. Arora and P. Attri, *Journal of Composites Science* 4(3), 135, 2020.

78. V. L. Punzi, V. Z. Kungne and Skaf, D. W. Environ. Prog. Sustain. Energy 13(4), 314, 2020.
79. M. Martínez-Cabanas, L. M., J. L. Barriada, R. Herrero and Sastre de Vicente, M. E. Chem. Eng. J. 16(4), 149, 2016.
80. K. S. Prasad, Gandhi, P. and K. Selvaraj, Appl. Surf. Sci. 140(9), 2442, 2014.
81. J. S. Algethami, A. A. Alqadami, S. Melhi, M. A. M. Alhamami, A. M. Fallatah, and M. A. Rizk. Adsorp. Sci. & Techn. 22(4), 8249, 2022.
82. S. Biswas, J. Fatema, T. Debnath and T. U. Rashid, ACS ES and T Water 2(11), 2075, 2021.
83. K. Tan, N.R Nijem, Y. Gao, S. Zuluaga, J. Li, T. Thonhauser and Y. J Chabal. Cryst Eng Comm 10(3), 940140, 2015.
84. L. D. Fernando, M. C. D. Widanage, J. P., Andrew S L., N. Washton, J. P. Latgé, P. Wang, L. Zhang, T. Wang Front. Mol. Biosci. 7(2), 7053, 2021.
85. M. Ioelovich, Research and Reviews: Journ. of Chem. 3(3), 938, 2014.
86. H. K. No, Kim, S. H., Lee, S. H., N. Y. Park, and W. Prinyawiwatkul, Carbohydr. Polym. 1(2), 1036, 2006.
87. D. P. Chattopadhyay and M. S. Int. J. Polym. Sci. 9(3), 9536, 2010.
88. M. B., Kaczmarek, S. K. Swita, Li, X., S. M. Antczak and M. Daroch, Front. in Bioeng. and Biotech. 2(4) 336, 2019.
89. E. Başaran, E. Yenilmez, M. S. Berkman, G. Büyükköroğlu, and Y. A. J. Yazan, Micro.encapsul. 8(5), 839, 2014.
90. Q. Wang, T., Cochrane, C. and McCarron, P. Coll. Surf. B Bioint. 10(1) 62024, 2005.
91. A. Grenha, Journ. of Drug. Targ. 6(5), 4121, 2012.
92. M. H. Kafshgari, M. Khorram, M. Mansouri, A. Samimi, and S. Osfour. Iran. Polym. J. English Ed. 13(7), 265, 2012.
93. S. Sajeesh, and C. P. J. Sharma, Biomed. Mater. Res. 3(3), 726, 2006.
94. N. Hijazi, N. Le Moigne, E. Rodier, M. Sauceau, T. Vincent, J. Benezet, J. Fages Polym. Eng. Sci. 2(4), 983, 2019.
95. H. Ichikawa, H. Tokumitsu, M. Miyamoto, and Y. Fukumori Nanot. for the Lif. Sci. 9(7), 835, 2003.
96. J. P. Quiñones, H. Peniche, and C. Peniche, Polymers 3(3), 30235, 2018.
97. W. Fan, Yan, W., Xu, Z. and Ni, H. Coll. Surf. B Biointerfaces 10(1), 62011, 2012.
98. R. N. Wijesena, N. Tissera, Y. Y. Kannangara, Y. Lin, G. A. J. Amaratunga, K. M. Nalin de Silva Carbohydr. Polym. 10(1), 62014, 2015.

99. Y. Wang, G. Xia, C. Wu, J. Sun, R. Song, W. Huang *Carbohydr. Polym.* 10(1), 1409, 2015.
100. A. M. Saad, M. R. Abukhadra, S. Abdel-Kader Ahmed, A. M. Elzanaty, A. H. Mady, M. A. Betiha, J. Shim, A. M. Rabie. *J. Environ. Manage.* 1(10), 3043, 2020.
101. T. T. Nhi Le, V. Thuan Le, M. U. Dao, Q. V. Nguyen, T. Thu Vu, M. H. Nguyen, D. L. Tran & H. Sinh Le *Chem. Eng. Commun.* 20(6), 1337–1352, 2019.
102. S. M. Pourmortazavi, H. Sahebi, H. Zandavar, and S. Mirsadeghi, *Compos. Part B Eng.* 10(7), 130, 2019.
103. H. L. Fan, S. F. Zhou, W. Z. Jiao, G. S. Qi and Y. Z. Liu. *Carbo. Polym.* 1(7), 7050, 2017.
104. J. Liu, Y. Chen, T. Han, M. Cheng, W. Zhang, J. Long and X. Fu. *Chemos.* 8(9), 172, 2019.
105. M. Verma, W. Ahmad, J. Park, V. Kumar, S. Mikhail, D. Vlaskin, G. Vaya and H. Kim *J. Water Process Eng.* 10(2), 989, 2022.
106. A. Razzaz, S. Ghorban, L. Hosayni, M. Irani, and M. J. Aliabadi. *Taiwan Inst. Chem. Eng.* 5(6), 5613, 2016.
107. L. Dong, C. Shan, Y. Liu, H. Sun, B. Yao, G. Gong, X. Jin, and S. Wang. *Int. J. Environ. Res. Public Health* 19(17), 11123, 2022.
108. S. Shahraki, Delarami, H. S., Khosravi, F. and Nejat, R. *J. Colloid Interface Sci.* 20(10), 5006, 2020.
109. C. Jiang, X. Wang, G. Wang, C. Hao, X. Li and T. Li. *Compos. Part B Eng.* 1(9), 3082, 2019.
110. Mi, F. L., Wu, S. J. and Chen, Y. C. *Carbohydr. Polym.* 1(5), 6031, 2015.
111. Z. A. Sutirman, E. A. Rahim, M. M. Sanagi, K. J. Abd Karim. and W. A. Wan Ibrahim. *Int. J. Biol. Macromol.* 20(3), 4115, 2020.
112. Z. Lin, Yang, Y., Liang, Z., Zeng, L. and Zhang, A. *Polymers (Basel).* 13(11), 1891, 2021.
113. S. Pavithra, G. Thandapani, S Sugashini, P.N. Sudha, H. Hussein, A. F. Alkhamis, M. H. Almutairi. *Chemos.* 12(9), 415, 2021.
114. S. Hu, Z. Huang, T. Zhang, N. Lei, Y. Zhou and Y. Wang. *Carbohydr. Polym.* 11(8), 809, 2022.
115. B. Wang, Z. Bai, H. Jiang, P. Prinsen, R. Luque, S. Zhao and J. Xuan *J. Hazard. Mater.* 18(10), 3024, 2019.

116. A. El Shahawy, M. F. Mubarak, M. El Shafie and H. M. Abdulla, RSC Adv. 20(4), 693, 2022.
117. A. M. Abu El-Soad, G. Lazzara, M. O. Abd El-Magied, G. Cavallaro, J. S. Al-Otaibi, M. I. Sayyed, and E. G. Kovaleva Int. J. Mol. Sci. 2(3), 42396, 2022.
118. E. H. Ablouh, Z. Hanani, N. Eladlani, M. Rhazi. and M. Taourirte. Sustain. Environ. Res. 42(8), 34019, 2019.
119. X. Song, Li, L., Zhou, L. and Chen, P. Chem. Eng. Res. Des. 8(6), 1425, 2018.

Temperature Assisted Ligand Conversion from 3R-MoS₂ to α -MoO₃ by Preserving Layered Nature[#]

Manuja M*, Tintu Thomas and Gijo Jose

Post graduate and Research department of Physics S.B. College Changanasserry
(Autonomous), Kottayam, Kerala, India

* E-mail: manuja.jayan85@gmail.com

Received: 20.9.2023, Revised: 20.1.2024, 27.1.24, Accepted: 27.1.24

Abstract

All polymorphs of 2D MoS₂ (1T, 2H & 3R) are layered with planes of molybdenum atoms sandwiched between two sulphur atoms (S-Mo-S layers) with intra planar covalent bonding and weak interlayer van der Waal's interactions. Here in this work, the role of polyethylene glycol as surfactant in the formation of 3R-MoS₂ is recognized. XRD and FTIR results provide structural elucidation and bonding information in the compound. More detailed crystal structure investigations and polyhedral visualizations were obtained in the Rietveld refinement procedure. The trigonal prismatic metal coordination in the 3R phase is portrayed with the ABC-ABC type layer stacking sequence. The morphology of layered 3R-MoS₂ nanostructure was identified from HRTEM images and the percentage composition from FESEM mapping and EDAX analyses. Temperature dependent mass loss in the compound is monitored and the quantitative analysis confirms the complete transformation of 3R-MoS₂ into layered α -MoO₃ at a temperature of 398 °C. Endo and exothermic peaks in the DSC and DTA measurements help to substantiate the results. Thus the work highlights the temperature assisted conversion of sulphide (3R-MoS₂) to oxygen ligand (α -MoO₃) of molybdenum at 398°C by cleavage of S-S bonds and preserving the layered nature.

Key words: 3R-MoS₂, layered nature, van der Waal's interaction, α -MoO₃, polyhedral structure.

[#] Paper presented during 3rd International Conference on Recent Trends in Analytical Chemistry (26-28 June 23) organized by Department of Analytical Chemistry, University of Madras, Chennai and ISAS Tamilnadu Chapter

Introduction

Molybdenum dichalcogenides, for variety of applications has been grabbing the researcher's incessant attention in this day and age. MoS₂ can have the similar properties as that of graphite with an advantage of non zero band gap¹ and finds applications in diverse fields such as optoelectronics², energy storage systems³, solar cells⁴, FETs⁵, switchable transistors⁶, memristor devices⁷ etc. Bulk MoS₂ is a diamagnetic⁸, direct bandgap semiconductor⁹ similar to silicon, with a bandgap of 1.23 eV. MoS₂ exists in three phases 1T, 2H and 3R phases. All forms have a layered structure, in which a plane of molybdenum atoms is sandwiched by planes of sulphide ions. 1T phase is metastable with a solitary layer and the basic building block is an octahedron. But in 2H and 3R phases the basic building block is a trigonal structure with two and three sorts of layers respectively¹⁰. The intra-planar connection is dominated by covalent bonding and the inter-planar bonding is very weak vander Waal's interactions¹¹.

The layered nature of MoS₂ can be exfoliated even to monolayer form using scientific methods. The exfoliation will accompany the change in band gap and the luminous intensity in photoluminescent spectra¹². The layered structure enables foreign cations to intercalate in between the layers and tunes the optical and electrical properties via structural distortion and band gap tailoring¹³. This work highlights the conversion of ligands associated with molybdenum atoms by providing heat treatment and the importance of these findings vest in the preservation of layered nature even after the change of ligands at high temperatures. The 3R-MoS₂ having trigonal prismatic co-ordination structure is transformed to octahedral geometry in α -MoO₃ during temperature treatment with accompanied oxidation. At the meantime the centre of symmetry of two compounds also changes. 3R-MoS₂ lacks center of symmetry and α -MoO₃ is centrosymmetric in structure. The change in symmetric structure can impose temperature stimulated electric phase transition in the compound thereby allowing conductivity tuning. Hence ligand conversion has importance in the present study even there is direct procedure for the production of layered α -MoO₃.

Experimental techniques

Sample preparation

The hydrothermal techniques were used to synthesize powdered 3R-MoS₂ from sodium molybdate (Na₂MoO₄.2H₂O-AR grade) and thiourea (NH₂CSNH₂-AR grade) in presence of

HCl/polyethylene glycol. 0.2 M and 0.6 M solutions of sodium molybdate and thiourea were prepared and mixed with 30 ml of diluted HCl with continuous stirring at 80 °C for half an hour. The resulting precursor solution is transferred to teflon lined stainless auto clave at 140 °C for 6h, 8h, 11h in three trials. The temperature increased to 200 °C and kept in an autoclave for 11h in the fourth trial. Again the acidic medium of HCl is replaced by polyethylene glycol and the process is repeated with 1.21g sodium molybdate, 1.56 g thiourea and 0.14 g polyethylene glycol in fifth trail. All samples were centrifuged several times using water and ethanol and dried in an oven at 80 °C for 3 h.

Characterization techniques

Structural confirmation of the prepared samples were done using powdered x-ray diffraction techniques (XRD) in Bruker D8 x-ray diffractometer having $\text{CuK}\alpha_1$ ($\lambda=1.5406 \text{ \AA}$) radiation with step size of 0.02 and a scan rate of 3° per minute between 2θ values ranges from 5 to 65°. The Rietveld refinement procedure of x-ray diffraction profiles for detailed investigation of structure and getting bonding information were done in fullprof suit. Further structural confirmations were done in FTIR analysis and were recorded using 'Perkin-Elmer' spectrum 2 with in a wavenumber range of 400 to 4000 cm^{-1} . The morphology was visualized from FESEM and HR-TEM images from Versa 2D dual beam analyzed equipped with EDAX and Tecnai G2T20 instrument FEI, Netherlands respectively. Thermo gravimetric analysis (TGA) and differential scanning calorimetry (DSC) were performed in SDTQ600. Thermogravimetric analyzer provides simultaneous measurement of mass change and differential heat flow on the same sample. Both measurements were taken with a heating rate of 20 °C/minute within temperature range from 30 to 700°C.

Results and Discussion

The samples collected were analyzed for its structural properties and phase purity by non destructive x-ray diffraction techniques at room temperature. Recorded PXRD profiles are displayed in Fig.1 (a). The figure compares and identifies the importance of polyethylene glycol in the synthesis technique. Fig. (1a) (i-iv) represents the diffracted PXRD profiles of samples prepared without polyethylene glycol at different processing temperature and time. The dominating peak at $2\theta=14^\circ$ becomes sharper with the rise in temperature and processing time. With the presence of polyethylene glycol as surfactant Fig. 1a (v) plot shows more

diffraction peaks at different 2θ values at 13.69° , 32.85° , 35.61° , 42.3° and 57.54° and could be indexed to (003), (101), (012), (015), and (110) planes. This corresponds to rhombohedral phase of MoS_2 as signified in Fig.1(b) along with the ICSD details at the bottom. The peaks in the spectra are confirmed without any impurities and is used for the further analysis throughout the work.

For getting further details regarding polyhedral structure refinement of XRD profiles are carried out and bonding details are analyzed. The Rietveld refinement enlightens more detailed crystal structure when refined in full profile suit. The least square approach is adopted for refining the recorded data to match with theoretical profiles. Pseudo-Voigt function in a linear combination of Gaussian and Lorentzian functions^{14,15} is used for the better refinement following the relation,

$$y(x) = V_p(x) = n * G(x) + (1 - n) * Ln(x). \quad (1)$$

The refined output corroborate $R\bar{3}m(160)$ space group in rhombohedral geometry with $3m$ point group having Wyckoff sequence $a\bar{3}$ and Pearson code $hR3$. The lattice parameters $a=b=3.1069\text{Å}$ and $c=19.0300\text{Å}$ matches well with the theory and prior findings with c/a ratio 6.1251Å . Higher c/a identifies the layer stacking with van der Waal's interaction along 'c' axis and is indicated in Fig. 2 (a). In rhombohedral MoS_2 ($3R\text{-MoS}_2$) the basic building block is trigonal prismatic coordination sphere with Mo (IV) occupies at the centre and each molybdenum atoms is surrounded by six sulphur ligands. The bond length details and the fundamental structures are shown in Fig. 2(b-c). Each Mo-S bond is equal with a distance of 2.5243Å where sulphur atom again is the centre of a pyramid and is connected to three Mo atoms with formula sum Mo_3S_6 which reconcile with previous reports. The atomic (distance between centre of nucleus and outermost shell of an atom¹⁶), ionic¹⁷ and vander Waal's radii¹⁸ of Mo/S atoms in the compound are $1.4/1.04$, $0.59/1.84$ and $2.02/1.8\text{Å}$ respectively. The higher the ionic radius, larger will be the spread of electron configuration in space and greater the tendency to polarize¹⁹. Hence the foreign ions having sufficiently lower ionic radius of Na^+ (1.02)²⁰, Li^+ (0.74), and Mg^{2+} (0.72) can be used to intercalate into the vacant site thereby improve the electric properties²¹.

The intraplanar covalent bonding exists in each MoS_2 bc planes and they are connected between two sulphur atoms by van der Waal's interaction along c axis originating the layered nature. Thus c/a ratio gets a higher value. In the layered structure, each Mo atoms are sandwiched between two layers of sulphur atoms. Basic layer is similar to the structure of $2H$

MoS₂ but in 3R structure each fourth layer is the repetition of first layers giving ABC-ABC layer stacking sequence thereby forms 3 different orientations along ab planes giving 3R structure. The symmetry operations and bravais sites obtained from the output pattern are $x, y, z; y, x-y, z; -x+y, -x, z; -x+y, y, z; x, x-y, z;$ and $-y, -x, z$ with bravais sites (0,0,0), (2/3,1/3, 1/3) and (1/3, 2/3, 2/3).

A deeper insight into inter and intra layer bonding were obtained from more sensitive FTIR observations as recorded in Fig. 3 within the wavenumber range of 400 to 4000 cm⁻¹. In addition to the peaks representing presence of water and O-H group at 3452 and 3162 cm⁻¹ respectively²², there are 4 other prominent peaks at 540, 931, 1083 and 1424 cm⁻¹. The first two peaks correspond to Mo-S and S-S bonding present in layered 3R-MoS₂^{23,24}. This represents the presence of covalent bonding between Mo and S and the interlayer van der Waal's interaction between sulphur ligands. This peak substantiates for the existence of layered nature in the compound. Next two peaks at 1083 and 1424 cm⁻¹ stands for the presence of polyethylene glycol, and -CH₂ stretching modes associated with the surfactant^{25,26}. A very small shoulder peak at 826.4 cm⁻¹ specifies the oxidation occurring on the surface level of sulphur ligands on MoS₂²⁷.

FESEM micrographs of rhombohedral MoS₂ are given in Fig. 4 (a) and disclose the agglomerated image of samples. The agglomeration makes the identification of proper morphology a tedious task however; the histogram represents the size distribution of the particle in the nano meter range. The nanostructure within the radius range of 60-80 nm shows maximum distribution and is indicated in the inset of Fig. 4 (a). HRTEM images played a role for more clear visibility of morphology and identification of growth direction. A single enlarged view of crystal is seen in Fig. 4 (b) identifies the 2D nanoflake like structure with thickness confined to 8 nm in dimension and the length x breadth is 174 × 145 nm. The attractive feature of the morphology lies in the transparent nature of samples with presence of pore sizes. Some of the pores are marked circularly in the respective image. The pore size has a diameter of about 9.43 nm and this can act as a host for foreign materials to root on the surface.

The morphology and its peculiar nature lead to vital applications of energy storage mechanisms²⁸. Lattice fringe pattern is given in Fig. 4 (c) shows incomplete layers but confirms d spacing of 0.6 nm indicating the (003) planes. The fringe pattern again clarifies the c directional layer stacking and the growth direction. SAED pattern tells about the

polycrystalline structure in Fig. 4 (d). FESEM mappings function as a supportive evidence for the identification of composition of elements present in the compound, along with EDAX results. The mapping of composition for the elements present in the highlighted region of Fig. 5(a) is shown in Fig. 5 (b-d). The inset of Fig. 5(b) gives the EDAX observations. The percentage composition of molybdenum and sulphur is identified as 1:2.33 in the typical compound. The non stoichiometry arises due to the incomplete growth of the sample during this processing time and temperature, as substantiated from lattice fringe patterns. The presence of both Mo^{4+} and Mo^{6+} are identified with a ratio of $\text{Mo}^{6+}/\text{Mo}^{4+}$ as 1.02²⁹. Existence of this non stoichiometric molybdenum takes the role of several unique electrical and optical properties in the typical compound and provides stability for the compound.

order to identify the thermal stability of the prepared material thermo gravimetric analysis was carried out. In TGA (Fig. 6 (a)), provides percentage mass loss as a function of temperature. For the sake of explanation, the total region of TGA is divided into four sections. In the first region (from room temperature to 102 °C) there is a mass loss of 6.9 % which corresponds to the removal of absorbed water from the compound associated with the hygroscopic nature of typical material. The region II (102 °C to 331 °C) shows a mass loss of 6.02%. The third region III (331 °C to 398 °C) suffers a mass loss of 5.2 % associated with the complete modification of 3R-MoS₂ to α -MoO₃. Higher temperature constancy of TGA plot indicates the stability of α -MoO₃ with respect to temperature. The removal of absorbed water from the compound at 102 °C is confirmed by an endothermic peak in DSC and DTA plots as represented in Fig. 6 (b).

As elucidated from the thermal analyses MoS₂ is annealed at 398 °C and room temperature PXRD result is verified. The orthorhombic (α) phase of MoO₃ is obtained. The phase pure and impurity free samples are identified from PXRD profiles and the peaks are indexed as shown in Fig.7. The standard JCPDS values are attached at the bottom for comparison. Presence of (0 2 0), (0 4 0), (0 6 0) and (0 10 0) identifies the growth of α -MoO₃ along {0 k 0} phase sets. The growth along the b axis is the clear indications of layered nature with inter layer van der Waal's interaction along the 'b' axis and the intralayer covalent bonding along the ac plane. Thus planar layer grows along the ac plane forming lamellar structure and the layer stacking occurs along the b axis as indicated in Fig.8 which represents Rietveld refined output of α -MoO₃. In addition, α -MoO₃ structure is formed from MoO₆ octahedra with Mo atom at the centre and surrounded by six oxygen atoms with three types of position specifications. The detailed structure of layered α -MoO₃ and its exfoliation techniques for the

reduction of layered number is discussed in our previous publication³⁰. The basic building block is octahedra MoO₆ as indicated in Fig.8. With the increase in temperature S-S bond gradually gets cleavage and new bonds are formed between Mo and O and it completely get transforms to α-MoO₃ at 398 °C while preserving layered nature.

Further confirmation of the processing time of MoS₂ preparation is done again by repeating the sample synthesis technique with polyethylene glycol for 24 h. The PXRD profiles are shown In Fig.9. The well defined peaks show the more oriented samples with the same growth direction (003) along c axis.

Conclusions

The hydrothermal synthesis of 3R-MoS₂ depends strongly on the presence of surfactant (polyethylene glycol), the processing time and the temperature. 3R-MoS₂ has layered nature with ABC-ABC stacking and fourth layer is the repetition of first layer. The layered nature arise due to the weak van der Waal's interaction between inter layer sulphur atoms. The growth direction and the layer stacking is along 'c' axis. Molybdenum is multivalent in the typical compound and the nonstoichiometry arises due to incomplete growth. With the increase in temperature S-S bonds breaks and new bonds form by the oxidation and the formation of Mo=O. Thus 3R-MoS₂ completely transforms to α-MoO₃ at 398 °C with the retention of layered nature and the growth is along 'b' axis.

Acknowledgement

MM acknowledges the financial support provided by Kerala Startup mission and KSUM, MG University (RINP 2022).

Figures:

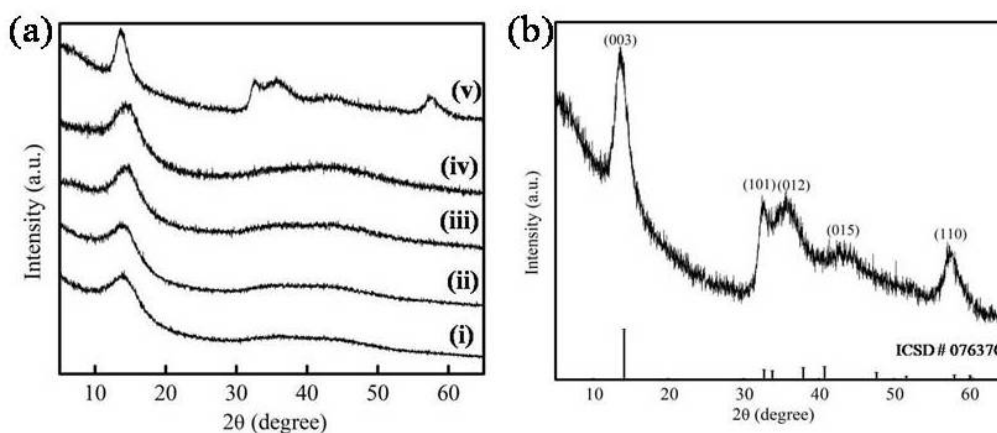


Fig. 1 (a) X-ray diffraction profiles of 3R-MoS₂ with different conditions of preparation (a-d) without polyethylene glycol at different processing time and temperature and (e) with polyethylene glycol. (b) The enlarged plot for 3R-MoS₂ with ICSD profiles at the bottom

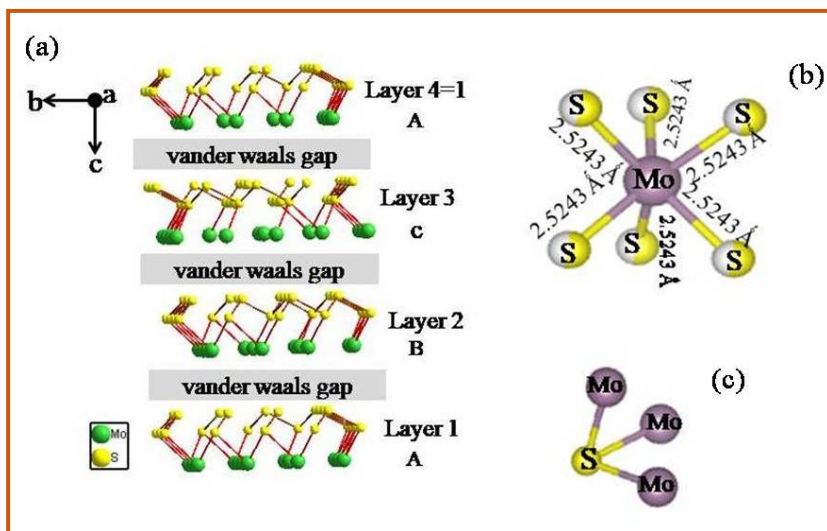


Fig. 2 Reitveld refined structure of 3R-MoS₂(a) clearly identifying the layered nature and stacking sequence (b) basic crystal structure of trigonal geometry with Mo at the centre and (c) with S at the centre

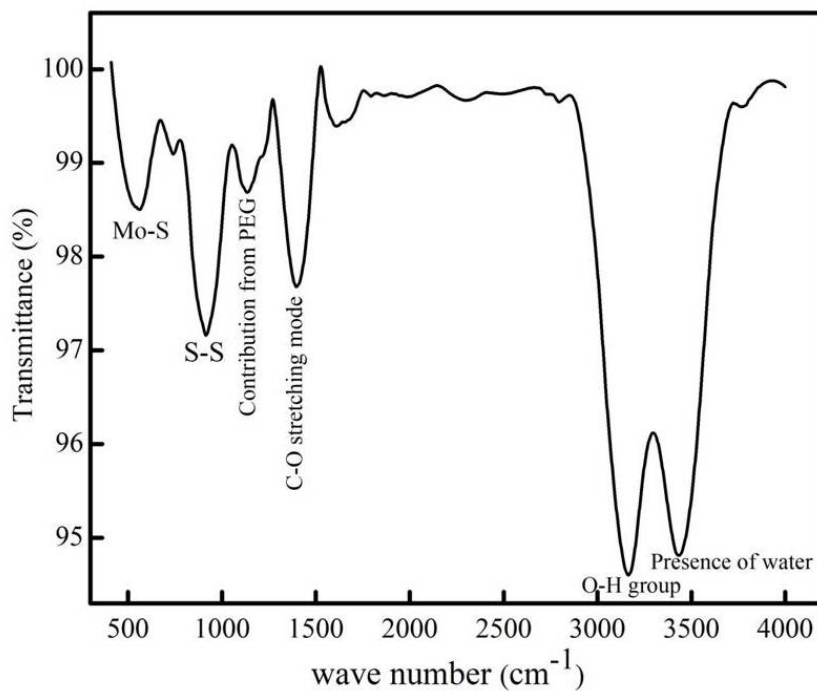


Fig. 3 FTIR spectra of 3R-MoS₂ with the wave number range 400 to 4000 cm⁻¹

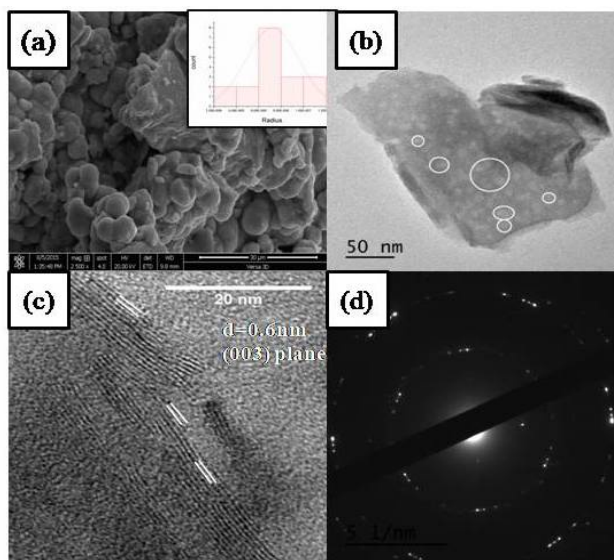


Fig. 4 Electron microscopy images of 3R-MoS₂ (a) FESEM images with histogram at the insets, (b) HRTEM image of a single particle morphology, (c) lattice fringe pattern and (d) SAED pattern .

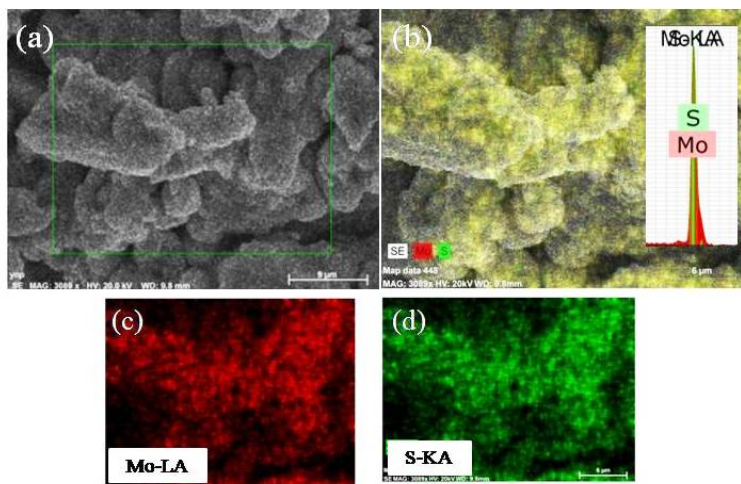


Fig. 5 FESEM mapping mages of 3R-MOS₂ (a) FESEM image, (b) mapped image with Mo and S presence of (c) Mo identification image and (d) S identification image.

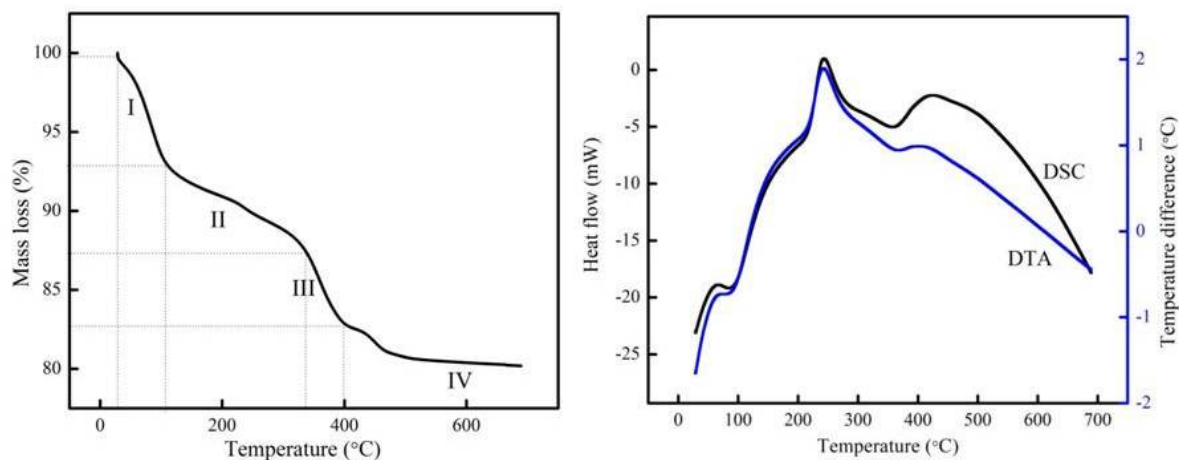


Fig. 6 Thermogravimetry analysis of 3R-MoS₂ (a) TGA indicating percentage mass loss with respect to temperature and (b) DSC and DTA plots of 3R-MoS₂

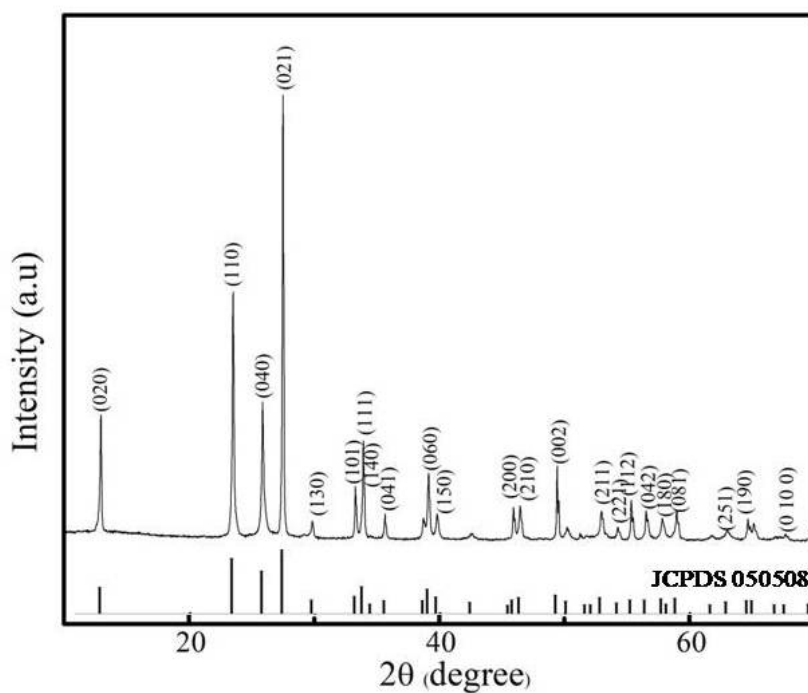


Fig. 7 X-ray diffraction patterns for layered α -MoO₃ with corresponding JCPDS data at the bottom.

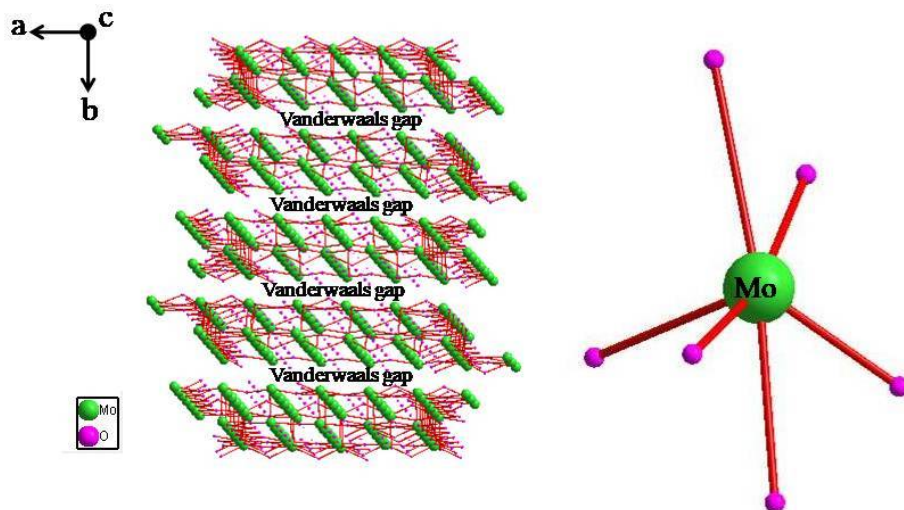


Fig. 8 Reitveld refined image of α - MoO_3 indicating layered nature and stacking sequence with the basic building blocks of octahedral structure with Mo at the centre.

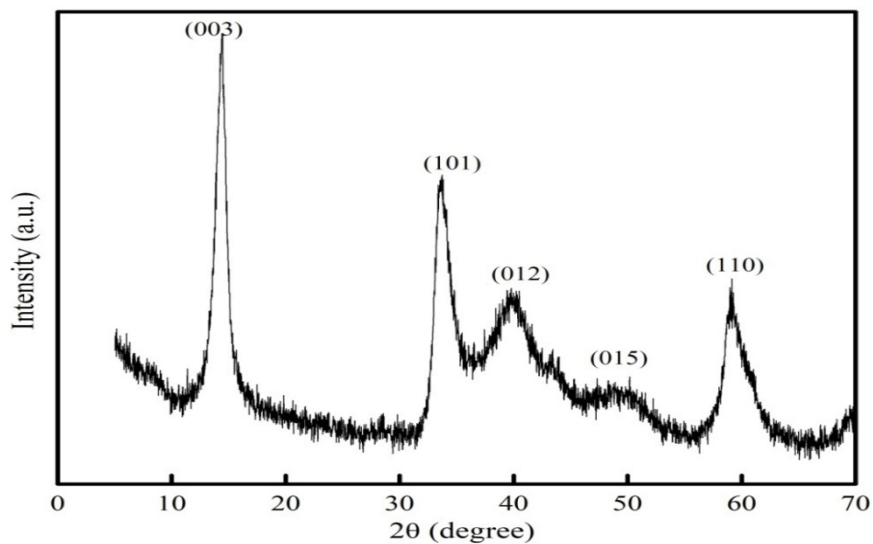


Fig. 9 X-ray diffraction profiles of 3R- MoS_2 with well defined peaks when PEG used as and processed at 24 h time

References

1. X. Li, and H. Zhu, *J.Materiomics*, 1(1), 33, 2015.
2. T. Nawz, A. Safdar, M. Hussain, D. S Lee, and M. Siyar, *Crystals.*, 10(10), 902, 2020.
3. T. Wang, S. Chen, H. Pang, H. Xue, and Y. Yu, *Adv. Sci.*, 4(2), 1600289, 2017.
4. U. Dasgupta, S. Chatterjee, and A. Pal, *J. Sol. Energy Mater Sol. Cells.*, 172, 353, 2017.
5. C. Wang, Y. Song, and H. Huang, *Nanomater.*, 12(18), 3233, 2022.

6. Y. Zhao, S. Bertolazzi, M. S. Maglione, C. Rovira, M. M. Torrent, and P. Samorì, *Adv. Mater.*, 32(19), 2000740, 2020.
7. Y. Gu, M. I. Serna, S. Mohan, A. L. Calderon, T. Ahmed, Y. Huang, and D. Akinwande, *Adv. Electron. Mater.*, 8(2), 2100515, 2022.
8. Mathew, S., Gopinadhan, K., Chan, T. K., Yu, X. J., Zhan, D., Cao, L., and Thong, J. T. *Appl. Phys. Lett.*, 101, 2012.
9. N. Thomas, S. Mathew, K. M. Nair, K. O. Dowd, P. Forouzandeh, A. Goswami, and S. C. Pillai, *Mater. Today Sustain.*, 13, 100073, 2021.
10. M. Manuja, and G. Jose, *Research Aspects in Chemical and Materials Sciences, BP international* 5, 2022.
11. S. W. Han, H. Kwon, S. K. Kim, S. Ryu, W. S. Yun, D. H. Kim, and S. C. Hong, *Phys. Rev. B*, 84(4), 045409, 2011.
12. M. Manuja, T. Thomas, and G. Jose, In *IOP Conf. Ser.: Mater. Sci. Eng.* IOP Publishing 1263(1), 012021,
13. M. Manuja, and G. Jose, *Fundamental Research and Application of Physical Science, B.P international* 2, 2023.
14. M. Manuja, T. Thomas, J. Jose, G. Jose, and K. C. George, *J. Alloys. Compd.*, 779, 15, 2019.
15. M. Manuja, K. V. Sarath, T. Thomas, J. Jose, and G. Jose, *J. Electron. Mater.*, 49, 2556, 2020.
16. P. Yadav, H. Tandon, B. Malik, V. Suhag, and T. Chakraborty, *Struct. Chem.*, 33, 389, 2022.
17. K. Hayamizu, Y. Chiba, and T. Haishi, *RSC adv.*, 11(33), 20252, 2021.
18. P. Luo, C. Liu, J. Lin, X. Duan, W. Zhang, C. Ma, and X. Liu, *Nat. Electron.*, 5, 849, 2022.
19. A. M. O. Mohamed, E. K. Paleologos, *Fundamentals of Geoenvironmental Engineering*, Butterworth-Heinemann, Elsevier 205 2018.
20. M. Goswami, S. Kumar, H. Siddiqui, V. Chauhan, N. Singh, N. Sathish, and S. Kumar, In *Emerging Trends in Energy Storage Systems and Industrial Applications*, Academic Press, 223 2023.
21. V. W. Fisher, J. M. Delgado, P. R. Nagy, E. Jakobsson, S. A. Pandit, and S. Varma, *J. Chem. Phys.*, 153(10), 104113, 2020.
22. K. C. Lalithambika, K. Shanmugapriya, and S. Sriram, *Appl. Phys. A*, 125, 1, 2019.

23. S. Liu, X. Zhang, H. Shao, J. Xu, F. Chen, and Y. Feng, *Mater. Lett.*, 73, 223, 2012.
24. K. C. Lalithambika, K. Shanmugapriya, and S. Sriram, *Appl. Phys. A.*, 125, 1, 2019.
25. A. R. Polu, and R. E. Kumar, *J. Chem.*, 8(1), 347, 2011.
26. S. Liu, X. Zhang, H. Shao, J. Xu, F. Chen, and Y. Feng, *Mater. Lett.*, 73, 223, 2012.
27. T. He, and J. Yao, *JPPC.*, 4(2), 125, 2003.
28. M. Manuja, T. Thomas, S. John, J. Jose, and G. Jose, *J. Alloys. Compd.*, 869, 159234, 2021.
29. M. Manuja, K. V. Sarath, and G. Jose, *IOP Conf. Ser. Mater. Sci. Eng.* IOP Publishing, pp012015, October 2018
30. M. Manuja, T. Thomas, J. Jose, and G. Jose, *Mater. Today. Proc.*, pp5283, 2022.

Modelling of CO₂ Sequestration in Deep Saline Aquifer Reservoir Using Surface Evolver Software

Pradeep Kumar

Bhabha Atomic Research Centre, Trombay, Mumbai, India, 400085.

E-mail: pradeepk@barc.gov.in

Received: 10.12.2023, Revised: 29.1.2024, 30.1.2024, Accepted: 30.1.2024

Abstract

A strategy to mitigate CO₂ concentration in the atmosphere is injection of supercritical CO₂ in porous sedimentary medium filled with saline water where CO₂ gets trapped in the pores. Sequestration is resultant of two processes, drainage and imbibition in accordance with capillary law. Simulation of the pore-scale trapping has been performed on reservoir scale. A simple model reservoir consisting of 1000 tetrahedral subunits was constructed. Using Surface Evolver software, pore volume of each tetrahedral subunit and liquid saturation in the model reservoir were calculated. Normalized critical curvature for drainage and imbibition were evaluated for each subunit. The CO₂ pressure and liquid saturation curves of the reservoir displayed hysteretic character, indicating that the evolution of the system is pathway-dependent. The simulated curves illustrate the pathway dependency of the residual gas saturation, an important parameter controlling the amount of CO₂ stored in the reservoir, hence the efficiency of the CO₂ storage. Our study also shows the existence of critical thresholds in terms of in/out gassing during the drainage or imbibition processes.

Key Words Reservoir, Drainage, Imbibition, Hysteresis

Introduction

In the previous article¹ published in this journal, pore scale investigation of CO₂ sequestration in sedimentary media has been described. The medium modelled as random packing of equal spheres, giving rise to a network of pore bodies connected by pore throats. The basic laws of capillarity are integrated to understand the CO₂ gas trapping processes at the pore scale. The two key processes, drainage and imbibition, responsible for CO₂ sequestration have been studied using the Surface Evolver software². Starting from liquid bridge adhering between two spheres, subsequently extended to liquid bridge adhering to three spheres and drainage and imbibition in pore throat have been investigated.

In the present paper, study has been extended to CO₂ trapping at reservoir scale. Reservoir is modelled as 3D network of large number of pore bodies connected by pore throats. The

pore is described in terms of tetrahedral subunits, centers of four spheres lying on the vertices of a tetrahedron. The void space inside the tetrahedron has been termed as pore body while the cross section of each face as pore throat. Initially drainage and imbibition processes are modelled at pore body for regular polyhedron. For reservoir, the heterogeneity is taken into consideration by means of distance variation among spheres.

Experimental

In the beginning, the entire reservoir contained the resident saline solution completely saturating the pores constituting a continuous wetting phase. During the drainage process, the non-wetting phase (CO₂) displaces the wetting phase (liquid) from the pores and progressively invades the pores network. At the extreme, the CO₂ forms a continuously connecting air bubble throughout the entire reservoir (pore network), and the residual water only persisting as pendular rings. The drainage process involves the receding of the meniscus (CO₂-brine interface) into the pore body, successively partitioning into several individual liquid bridges. The process occurs under the influence of two key parameters: the capillary pressure and the local geometry. In the present study simulations have been performed for various processes such as simulation of pore body drainage, simulation of pore body imbibition, imbibition at the pore throat. Simulation of drainage and imbibition for model reservoir has been performed.

(a) Simulation of Pore Body Drainage

At the pore scale simulation, liquid bridge adheres to four spheres arranged in a tetrahedral configuration. The arrival of the gas bubble is important event. This means building of a liquid-gas interface, which can pass through a pore body. Hence, the capillary properties of the pores determine the drainage of the pore bodies. Owing to tetrahedral configuration of pore, the interface can enter the pore from any of the four faces (pore throat) formed by three triangle-arranged spheres. In other words, the most critical step during a drainage process, is the conditions and situation where the pore body is emptied while the wedge-shaped parts remain filled.

The capillary pressure is a direct function of the curvature of the interface. The curvature gradually increases with the pressure. During injection period, the gas pressure increases significantly whereas variation in the liquid pressure is negligible. During injection period, a certain state is reached where interface passes into the pore body: the liquid spontaneously drains from the pore body and bubble goes on moving towards another network subunit. This spontaneous invasion is often termed as the Haines jump³ and the corresponding curvature is

called the critical curvature. The Mayer-Stowe-Princeton (MS-P) method⁴ is an accurate analytical method for calculating the critical curvature of complex geometries and yields satisfactory results for meniscus in pores formed by rods. Mason and Marrow^{5,6} experimentally observed that the MS-P theory provides good approximation to meniscus in pore throats formed by spheres as well, and so the curvatures were calculated using this MS-P method.

Following the simulation (Fig. 2), small CO₂ volume is held in pore throats before reaching the critical curvature, and it gradually increases with capillary pressure while the corresponding liquid volume is displaced. At the critical curvature conditions, CO₂ invades the pore body forcing the liquid out from the pore body. As a consequence, the CO₂ is percolating throughout the given subunit, while the water remains as pendular rings. Further increase in capillary conditions does not significantly enhance the CO₂ trapping. The liquid water in pendular rings corresponds to residual water saturation.

(b) Simulation of Imbibition

The imbibition process is the reverse of drainage process: pores are invaded by the wetting phase. Imbibition leads to formation of continuous liquid phase, implying the splitting of the CO₂ bubble into dispersed air pockets inside the porous medium. The imbibition process starts from the point where the drainage has ended. Here also, the location and shape of the interface is described by the capillary pressure, and the geometry of the portion of the pore hosting the interface. The imbibition is simulated through the incremental decrease in the capillary pressure gradually allowing water to invade the sampling network, thereby increasing the water saturation in the system. Thus, as the imbibition progresses, the capillary pressure correspondingly decreases, and the related configuration and location of the interface change. The interface moves reversibly in response to this decrement in the capillary pressure, as long as another interface is not encountered. Irreversible pore-level imbibition event occurs when decrement in pressure causes two interfaces to touch with each other, spontaneously merging into single interface. Now, restoring the pressure to prior values would not cause the wetting phase to split into its pre-merger situation: this fact is the true basis of what is classically called the hysteresis, namely the fact that the drying and the wetting branches do not correspond in terms of pressure-volume relationship. Clearly, the imbibition process disconnects the earlier continuous CO₂ phase.

(c) Imbibition at the Pore Throat

The imbibition process starts from the end point of the primary drainage (irreducible water saturation or any turning point of interest), and the capillary existing inside three pendular rings progressively decreases. As a consequence, the rings start growing and finally merge so that the entire plane delimited by three spheres is filled with liquid: CO₂ is spontaneously eliminated from this portion of the throat, disconnecting the gas phase. This type of imbibition is called coalescence or snap-off, and its main characteristic is that it preserves the hosted CO₂ bubble at the very centre of a tetrahedral sub-unit. Thus the continuous CO₂ phase becomes discontinuous, with the very positive feed-back (in terms of storage efficiency) of trapping air pockets surrounded by liquid barriers. The isolated CO₂ bubble, present in the pore body of the tetrahedral sub unit, is trapped under stable conditions (as long as the conditions do not change).

(d) Imbibition at the Pore Body

After the throat imbibition, a liquid bridge exists adhering to three spheres while the pore body entrance hosts the brine-CO₂ meniscus. On further decreasing the capillary pressure, the liquid bridge as well as the meniscus would grow in size, finally merging with each other. Such merging leads to spontaneous withdrawal of CO₂ phase from the pore body, or conversely leading to the spontaneous filling-up of the pore. Haines³ proposed an approximation to evaluate the critical curvature of imbibition. The meniscus in the pore is approximated to a sphere that just touches four spheres (nil contact angle). The imbibition curvature (C_{imb}) is therefore expressed by the following relation.

$$C_{imb} = \frac{2R}{r_{cav}} \quad (1)$$

Where 'R' is the radius of sphere and 'r_{cav}' is the radius of the in-sphere space. However, the drainage critical curvature calculated by MS-P method and the imbibition critical curvature calculated by Haines in-sphere approximation, resulted in a negative hysteresis, known to be practically impossible. As a consequence, Mason and Mellor⁷ suggested on sound grounds an empirical shift to the Haines values in order to eliminate the hysteric effect. Accordingly, they suggested the following relationship:

$$C_{imb} = \frac{2R}{r_{cav}} - 1.6 \quad (2)$$

Using these formulae, the pressure-volume relationships were derived along the different steps

described in Fig. 3. Obviously, the imbibition at the pore throat occurs at higher pressure than the imbibition at the pore body. Initially, only one of the throats gets imbided, and after a certain range of capillarization inside the system, the pore body itself gets imbided (Fig. 3). Along the imbibition pathway, it becomes evident that much larger CO₂ amount gets trapped than along the drainage pathway.

(e) Simulation of drainage and imbibition for model reservoir and hysteresis in capillary pressure

So far, we have carried out pore scale investigation for single regular tetrahedron. These investigations have provided direct insight on the role of the geometry on the drainage and imbibition processes at the pore level. At the reservoir scale, the sequestration is expressed by capillary pressure versus the liquid saturation graph, and so the principle of the simulation and the lines of interpretation remain similar.

However, while carrying out simulation for a large scale reservoir, it is imperative to take into consideration the degree of heterogeneity, at least defining a certain range of existing porosity. In the pore level approach, the reservoir is modelled as random packing of equal spheres while at the basin scale, integration of grain size variation is required. To make preliminary estimation, we have built a model reservoir consisting of a network of irregular tetrahedrons, by using equal-size spheres separated by varying distances. As a consequence, the hosting porosity is changing throughout the media in a way analogous to what occurred in nature with varying grain size.

Actually, the distance between the centres of two spheres constitutes the edge of the tetrahedron. For a reservoir consisting of random packing of equal spheres, most often the spheres are in contact with each other. Meanwhile, for separated spheres, all edge lengths of tetrahedron are almost equally probable up to 1.4 times the sphere diameter⁷. In the tetrahedral subunits, one sphere was assumed to be in contact with the other three spheres, whereas for separated spheres all possible combinations of edge lengths (again, up to 1.4 times the sphere diameter) were taken into consideration for the construction of irregular tetrahedral subunits. A simple model reservoir was constructed consisting of 1000 tetrahedral subunits. Pore volume for each subunit was calculated and liquid saturation in the model reservoir was obtained. Similarly, normalized critical curvature for drainage and imbibition were calculated for each subunit. The imbibition critical curvatures are lesser than the

drainage critical curvatures (Fig. 4, on only 200 pores statistically chosen), according to the above described processes.

To drain a subunit, the gas-liquid interface would enter from the face (throat) having the smallest capillary pressure, i.e. the smallest drainage critical curvature. The critical curvature obviously decreases with the widening of the distance between the spheres. Hence, it is easier to penetrate the pore body through the face having large distance between the spheres (smallest capillary pressure between the three faces). The respective amount of liquid and trapped CO₂ depends upon the pore volume itself as per the edge lengths constituting the tetrahedral subunit. Two pores can possess the same volume even with different combination of edge lengths. With widening the distance between spheres, the pore volume increases while the interface curvature decreases: larger pores are easier to drain. Initially the model reservoir is assumed to be completely filled with liquid phase (100% liquid saturation). For the model reservoir, the drainage process was simulated by successively draining the pores in the order of their increasing drainage critical curvature and calculating the corresponding liquid/CO₂ saturation in the reservoir as well as capillary pressure (Fig- 5). The model reservoir shows ~7% residual water saturation, a value calculated as the remaining liquid amount (trapped as pendular rings) when the drainage emptied even the smallest pore throats/bodies of the model reservoir.

After having reached the residual liquid water saturation, the simulation makes the capillary pressure to progressively decrease. As a consequence, the pores of the model reservoir get imbibed following the order of the decreasing imbibition critical curvature. As mentioned earlier, the liquid/CO₂ saturation and the capillary pressure can be calculated along the imbibition. Owing to the tetrahedral structure of pore body, the critical drainage curvature and imbibitions curvature are different: imbibition occurs at lower curvature than drainage, this leads to hysteric effect⁸. In other words, drainage depends on the critical curvature of the pore throat whereas the imbibition depends upon the pore body. As a consequence, the imbibition curves plot at lower pressure than the drainage curve (Fig-5), and such curves are often called hysteretic curves. During the imbibition process, CO₂ gets trapped in some pores depending upon the injection conditions of the reservoir, e.g. the capillary number. Suekane et al.⁷ have experimentally observed the presence of a residual gas saturation (after the final stage of imbibition) and found it to depend on the capillary number, namely the ratio between the velocity of the liquid-gas interface and the interfacial tension. For low capillary numbers, flow in porous media is dominated by capillary forces. Very logically, Suekane et al.⁷ concluded that the residual gas saturation decreases as the capillary number increases.

We decided to calculate the value of this residual gas saturation by fixing arbitrarily the percentage of pores keeping its gas bubbles in the final stage of the process. We have chosen three situations: 10%, 20%, 30% of pores trapped by CO₂, resulting in residual gas saturations of 10%, 17% and 26%, respectively (Fig. 5).

Another important parameter that needs to be considered is the saturation existing at the state where the system changes from drainage to imbibition, called the turning point (Fig. 6). According to the concepts developed above, at any turning point above the irreducible liquid saturation, some pores contain large amount of CO₂ along with liquid pendular rings and are ready to the imbibition stage, while others are still almost entirely filled with liquid. As a consequence, when turning to the imbibition stage, the first type of pores can trap CO₂ bubbles and contribute to the residual gas saturation while the latter do not experience significant changes. For a given model reservoir, certain percentage of pores participate in the residual gas saturation, then the irreducible gas saturation depends mainly upon the saturation value at the turning point (Fig. 6).

The higher the reservoir is liquid saturated at the turning point (the lesser is the number of pores experiencing the complete emptying), the lesser is the residual gas saturation (Fig. 6). The maximum residual gas saturation corresponds to the turning point at the irreducible liquid saturation.

Results and Discussion

In the present study, starting from simulation of drainage and imbibition processes of tetrahedral subunits, was extended to reservoir scale. The reservoir was modelled as random packing of equal spheres consisting of 1000 tetrahedral subunits giving rise to 3-D network of pore bodies and pore throats. The heterogeneity aspect of reservoir was taken into consideration by varying the distance between two equal- size spheres upto 1.4 times the side length. The drainage and imbibition processes are governed by the capillary pressure and the local geometry. For a tetrahedral subunit, pore body drainage was simulated in terms of as progressively increasing curvature of gas-liquid (CO₂-brine) interface. The interface penetrates through face formed by triangle configuration of spheres .

During the CO₂ injection period, at certain point interface passes into the pore body and the liquid spontaneously drains from the pore body, gas bubble goes on moving towards another network subunit. Critical curvature was calculated by Mayer-Stowe-Princeton (MS-P) method. Imbibition causes the splitting of the CO₂ bubble into dispersed air pockets inside

the porous medium. Irreversible pore-level imbibition takes place when two interfaces touch with each other, spontaneously merging into single interface. Imbibition occur at throat where the pendular rings start growing and finally merge, CO₂ is spontaneously eliminated from this portion of the throat, disconnecting the gas phase. This type of imbibition is called coalescence or snap-off. On further decreasing the capillary pressure, the liquid bridge as well as the meniscus inside pore body would grow in size, finally merging with each other, leading to spontaneous withdrawal of CO₂ phase from the pore body, or conversely leading to the spontaneous filling-up of the pore. Haines approximation, modified by Mason and Mellor was employed to evaluate the critical curvature of imbibition.

On similar lines, simulation for reservoir was carried out. At the reservoir scale, the sequestration is expressed by capillary pressure versus the liquid saturation graph. Using Surface Evolver software, pore volume for each subunit and liquid saturation in the model reservoir was obtained. Also Normalized critical curvature for drainage and imbibition were calculated for each subunit. The imbibition critical curvatures are lesser than the drainage critical curvatures. The drainage occurs during CO₂ injection in the system whereas imbibition occurs during post injection period. The study revealed that the system is highly pathway-dependent, indicating hysteretic character of the pressure-volume curves. This can be assigned to the fact that the imbibition curvature is lesser than drainage curvature. The gas trapping in reservoirs as gas bubbles gets stabilized inside the pore bodies or pore throats, may be very efficient and could be expected to be a major parameter in the gas storage amount.

On the CO₂ sequestration point of view, the residual gas saturation is of the utmost importance, since it determine the amount of CO₂ permanently trapped as gas bubbles, a parameter that directly participates in the efficiency of the global storage operation. One major features outlined by our study is the strong dependency of this residual gas saturation, on the pathway followed by the bubble during the post-injection period. The more the bubble disperses throughout the media, the more drained is the reservoir, the more CO₂ will be finally trapped. On the contrary, whenever the injected massive bubble slides inside the reservoir without splitting in many interfaces throughout the pores, the less drained is the reservoir implying that the final gas trapping is drastically reduced.

Conclusions

In the present study we have performed modelling of CO₂ sequestration in deep saline aquifers using surface evolver software. The actual reservoir is very complex. For sake of

simplicity, the reservoir is modelled as random packing of equal spheres which nearly mimicks real reservoir. Drainage and imbibition processes have been investigated taking into consideration the capillary pressure and reservoir geometry. For obtaining critical curvature for drainage Mayer-Stowe-Princeton (MS-P) method was used. The critical curvature of imbibition was evaluated using Haines approximation, modified by Mason and Mellor. The model reservoir showed ~7% residual water saturation. The residual gas saturation was calculated by arbitrarily fixing the percentage of pores keeping its gas bubbles in the final stage of the process. For three situations 10%, 20%, 30% of pores trapped by CO₂, the residual gas saturations was observed to be 10%, 17% and 26%, respectively .

Thus, the present study provides interesting insights into the basic aspects of the CO₂ sequestration, especially the mechanisms accompanying the residual (water or CO₂) saturation, and the associated amounts of trapped materials. One interesting feature highlighted by the present study is the threshold effects related to the critical curvature characteristics of the reservoir. Generally speaking, the more polydisperse is the porosity of a reservoir, the more thresholds (in-or out-gassing) will be experienced through the post-injection period. As a matter of fact, this feature corresponds to pressure/volume pulses which may display negative feed-back in terms of storage security. Each time a threshold is crossed; a certain volume of CO₂ is trapped or pushed away, with a related brutal variation of the mechanical balance at the reservoir scale. Such very rapid events necessarily impact both the hydraulic conductivity and the local pressures, possibly contributing to affect the integrity of the reservoir (micro-fracturing). Our model reservoir is not able to simulate these consequences since it has no closed boundaries, and the liquid is free to move outside the model box during drainage at constant liquid pressure. Due to this, we do not simulate the increasing liquid pressure associated to the drainage process, and its related equilibria towards the gas pressure, these mutual changes controlling the behavior of the global bubble. As a consequence, the present strategy and calculations could be extended to complex geometries, as those defined through the packing of grains having varying and complex individual shapes. There is scope to calibrate our present model reservoir against a real system, by building a heterogeneity index (ratio between the different kinds of tetrahedral units) accounting for the pore-size distribution curves measured in the real reservoir. Further studies should open the present reasoning and considerations to practically applied calculations and predictions.

Figures

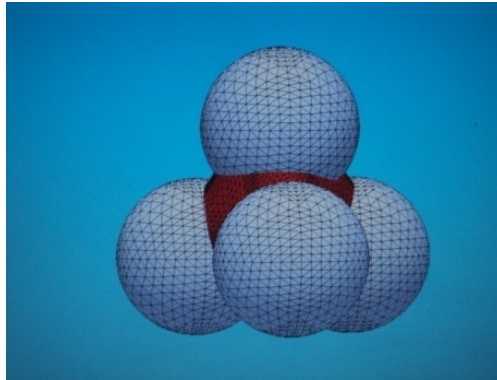


Fig. 1. Liquid bridge adhering to four spheres arranged in a tetrahedral configuration

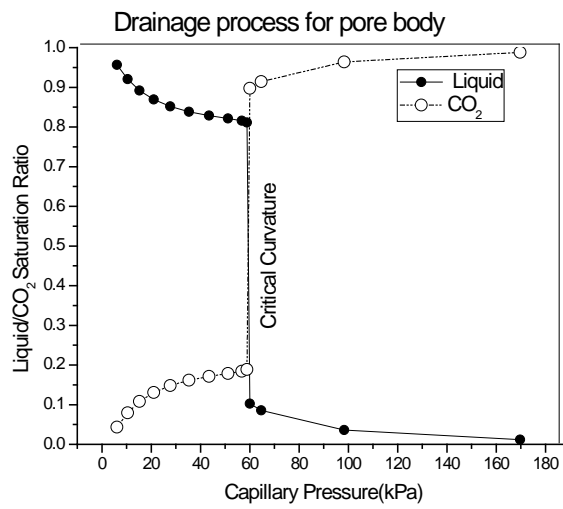


Fig.2. Variation of the liquid and CO₂ saturation with respect to capillary pressure

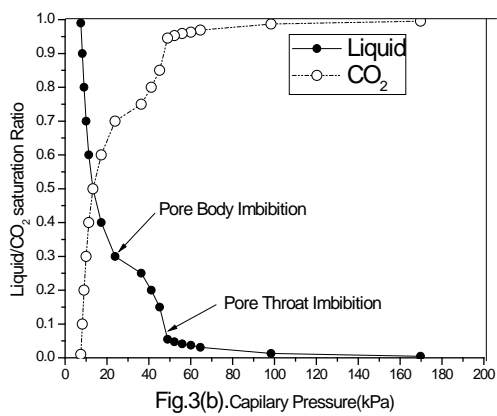
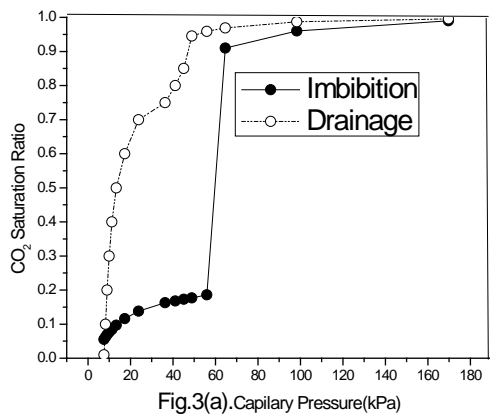


Fig. 3(a). Different steps in the imbibition process for pore body formed by four spheres arranged in tetrahedral configuration. Fig.3(b). Comparison of CO₂ invasion during drainage and imbibition.

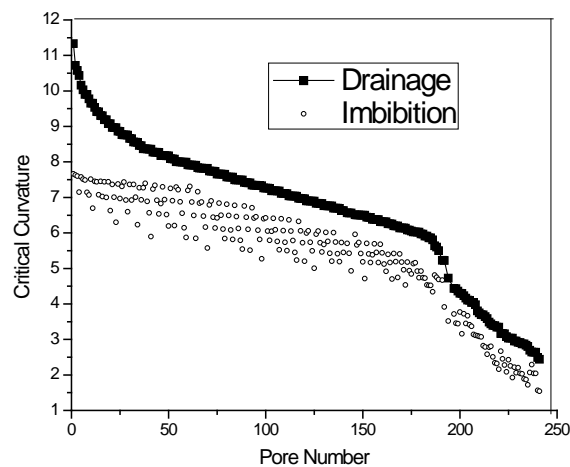


Fig. 4. Normalized critical curvatures of drainage and imbibition for the model reservoir pore bodies

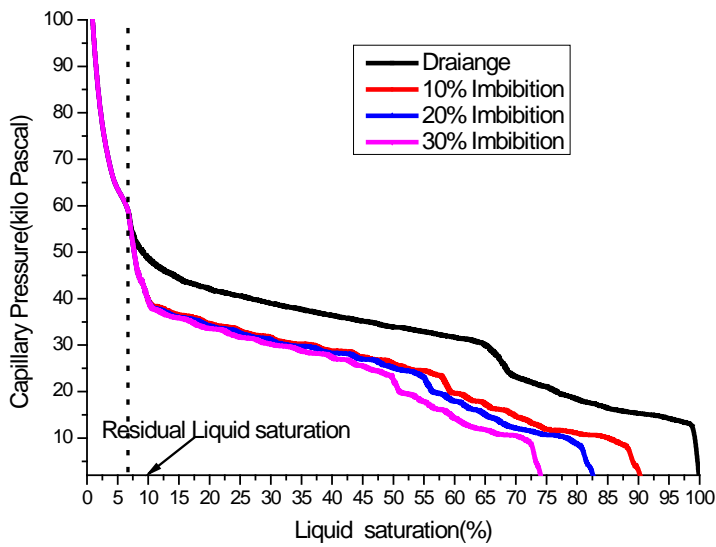


Fig. 5. Characteristic capillary pressure versus liquid saturation graph. Drainage is shown by continuous line and imbibition by broken lines. Imbibition is shown for situations with residual gas saturation filling 10%, 20%, 30% of the reservoir pores .

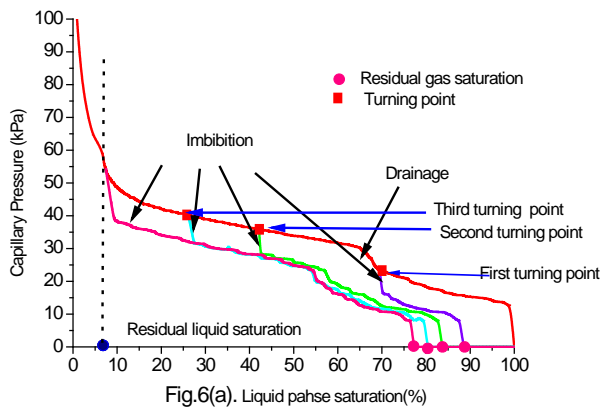


Fig.6(a). Liquid phase saturation(%)

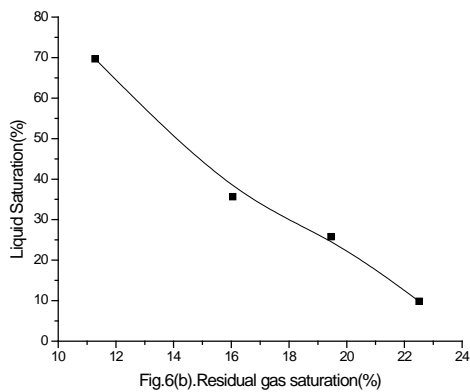


Fig.6(b).Residual gas saturation(%)

Fig. 6(a) characteristic capillary pressure curves for a model reservoir assuming 20%

pore are CO₂-trapping.

Fig.6 (b) Residual gas saturation plotted as a function of liquid saturation at the turning point.

References

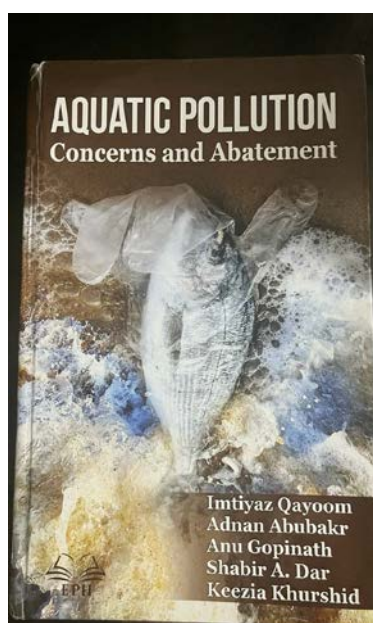
1. Pradeep Kumar, J. ISAS., 1(3), 1, 2023.
2. Brakke A.K. Surface evolver manual. Susquehanna University Selinsgrove, PA 17870.
3. The Surface Evolver software is available on <http://www.susqu.edu/brakke/evolver>. Year 2008.
4. Haines W.B. J., Agri. Soc., 20,1930,97.
5. Mayer R.P. and Stowe R.A., J. Colloid Interf. Sci., 20,1965,93.
6. Mason G. and Marrow R.N., J. Colloid Interf. Sci., 100(2), 1984, 519.
7. Mason G. and Marrow R.N., J. Colloid Interf. Sci., 109(1), 1986, 46.
8. Mason G. and Mellor W.D. J. Colloid Interf. Sci., 176 (1995) 214.
9. Suekane T, Thanh N.H, Matsumoto T, Matsuda M, Kiyota M, Ousaka A.
10. Energy Procedia, 1, 2009, 3189.
11. Doughty C. Energy Conversion Management, 48, 2007, 1768.

**Review of the Book: Aquatic Pollution – Concerns and Abatement by
Imtiyaz Qayoom, Adnan Abubakr, Anu Gopinath, Shabir.A. Dar , & Keezia Khurshid**

Dr Anoop Krishnan

Scientist- E, Biogeochemistry Group, National Centre for Earth Science Studies, Trivandrum

sree.anoop@ncss.gov.in



This book is based on invited chapters on issues related to aquatic pollution. It also focuses on the sources, mechanisms, impacts and abatement of pollution in various waterbodies. Moreover, the role of vital model organisms that not only act as pollution indicators but also as agents to remove pollutants from lakes has been comprehensively addressed. The readers will also get acquainted with various methods of decontamination like phytoremediation, pesticide removal techniques, toxic site reclamation and environmental sustainability using microbial aspects associated with clean-up of wastes. It has fifteen invited chapters and is published by Elite Publishing Group, New Delhi (2024). The book invites the intellect and vision of scientists from all over the world to address environmental deterioration and come up with efficient measures to combat the global issue of water pollution. The ISBN No is 978-93-58999-70-9.